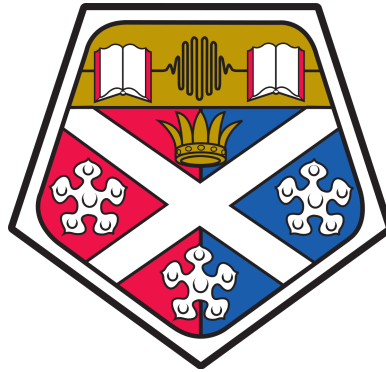


Development of Micro-fabricated Vapour Cell Technology for Compact Atomic Devices

Sean Dyer

A thesis presented in the fulfilment of the requirements for
the degree of
Doctor of Philosophy



Experimental Quantum Optics and Photonics
Department of Physics and SUPA
University of Strathclyde

November 2024

Declaration

This thesis is the result of the author's original research. It has been composed by the author and has not been previously submitted for examination which has led to the award of a degree.

The copyright of this thesis belongs to the author under the terms of the United Kingdom Copyright Acts as qualified by University of Strathclyde Regulation 3.50. Due acknowledgement must always be made of the use of any material contained in, or derived from, this thesis.

Signed:

Date:

Abstract

This thesis follows several investigations into micro-fabricated vapour cells towards the development of compact and field deployable atomic devices such as RF/optical atomic clocks, wavelength references and magnetometers. Initially I investigated a novel fabrication technique using a water-jet cutter to form deep silicon cavities allowing for micro-fabricated vapour cells to be produced with a 6 mm optical path length in an efficient and low-cost manner. I then investigated controlling the N₂ pressure within a micro-fabricated cell via laser heating an non-evaporable getter. From this study it was found that the N₂ pressure could be reduced from one to hundreds of Torr and this technique was then used to map out the intrinsic relaxation rate of the Cs atoms within the cell with a optically pumped magnetometer. Then I investigated packaging a Rb cell with a 1 mm optical path length together with printed circuit board coils to create a Zeeman tunable wavelength reference, which demonstrated a frequency tunability of ± 60 MHz and a short-term frequency stability comparable to conventional Rb wavelength references. Next I fabricated a 6 mm thick micro-fabricated cell, which was capable of sustaining a cold atom sample with active vacuum pumping. This cell was integrated with a micro-fabricated diffractive optic to produce a chip-scale laser cooling platform capable of trapping 10^6 ⁸⁷Rb atoms. Finally I investigated different fabrication routes to realise a micro-fabricated vapour cell with an elongated geometry for two-photon optical clocks.

Acknowledgements

This thesis was made possible through the invaluable guidance provided by my supervisors Erling Riis, Paul Griffin and James McGilligan, to whom I owe a deep debt of gratitude. I would first like to express my gratitude to Erling for giving me the opportunity to study within the experimental quantum optics and photonics group at Strathclyde and for sharing his invaluable wisdom, which set me on this path. Griff has been a fount of knowledge and support both in the lab and the writing of this thesis. I have had the pleasure of working closely with James over the course of my PhD from, which I learned many tricks of the trade from making vapour cells through to selecting an appropriate soundtrack for the task at hand. I would like to extend my thanks to all the members of the clock team, both past and present. It has been a pleasure to work alongside Alan Bregazzi, Rachel Cannon and Allan McWilliam on various projects, sharing a couple of pints and plenty of patter.

I would like to thank my parents for their constant encouragement, especially for motivating me to persevere during my school years. I am also thankful to Betty for taking the time to share her university experiences with me. My heartfelt thanks go to my fiancée, Louise Rooney, whose unwavering support has undoubtedly made completing my PhD much easier, especially during the writing of this thesis. I now look forward to spending all the time I have freed up with you. Lastly, but certainly not least, I want to thank my daughter, Grace Dyer, for always bringing a smile to my face with her antics.

Contents

List of Figures	iii
1 Introduction	1
1.1 Atomic Sensors and Devices	1
1.2 Micro-fabricated atomic vapour cells	2
1.3 Thesis Layout	3
2 Atomic physics	7
2.1 Atomic Structure	7
2.2 Absorption Spectroscopy	9
2.2.1 Spectral Profile	10
2.2.2 Number Density	11
2.2.3 Absorption Profile	12
2.3 Saturation Absorption Spectroscopy	14
3 Micro-fabricated Silicon Vapour Cells	16
3.1 Vapour Cell Fabrication	17
3.2 Experimental Setup and Results	21
3.3 Conclusion and Future Work	27
4 Nitrogen Buffer Gas Pressure Tuning	29
4.1 Buffer Gas Cell Fabrication	32
4.2 Extracting Buffer Gas Pressure	33
4.3 Laser Controlled Gettering	43
4.4 Optimising Relaxation Rate	46

4.5	Buffer Gas Pressure Stability	50
4.6	Nitrogen Evacuated Cell	52
4.7	Conclusion	57
5	Compact Zeeman Tunable Wavelength Reference	59
5.1	Atomic Wavelength Referencing	60
5.2	Zeeman Tunable lock	61
5.3	Physics Package	63
5.4	Frequency Tuning	67
5.5	Frequency Stability	70
5.6	Conclusion and Future Work	74
6	Chip-scale Cold Atom Platform	76
6.1	Laser Cooling	77
6.1.1	Optical Molasses	77
6.1.2	Magneto-Optical Traps	79
6.1.3	Grating Magneto-Optical Traps	81
6.2	Micro-fabricated UHV Vapour Cell	82
6.3	Experimental Setup	85
6.4	Results	88
6.5	Conclusions and Future Work	93
7	Elongated Vapour Cell for a Two-Photon Optical Clock	94
7.1	Degenerate Two-Photon Spectroscopy	95
7.2	Wet Etched Silicon Reflector	97
7.3	Commercial Prism Reflectors	104
7.4	Conclusions and Future Work	107
8	Conclusion	110

List of Figures

2.1	Atomic structure	8
2.2	Theoretical absorption for the D ₂ line in Rb	13
2.3	Example saturation absorption spectroscopy	15
3.1	Water-jet overview	18
3.2	SEM images of cell walls	19
3.3	Anodic bonding overview	20
3.4	Water-jet cell fabrication	21
3.5	Alkali source laser activation	22
3.6	Cell images and measured absorption during activation	24
3.7	Absorption spectra from 6 mm thick vapour cell.	26
4.1	Theoretical Buffer gas pressure vs relaxation rate.	31
4.2	Buffer gas cell fabrication	33
4.3	Cs spectra with and without buffer gas.	34
4.4	Buffer gas monitoring setup	36
4.5	Etalon fits	38
4.6	Cs Reference cell fit	40
4.7	Micro-fabricated cell fit	42
4.8	N ₂ buffer gas tuning	45
4.9	Vapour cell geometries	47
4.10	FID trace	48
4.11	Buffer gas vs relaxation rate	49
4.12	Transmission in a buffer gas cell as function of temperature.	51

4.13	Buffer gas stability	52
4.14	Saturation absorption spectroscopy setup for N ₂ evacuated cell.	54
4.15	Sub-Doppler spectroscopy of a N ₂ evacuated cell.	56
5.1	A simple rubidium wavelength reference setup.	60
5.2	Optical pumping with σ^+ transitions illustration	62
5.3	Compact Zeeman tunable spectroscopy package.	64
5.4	Predicted field strength	65
5.5	Saturated absorption spectrum and error signal obtained from the compact package	66
5.6	Beat note measurement setup	67
5.7	Frequency shift provided by PCB coils	69
5.8	Overlapping Allan deviation laser stability comparison	71
5.9	Overlapping Allan deviation for different B fields.	73
5.10	Overlapping Allan deviation as a function of cell temperature	74
6.1	Acceleration from 1D molasses.	78
6.2	schematic of a 1D MOT	80
6.3	TRI grating chip	81
6.4	Fabrication process of the micro-fabricated UHV cell	84
6.5	Absorption spectra from the UHV cell	85
6.6	laser cooling experimental setup	86
6.7	Compact cold-atom platform	87
6.8	Example photodiode rise-curve	89
6.9	Atom number measurements	90
6.10	Atom number stability	92
7.1	Two-photon energy level diagram.	96
7.2	The fabrication process for the periscope cell.	99
7.3	Two-photon experimental setup.	100
7.4	Initial two-photon spectrum.	101
7.5	Fitted two-photon spectrum from the periscope cell.	102
7.6	Wet etched reflector images	103

7.7	The fabrication process for the COTS cell.	106
7.8	Fitted two-photon spectrum from the COTS cell.	107
7.9	Anodically bondable reflector.	108
7.10	The fabrication process for the polished silicon reflectors.	109

Chapter 1

Introduction

1.1 Atomic Sensors and Devices

Atoms provide an incredibly versatile platform for sensing allowing for the realisation of high performance clocks [1], interferometers [2], electric field sensors [3] and magnetometers [4] to only name a few of their potential applications. These devices operate by probing an ensemble of atoms with electromagnetic radiation to interact with the internal energy levels of the atoms.

Devices based on these interactions offer an intrinsic reproducibility, as every atom of a given element will behave identically when put under the same experimental conditions. Additionally the atomic energy levels are sensitive to perturbations in the surrounding environment, which modifies this interaction allowing for measurements of temperature [5], gravitational red shift [1], biomagnetic signals [6], etc. When these sensors are built to provide the highest precision and accuracy, they can require an entire lab filled with electronics, optics and vacuum apparatus, which limits their potential applications due to the challenges of transporting such equipment.

Due to the need for these sensors to be field deployable there is a market for atomic devices, which are compact and portable whilst maintaining a performance good enough for the end user and their application. An example of such an atomic device is the rubidium frequency standard (RFS) developed in the 1950's. The

RFS offers a fractional frequency stability of 10^{-12} at 1s, which is 3 orders of magnitude worse than state of the art atomic clocks [1] however, it is still good enough to be used for timing onboard GNSS satellites [7]. A RFS built for space applications such as GNSS is commercially available from several companies with a typical package size of $<5000 \text{ cm}^3$, weighing $\leq 7.5 \text{ Kg}$ and requires $\leq 40 \text{ W}$ of electrical power to run [8].

In the early 2000's a significant research effort was undertaken by teams in the US towards the development of chip-scale atomic devices [9], which would be light weight and battery operated increasing the number of potential applications. To achieve this goal the development of miniaturised and mass producible components for these devices was critical.

1.2 Micro-fabricated atomic vapour cells

A key step towards the development of chip-scale atomic devices was the invention of the micro-fabricated vapour cell [10,11] by the atomic devices and instruments (ADI) team at NIST. A vapour cell is an isolated vacuum chamber filled with a specific atom or molecule of choice, which are conventionally glass-blown. The chip-scale vacuum chambers developed by NIST were comprised of a glass wafer, an etched silicon cavity and a final glass wafer stacked on top of each other, which are anodically bonded together [12]. Prior to sealing the cells are either filled directly with the atomic species of choice [13] or with a precursor [14], which can be decomposed into the atomic species after sealing. Since these vapour cells are fabricated with pre-existing micro-electro-mechanical systems (MEMS) processes they can be produced in large quantities at a low cost whilst being easily integratable with other micro-fabricated components.

In 2004 the team at NIST integrated these micro-fabricated vapour cells into packages with other chip-scale components to produce a chip-scale atomic clock (CSAC) [13]. Later that same year, they also developed a chip-scale atomic magnetometer (CSAM) [14]. Both of these devices had physics packages with

a volume $\leq 12\text{mm}^3$ and consumed $\leq 200\text{mW}$ of electrical power. Whilst these chip-scale devices demonstrated a degraded performance compared to their lab scale counter parts they have still found commercial success with applications in a variety of industries from defense to medical imaging due to their small size, weight and power consumption (SWaP).

In the 20 years since their invention there has been significant effort put into the further development of chip-scale atomic devices to improve their performance, reduce their manufacturing costs as well as translating the success of the CSAC and CSAM to other atomic sensors with research programs in the USA, France, Germany, Switzerland, China, Japan and UK [9]. An example of such a program is NIST on a chip [15], which strives to develop chip-scale packages capable of providing measurements traceable to SI standards by leveraging atomic sensors that interrogate a micro-fabricated vapour cell. Throughout these research programs there has been a continued development of micro-fabricated vapour cell technology investigating different atomic sources [16, 17], vapour cell geometries [18, 19] and fabrication techniques [20–23] with the goal of producing micro-fabricated cells, which are optimised for their particular application.

1.3 Thesis Layout

This thesis focuses on the development of micro-fabricated vapour cell technology for compact atomic devices covering aspects ranging from fabrication techniques to pressure control within the cell.

- Chapter 2 covers the relevant background physics to explain absorption spectroscopy of hyperfine transitions, which is used throughout this thesis.
- Chapter 3 discusses the water jet cutting of silicon to realise micro-fabricated vapour cells with a 6 mm thick optical path length.
- Chapter 4 demonstrates the use of a non-evaporable getter to tune the nitrogen buffer gas pressure within a micro-fabricated vapour cell.

-
- Chapter 5 introduces a compact Zeeman tunable wavelength reference, which can be used to stabilise and tune the frequency of a laser.
 - Chapter 6 discusses the fabrication of an actively pumped micro-fabricated cell as a vacuum chamber for cold-atoms as well demonstrating a compact laser cooling platform by combining the cell with a micro-fabricated diffractive optic.
 - Chapter 7 covers the development of an elongated vapour cells geometry for two-photon optical clocks.
 - Chapter 8 recaps the conclusions drawn for each study preformed throughout this thesis.

Research output

Publications arising from this work

- **S. Dyer**, P. F. Griffin, A. S. Arnold, F. Mirando, D. P. Burt, E. Riis and J. P. McGilligan "Micro-machined deep silicon atomic vapor cells." *J. Appl. Phys.* 7 October 2022; 132 (13): 134401.

This paper constitutes the basis of chapter 3.

- **S. Dyer**, A. McWilliam, D. Hunter, S. Ingleby, D. P. Burt, O. Sharp, F. Mirando, P. F. Griffin, E. Riis and J. P. McGilligan "Nitrogen buffer gas pressure tuning in a micro-machined vapor cell." *Appl. Phys. Lett.* 14 August 2023; 123 (7): 074001.

- A. McWilliam, **S. Dyer** D. Hunter, M. Mrozowski, P. F. Griffin, J. P. McGilligan and E. Riis "Longitudinal Cs ground-state spin-relaxation minimization through buffer gas depletion" In preparation

The above two papers constitutes the basis of chapter 4.

- **S. Dyer**, K. Gallacher, U. Hawley, A. Bregazzi, P. F. Griffin, A. S. Arnold, D. J. Paul, E. Riis and J. P. McGilligan "Chip-Scale Packages for a Tunable Wavelength Reference and Laser Cooling Platform." *Phys. Rev. Appl.* 5 April 2023; 19 (4): 044015

This paper constitutes the basis of chapter 5 and 6.

Conferences

- 2022 Joint Conference of the European Frequency and Time Forum and IEEE International Frequency Control Symposium (EFTF IFCS), Paris, France. (**Poster presentation**)
- International Network for Micro-Fabricated Atomic Quantum Sensors workshop 1, Glasgow, UK. (**Poster presentation**)
- 2023 Joint Conference of the European Frequency and Time Forum and IEEE International Frequency Control Symposium (EFTF IFCS), Toyama, Japan. (**Poster presentation**)
- International Network for Micro-Fabricated Atomic Quantum Sensors workshop 2, Estes Park, Colorado, USA. (**Oral presentation**)

Chapter 2

Atomic physics

Throughout this thesis absorption spectroscopy of alkali metal atoms is commonly employed to evaluate micro-fabricated vapour cells. Therefore this chapter will provide a basic overview of atomic structure, absorption spectroscopy and saturation absorption spectroscopy.

2.1 Atomic Structure

Alkali metal atoms have a relatively simple hydrogen like atomic structure due to their single valance electron. This electron can occupy orbitals shells with orbital angular momentum L , which can occupy integer values from $0 \leq L \leq n - 1$, where n is the principal quantum number. These orbitals are typically denoted by S($L=0$), P($L=1$), D($L=2$) etc. The electron also has an intrinsic angular momentum $\frac{\hbar}{2}$ corresponding to a spin quantum number $S = \pm\frac{1}{2}$, which can couple to L giving rise to a total orbital angular momentum J , that can occupy integer values between $|L - S| \leq J \leq |L + S|$. This coupling between L and S gives rise to a splitting of the orbitals referred to as fine structure with energy levels of the form $^{2S+1}L_J$. This fine structure results in the doublet lines D₁ and D₂, which are characteristic of all alkali metal atoms. In the specific case of Rb, where $n=5$ the D₁ line corresponds to the $5S_{1/2}$ to $5P_{1/2}$ transition, while the D₂ line corresponds to the $5S_{1/2}$ to $5P_{3/2}$ transition.

A further hyperfine splitting of the atomic energy levels can occur through

the coupling of J with the nuclear spin I , which gives rise to the total atomic angular momentum F that can occupy the values between $|J - I| \leq F \leq |J + I|$. For the D₂ line of ⁸⁷Rb with $I=3/2$, the $5P_{3/2}$ state splits into four hyperfine levels $F' = 0, 1, 2$ and 3 . The hyperfine energy levels for the D₁ and D₂ lines of ⁸⁷Rb are illustrated in Fig. 2.1.

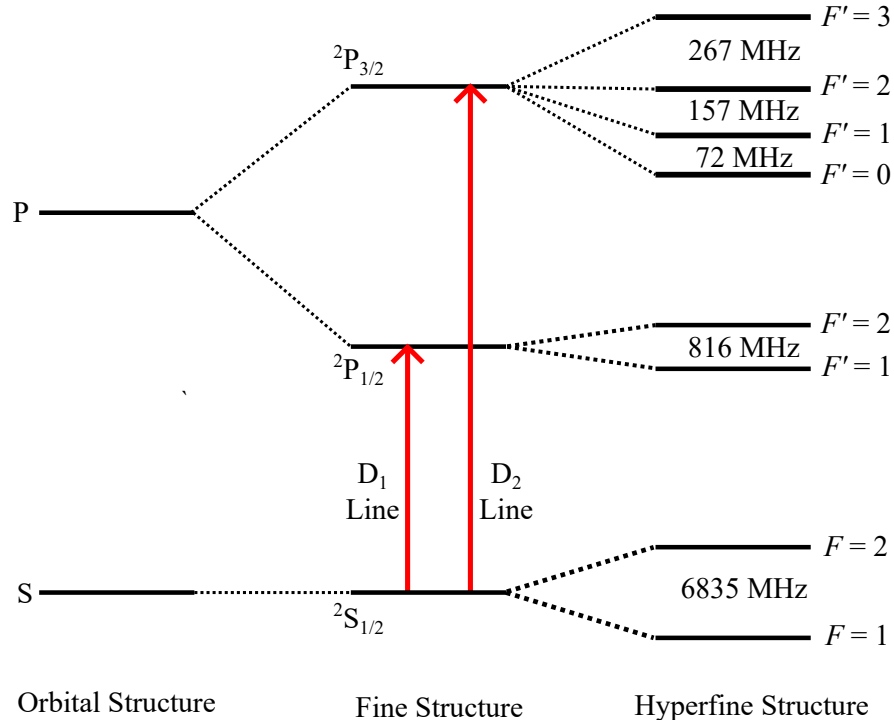


Figure 2.1: Hyperfine atomic structure for the D₁ and D₂ lines in ⁸⁷Rb.

Each hyperfine energy level is comprised of $2F+1$ degenerate Zeeman sub-levels typically denoted as m_F levels ranging in value from $-F$ to F . In the presence of a static magnetic field, the degeneracy of these m_F levels will be lifted. For the case of a weak magnetic field, the m_F levels will experience a linear energy shift of the form,

$$\Delta E_{F,m_F} = g_F \mu_B m_F B \quad (2.1)$$

where μ_B is the Bohr magneton, B is the applied magnetic field and g_F is the hyperfine Landé g factor, given by,

$$g_F = g_J \frac{F(F+1) - I(I+1) + J(J+1)}{2F(F+1)} + g_I \frac{F(F+1) + I(I+1) - J(J+1)}{2F(F+1)} \quad (2.2)$$

where g_J is the Landé g factor and g_I is the nuclear g factor [24–26].

For optical transitions due to the conservation of angular momentum only transitions that obey the electric dipole selection rules [27] are allowed. In the case of the D lines in Rb the important rules are $\Delta F = 0, \pm 1$ and $\Delta m_F = 0, \pm 1$.

2.2 Absorption Spectroscopy

When a near resonant light field interacts with an ensemble of atoms within a vapour cell it will experience an attenuation, which is described by the Beer-Lambert law. Here we follow the description provided by Siddons *et al* [28] where the fraction of transmitted light T through this vapour cell can be written as,

$$T = \exp\left(-L \sum \alpha_i\right), \quad (2.3)$$

where L is the interaction length and $\sum \alpha_i$ is the total absorption coefficient, which is obtained by summing over the absorption coefficient α for each transition for each species within the cell. This is given by,

$$\alpha = -N k C_F^2 d^2 \frac{1}{\hbar \epsilon_0} \frac{1}{2(2I + 1)} s(\Delta) \quad (2.4)$$

where N is the number density of the atomic ensemble, k is the wave vector of the light field and $s(\Delta)$ is the spectral profile of the atomic transition, where $\Delta = \omega - \omega_0$ is the detuning of the light field with respect to the atomic transition's frequency ω_0 . The factor of $2(2I + 1)$ accounts for the degeneracy of the ground states assuming the atomic population is evenly distributed amongst the Zeeman sub-levels.

The strength of a hyperfine transition is given by $C_F^2 d^2$, where C_F^2 is the sum of the transition strengths $c_{m_F}^2$ for each transition between Zeeman sub-level within a given hyperfine transitions and d is the reduced dipole matrix element, which for the D₂ line in Rb is $d=5.177e a_0$ where a_0 is the Bohr radius [28]. The values for d and c_{m_F} are tabulated by D. Steck for the D lines of ⁸⁷Rb, ⁸⁵Rb and Cs [24–26].

2.2.1 Spectral Profile

The spectral profile of an atomic transition is dependent on a variety of broadening mechanisms however, here for simplicity we only consider the case of the natural and Doppler broadening mechanisms. The natural broadening of the atomic transition arises due to the spontaneous nature of the decay of an atom in an excited state down to a ground state. The population of the excited state exhibits an exponential decay with a time constant τ referred to as the lifetime of the excited state. This exponential decay results in a homogeneous broadening of the atomic transition with a Lorentzian line shape and full width half maximum (FWHM) $\Gamma_{\text{nat}} = 1/\tau$, which is referred to as the natural width of the transition. In the case of the D_2 line in Rb $\Gamma_{\text{nat}}/2\pi = 6.065$ MHz [24].

A thermal ensemble of atoms will occupy a range of velocities, which leads to a Doppler broadening. When a photon interacts with a moving atom it will experience a Doppler shift of $\vec{k} \cdot \vec{v}$, where \vec{v} is the velocity of the atom. This Doppler shift can lead to the absorption of off resonant photons and subsequently a broadening of the spectral line. The velocity distribution of the atomic ensemble along one dimension can be described by the Maxwell-Boltzmann distribution,

$$P(v) = \sqrt{\frac{m}{2\pi k_B T}} e^{-\frac{mv^2}{2k_B T}}, \quad (2.5)$$

where m is the mass of the atom, k_B is the Boltzmann constant and T the temperature of the ensemble in Kelvin. This velocity distribution results in an inhomogeneous broadening of the atomic transition with a Gaussian line shape with a linewidth given by,

$$\Gamma_D = \omega_0 \sqrt{\frac{8k_B T}{mc^2}}. \quad (2.6)$$

In the case of Rb vapour at 20 °C the D_2 line will experience a Doppler broadening of $\Gamma_D \approx 2\pi \cdot 500$ MHz.

Due to the Lorentzian and Gaussian broadening mechanisms at play the line shape of the atomic transition is described by a Voigt profile, which is a convolution of the two line shapes. This profile can be expressed in an analytical

form [29],

$$V(\Delta) = \frac{2\sqrt{\ln 2/\pi}}{\Gamma_D} w\left(\frac{2\sqrt{\ln 2/\pi}(\Delta - i\Gamma_{\text{nat}}/2)}{\Gamma_D}\right), \quad (2.7)$$

where w is the complex complementary error function given by,

$$w(x) = \exp(-x^2) \operatorname{erfc}(-ix), \quad (2.8)$$

This analytical solution can be used for calculating and fitting atomic spectra [30]. However, fitting with this method can be computationally challenging, so we instead use the pseudo-Voigt function instead. The pseudo-Voigt function has been empirically derived [31] and takes the form of a weighted sum of the Lorentzian and Gaussian profiles each with a FWHM Γ_V , which is expressed as,

$$V(\Delta, \Gamma_L; \Gamma_G) = c_L L(\Delta) + c_G G(\Delta), \quad (2.9)$$

where c_L and c_G are the weighting factors for the Lorentzian and Gaussian profiles given by [31],

$$c_L = 0.68188 + 0.61293d - 0.1838d^2 - 0.11568d^3, \quad (2.10)$$

$$c_G = 0.3246 - 0.61825d - 0.17681d^2 + 0.11568d^3, \quad (2.11)$$

where $d = (\Gamma_L - \Gamma_G) / (\Gamma_L + \Gamma_G)$ is a dimensionless factor and Γ_V is given by,

$$\Gamma_V = 0.5346 \Gamma_L + \sqrt{0.2166 \Gamma_L^2 + \Gamma_G^2}. \quad (2.12)$$

In the scenario discussed here, where we only consider the natural and Doppler widths, the Voigt profile is dominated by the Gaussian line shape around the line centre. However, there are cases where additional broadening mechanisms such as pressure broadening can result in the Lorentzian line shape being dominant such as in chapter 4.

2.2.2 Number Density

If there are condensed droplets of alkali metal present within the cell the vapour phase can be described as saturated and the Rb vapour pressure P_v (Torr) within

the cell is given by [24],

$$\log_{10} P_v = \begin{cases} 2.881 + 4.857 - \frac{4215}{T}, & T < 312.6 \text{ K} \\ 2.881 + 4.312 - \frac{4040}{T}, & T > 312.6 \text{ K} \end{cases}, \quad (2.13)$$

where T represents the coldest point of the vapour cell. This vapour pressure can then be used with the ideal gas law to determine the number density $N = 133.323 \frac{P_v}{k_B T}$ [28]. The factor of 133.323 converts the vapour pressure from Torr to pa. This imposes a strong relation between transmission through a vapour cell and the cell temperature. In the case of rubidium in its natural abundance this density is separated into 27.8% ^{87}Rb and 72.2% ^{85}Rb .

2.2.3 Absorption Profile

The Rb D₂ absorption profile can be simulated by using Eq.2.3 and 2.4 alongside the relative transition frequency and strength for each transition, which are collated in Table.2.1 and 2.2 for ^{87}Rb and ^{85}Rb respectively [28] .

Transition	ν_0 (MHz)	C_F^2
$F=2$ to $F'=1$	-423.79	1/18
$F=2$ to $F'=2$	-266.85	5/18
$F=2$ to $F'=3$	0	7/9
$F=1$ to $F'=0$	6338.66	1/9
$F=1$ to $F'=1$	6410.89	5/18
$F=1$ to $F'=2$	6567.83	5/18

Table 2.1: The relative transitions frequency ν_0 and transition strength C_F^2 for the D₂ line in ^{87}Rb .

Transition	ν_0 (MHz)	C_F^2
$F=3$ to $F'=2$	939.97	10/81
$F=3$ to $F'=3$	1003.39	35/81
$F=3$ to $F'=4$	1124.35	1
$F=2$ to $F'=1$	3946.71	1/3
$F=2$ to $F'=2$	3975.97	35/81
$F=2$ to $F'=3$	4039.40	28/81

Table 2.2: The relative transitions frequency ν_0 and transition strength C_F^2 for the D₂ line in ⁸⁵Rb.

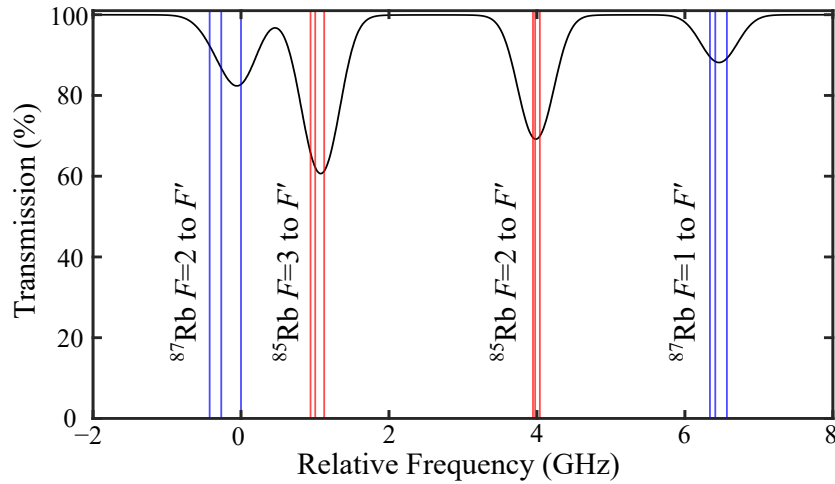


Figure 2.2: Theoretical absorption of the D₂ line in Rb for a room temperature vapour cell with a 7 cm path length. The red vertical lines represent ⁸⁵Rb transitions and the blue lines ⁸⁷Rb transitions.

The simulated D₂ absorption profile is shown in Fig.2.2 for a 7 cm long Rb vapour cell at 21 °C containing a natural abundance of Rb. The absorption profile for the D₁ and D₂ lines in alkali metals can be easily calculated with the ElecSus software [30] developed by the Quantum, Light and Matter group at Durham University. It is important to note that in this absorption model we have not considered the effects of saturation of the atomic transition or hyperfine pumping [32] as such this simulated spectra is only valid for a weak light field.

2.3 Saturation Absorption Spectroscopy

Due to Doppler broadening the individual hyperfine transitions cannot be resolved in room temperature Rb vapour as the Doppler width is greater than the frequency spacings of the excited states as can be seen in Fig.2.2. A simple technique used to resolve individual transitions much closer to their natural width is saturation absorption spectroscopy.

This technique uses two counter propagating beams traveling along z passing through a vapour cell, which experience an equal but opposite Doppler shift with respect to each other such that they only address the same atoms when $v_z = 0$. These atoms are referred to as the zero-velocity class. Assuming a two-level atom in steady state the number of photons an atom can absorb per second is given by the scattering rate $R_{sc}(I, \Delta)$. This rate is given by,

$$R_{sc}(I, \Delta) = \frac{\Gamma}{2} \frac{I/I_{\text{sat}}}{1 + I/I_{\text{sat}} + (2\Delta/\Gamma)^2}, \quad (2.14)$$

where I is the intensity of the pump beam, I_{sat} is the saturation intensity of the transition and Δ is the detuning with respect to the atomic transition.

The beams are typically configured to have a strong pump beam to saturate the transition and a weak probe beam to monitor transmission through the cell. When the two beams resonantly address this zero-velocity class, the ground state population is depleted by the pump beam and an increase in transmission around the atomic transitions is observed by the probe beam as demonstrated in Fig.2.3 for transitions from $F=3$ in ^{85}Rb .

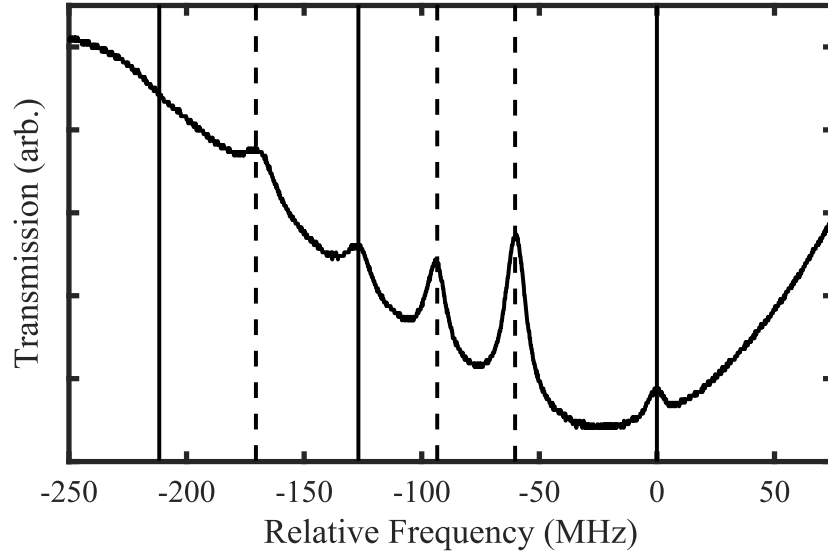


Figure 2.3: Measured saturation absorption spectroscopy of the ^{85}Rb D_2 $F=3$ Doppler broadened envelope for interrogating beams with a 0.75 mm beam waist ($1/e^2$ radius) and peak intensity of $\approx 6 \text{ mW/cm}^2$ with a relative frequency axis with respect to the $F=3$ to $F'=4$ transition. The solid vertical lines represent F to F' transitions and the dashed vertical lines represent cross-over resonances.

Although the technique is called saturation absorption spectroscopy the effect of hyperfine pumping [33] is also key to the formation of these sub-Doppler resonances. This pumping mechanism arises due to the chance that atoms in the excited state will spontaneously decay into a ground state, which is not resonant with the light field increasing transmission through the cell. The probability of an atom falling into a dark ground state is dependent on both the power and beam waist of the pump beam. Additionally crossover features can appear halfway between two transitions in the Doppler broadened envelope due to a depletion of the ground state population that occurs when the counter propagating beams are Doppler shifted into resonance with two separate transitions with a common ground-state. These sub-Doppler resonances exhibit a Lorentzian profile and undergo power broadening, resulting in a linewidth broadened by $\Gamma = \Gamma_{\text{nat}} \sqrt{1 + I/I_{\text{sat}}}$ where I_{sat} is the saturation intensity [24,25].

Chapter 3

Micro-fabricated Silicon Vapour Cells

The micro-fabrication of atomic sensors has enabled a revolution in the field deployment and commercialization of chip-scale atomic sensors [13, 34–36]. A critical component at the core of many of these chip-scale devices is the atomic vapour cell, consisting typically of a MEMS based glass-silicon-glass stack bonded under vacuum [11]. Such MEMS cells have been widely explored for compact sensors, forming hermetic seals from both anodic and thermo-compression bonds to provide a mass-producible cell manufacturing solution [11, 37, 38]. While this now mature technology has enabled the transition to miniature components for atomic sensors, the methods of manufacturing silicon have typically limited the available optical path length to around 2 mm. These limitations arise due to dry etch phenomena [39] and challenges associated with long duration wet etch processes [40].

However, a longer optical path length would be beneficial for atomic sensors due to the increased atomic absorption and the associated enhancement in signal-to-noise ratio (SNR). With this in mind, alternative techniques have been explored to increase the optical path length in line-of-sight cells, such as the processing of thick glass body cells [20, 21] or the ultrasonic drilling of thick silicon frames [41].

Here we introduce a micro-machined silicon based vapour cell, manufactured with water-jet cutting to achieve an optical path length of 6 mm in a simple line-of-sight geometry. The step-change from conventional semiconductor fabrication processes to micro-machining for silicon-based vapour cell production greatly reduces the manufacturing costs by mitigating the need for photolithography and etching processes, while providing an increased optical path length to improve the performance of chip-scale atomic sensors.

3.1 Vapour Cell Fabrication

The vapour cells discussed within this chapter were fabricated in collaboration with Kelvin Nanotechnology (KNT). The fabrication process began by water-jet cutting a 6 mm thick silicon wafer to form frames for the vapour cells. This process involved combining high pressure water and abrasive material together into a narrow jet, which cuts through the silicon via erosion. As illustrated in Fig.3.1 inside a water-jet cutter the high-pressure water and abrasive material are combined in a mixing chamber, which then passes through a nozzle that sets the diameter of the abrasive jet. The minimum feature size is restricted by the aperture of the nozzle, which can be swapped out to realise different sizes, for this initial demonstration the feature size was limited to 1.5 mm.

The dimensions of the silicon frames are controlled via CAD software, which defines cuts and traverses across the wafer to form arbitrary vapour cell geometries. Once the CAD file is prepared the silicon wafer is located within the bed of the water-jet and the automated cutting process begins, for a 6-inch silicon wafer containing 40 cells this process will take approximately 40 minutes. During water-jet cutting, no protective layer was used to cover the upper surface. As a result, chipping of the silicon was observed around the perimeters of the cut regions, with features on the order of $100\ \mu\text{m}$. However, these small defects do not hinder the hermetic sealing of the cell. Additionally, some preliminary measurements have shown that this can be mitigated by wax adhering glass wafers to both bonding surfaces prior to the water-jet process.

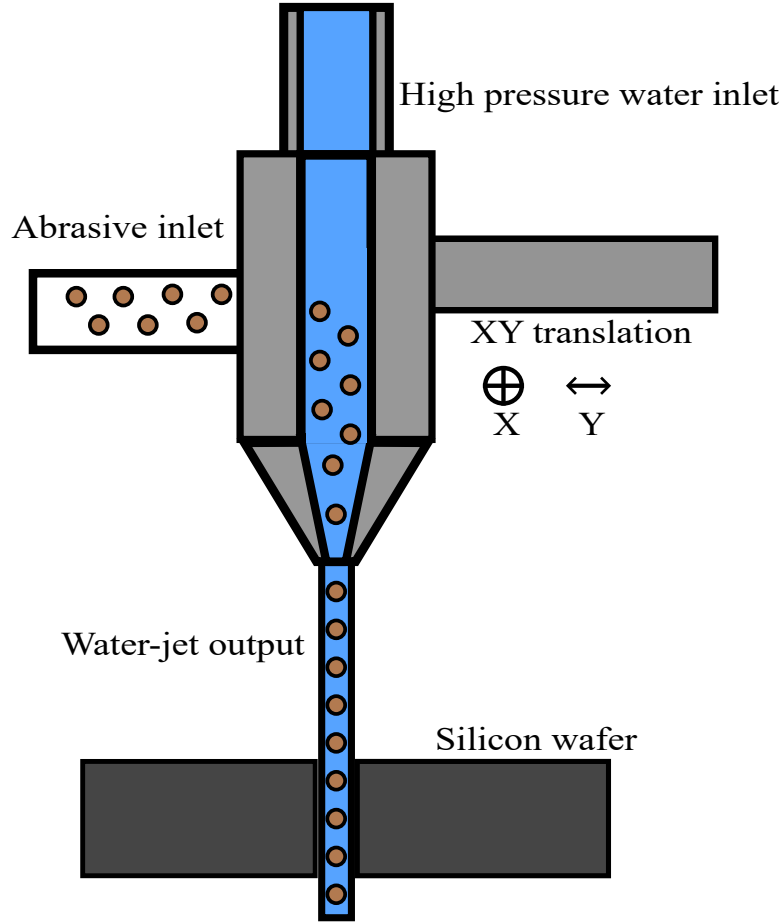


Figure 3.1: Overview of the water-jet cutting process.

Following the water-jet cutting, the silicon wafers are solvent cleaned in an ultra-sonic bath to remove any residual abrasive. After the cleaning stage, the silicon inner wall surface roughness was evaluated with surface profilometry and scanning electron microscopy (SEM). SEM images shown in Fig.3.2 were used to qualitatively evaluate the potential impact of wall roughness on the atomic vapour cell; an increased surface area could consume more alkali metal content and hinder the homogeneity of applied wall coatings that may be required in later applications. The surface profilometry measurements determined an arithmetic average wall roughness of $R_a = 5.9 \mu\text{m}$. While this wall roughness is comparable to recent work in additively manufactured vacuum chambers [42], it remains orders of magnitude larger than the wall roughness achievable for deep reactive-ion etching (DRIE), with short etch depths ($\leq 100 \mu\text{m}$) achieving $R_a = 5 \text{ nm}$, [39, 43] and deep etched silicon (1.4 mm) demonstrating $R_a = 300 \text{ nm}$ [22]. In

future applications, chemical smoothing of the inner walls can be applied if the wall roughness is found to hinder the atomic vapour cell's long-term performance [22].

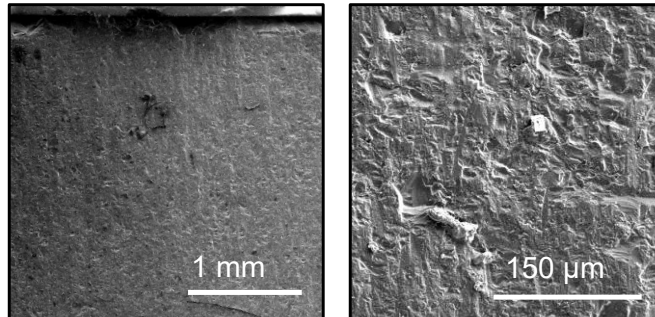


Figure 3.2: Scanning electron microscope (SEM) images of an interior wall within the micro-machined silicon cavity.

The next step in vapour cell fabrication is the vacuum encapsulation of the silicon frame. This was achieved by anodically bonding glass wafers to the top and bottom surfaces of the silicon wafer, which provided a hermetic seal without compromising optical access. Here anodic bonding was selected over other sealing techniques such as thermocompression [38] and indium bonding [44] due to its reliability and simple implementation. This process as illustrated in Fig. 3.3 involves stacking a glass wafer on top of the processed silicon wafer and heating the stack to 300°C to increase the mobility of the sodium ions (Na^+) within the glass. Once the stack has reached an equilibrium temperature an electric potential of 1 kV is applied across the stack with the negative electrode against the glass and positive electrode touching the silicon. This electric potential draws the positively charged sodium ions away from the silicon glass interface leaving behind a negatively charged region populated with oxygen anions (O^{2-}) [12]. Overtime the oxygen anions react with the silicon surface to form a layer of silicon dioxide (SiO_2), which acts as a cement adhering the wafers together creating a seal, which is hermetic and mechanically resistant [12].

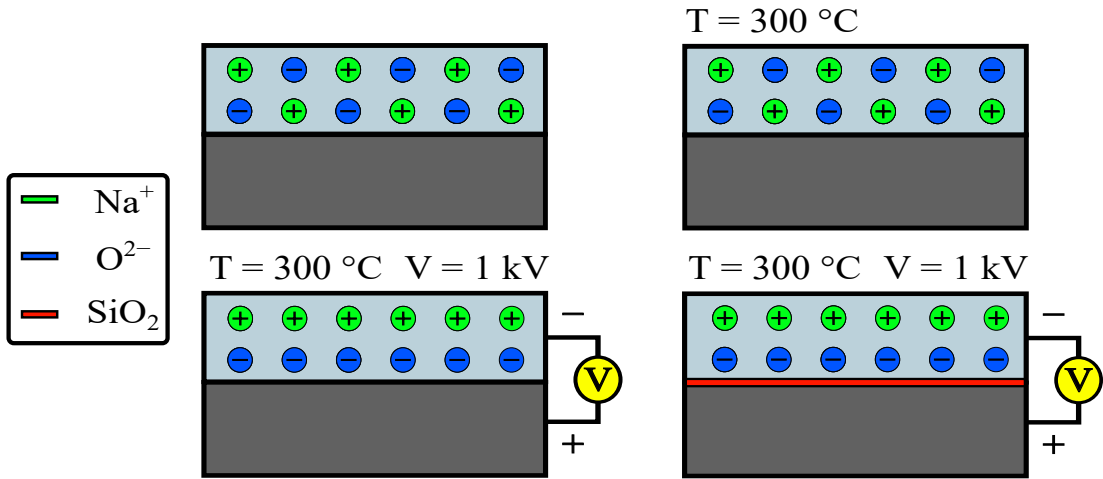


Figure 3.3: Simplified illustration of the anodic bonding process for a silicon and glass wafer stack.

A 0.5 mm borosilicate glass (BSG) wafer was anodically bonded to the base of the processed silicon frame to form a cell preform. This glass is frequently chosen for micro-fabricated vapour cells because its coefficient of thermal expansion (CTE) closely matches that of silicon, alleviating thermal strain on the cell ensuring its structural integrity. An inert atomic source can then be placed into this preform before vacuum encapsulation typically an alkali chloride [11], azide [16] or molybdate [17]. Here we elected for the latter specifically the Rb/AMAX/Pill/1-0.6 from SAES getters due to its commercial availability as well as its comparatively cleaner sourcing. This Rb source is composed of a zirconium and aluminium powder mixed to a chromium free Rb precursor to form a pill with a 1 mm diameter [45]. The vapour cell preform was then transferred to a vacuum wafer bonder, which was evacuated to pressures below 10^{-5} mbar and a final 0.5 mm BSG wafer was bonded to the top surface to encapsulate the cell as illustrated in Fig.3.4. Post bonding, the wafer stack was mechanically diced into individual cells with total dimensions measuring $13 \text{ mm} \times 13 \text{ mm} \times 7 \text{ mm}$ (L×W×H). To control the alkali metal vapour pressure, surface mounted resistors adhered to the front and back glass surfaces were used to heat the cell. The steady-state cell temperature was measured with a thermal camera.

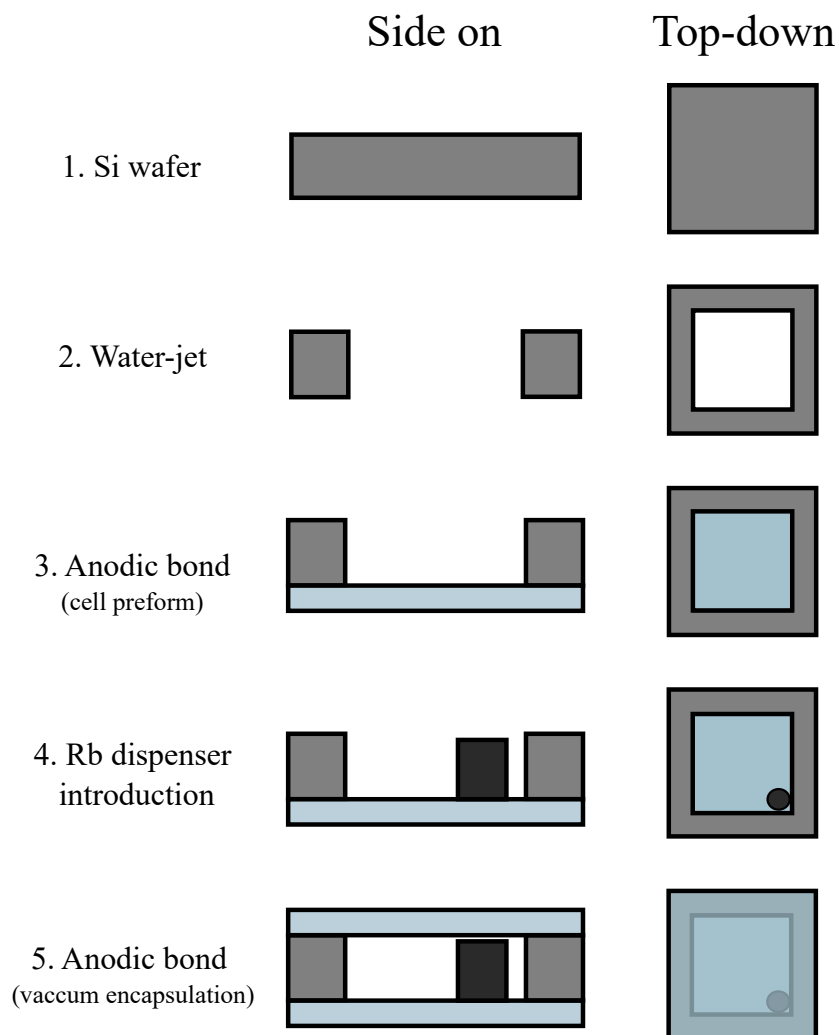


Figure 3.4: Water-jet vapour cell fabrication overview.

3.2 Experimental Setup and Results

To release the Rb within the dispenser into the micro-machined cell the pill dispenser must be heated in excess of $600\text{ }^{\circ}\text{C}$ [46]. Here this was achieved through laser heating the pill source with a 1070 nm ytterbium fibre laser. Light from the fibre was collimated to a Gaussian beam waist of 0.8 mm ($1/e^2$ radius) and then focused with a 50 mm lens to ensure that all of the light was incident onto the 1 mm surface of pill as illustrated in Fig.3.5. Determining the temperature the pill reaches during this laser irradiation was made difficult as the BSG windows filter out infra-red preventing the temperature being inferred from the emitted

black-body radiation. Instead we can only confirm if the pill reached the required temperature via the presence of condensed Rb droplets within the cell.

For the 6 mm thick vapour cells tested here we found that activating the dispenser with 3 W for 10 s was sufficient to release a visible amount of Rb into the cells. While it was noted that the pill could be activated with lower laser powers, the chosen parameters ensured a reproducible activation between the cells under test. Additionally, during preliminary testing it was observed that the Rb accumulated near the pill activation site on the rough walls created by the mechanical micro-machining of the silicon frame. This was overcome by heating the cell 60 °C to encourage migration throughout the cell chamber.

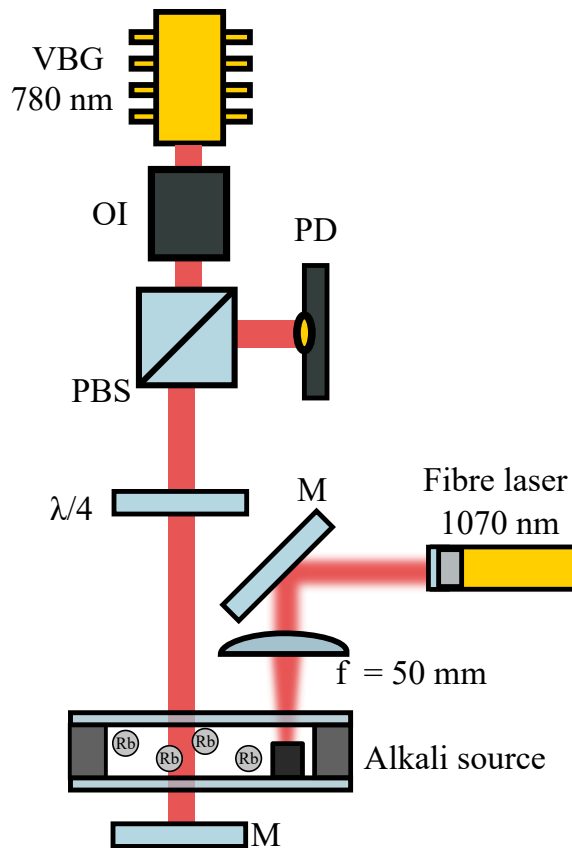


Figure 3.5: Illustration of the optical setup for both laser activation of the alkali pill source and absorption spectroscopy to monitor the presence of Rb. VBG:Volume Bragg Grating. OI:Optical Isolator. PBS:Polarising Beam Splitter. $\lambda/4$:Quarter Waveplate. M:Mirror. PD:Photodiode.

A double-passed absorption spectroscopy setup was assembled around the activation laser to monitor the migration of Rb throughout the cell after activation when heating the cell to 60 °C. This spectroscopy setup was comprised of a volume Bragg grating (VBG) laser scanning across the D₂ line of both ⁸⁷Rb and ⁸⁵Rb. The light from the laser then passed through an optical isolator (OI), which was used to prevent unwanted optical feedback from back reflections off of optical elements. Next the light was then transmitted by a polarising beam splitter (PBS) and circularly polarised with a $\lambda/4$ waveplate before passing through the cell with a 0.75 mm beam waist ($1/e^2$ radius) and peak intensity of 1.6 mW/cm². After the cell the light was retro-reflected along the same path where it passes through the $\lambda/4$ waveplate again. Two passes through the $\lambda/4$ waveplate change the polarisation of the light such that it is now reflected by the PBS and is then detected on a photodiode (PD) and recorded on an oscilloscope.

This measurement was first preformed in a vapour cell with a single chamber design with a square aperture as illustrated in Fig.3.6 (a). During the alkali dispensing process hot material was released from the pill, which reacted with the glass windows causing a discolouration reducing optical access as can be seen in Fig.3.6 (a:i-iii), which is undesirable for atomic sensors where optical access is required to interrogate the atoms within the vapour cell.

A second cell geometry was then investigated to circumvent the discolouration of the cell windows. This is typically achieved by fabricating dedicated regions for pill activation and spectroscopy connected via non-line-of-sight conductance channels [17, 38, 45, 47]. These conductance channels have feature sizes on the order of 200 $\mu\text{m} \times 200 \mu\text{m}$, which yields a poor conductance such that ejected material from the pill is no longer hot enough to damage the glass by the time it reaches the spectroscopy region.

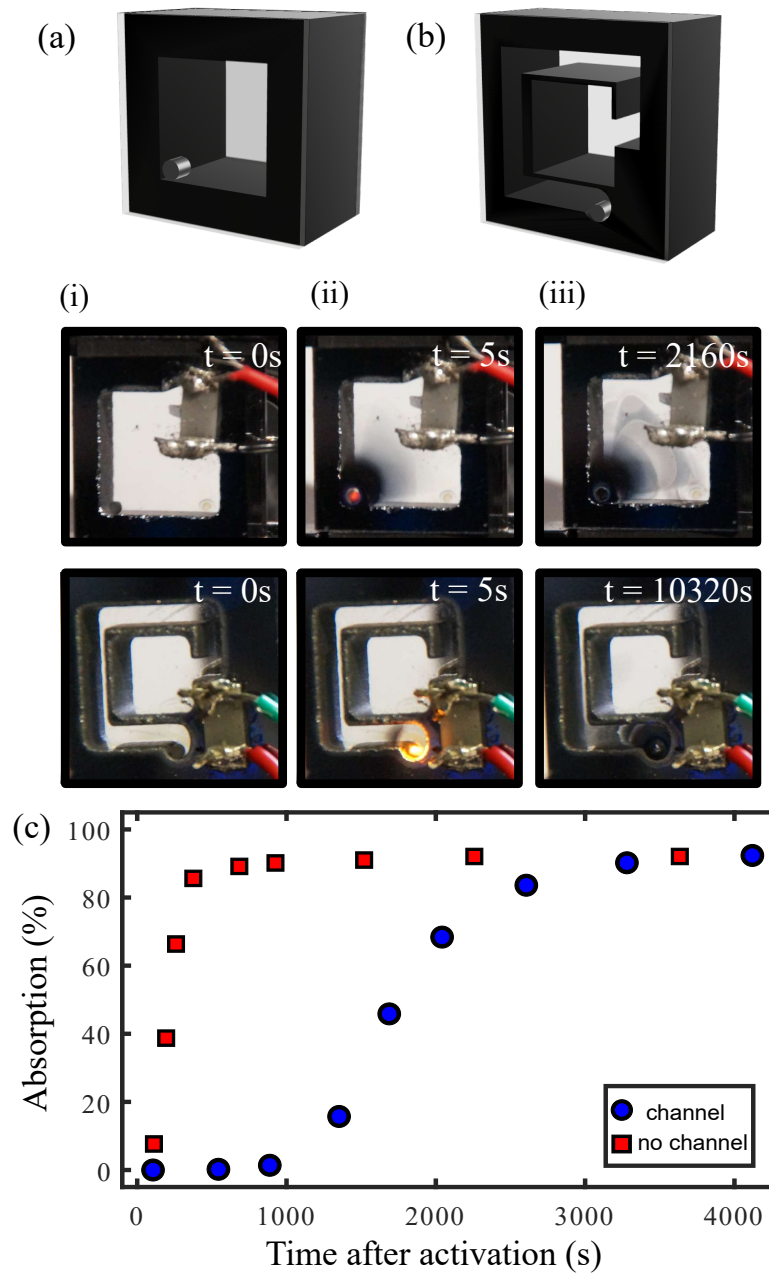


Figure 3.6: Images of micro-fabricated vapour cells (a): single chamber and (b): long meandering channel (i) before, (ii) during and (iii) after laser activation. (c): Simultaneously measured strongest D_2 transition absorption from the ^{85}Rb $F = 3$ ground state in the main chamber during the activation process for a channel and no-channel cell.

The water-jet cutters restricted feature size limited the channel width to 1.5 mm, which resulted in a cross section 220 times larger than conventional dry

etch channels [47]. To compensate for the increased conductance of the water-jet cut channels a 25 mm long meandering path was machined between a designated pill activation region and the main chamber as illustrated in Fig.3.6 (b). The inclusion of the long meandering channel works to confine the glass darkening to the pill activation site leaving the spectroscopy region clear as demonstrated in Fig.3.6 (b:i-iii). This demonstration of the meandering channel was fabricated with an exaggerated length to ensure that no damage from hot material could occur within the spectroscopy chamber however, as can be seen in Fig.3.6 b(iii) this length could be reduced down to several mm without compromising the visibility of the cell windows. The monitored absorption after activation for both cells is shown in Fig.3.6 (c). Here we see that the cell with a single chamber reaches a saturated level of absorption after only ≈ 400 s. Whilst for the cell with the meandering channel it takes ≈ 3000 s for the Rb to diffuse through the meandering channel into the main spectroscopy chamber.

Next we wanted to investigate if the water-jet process left behind any contaminants, which could significantly degrade the cell's internal pressure environment. To this end we built a saturation absorption spectroscopy setup as illustrated in Fig.3.7 (a) in an attempt to resolve sub-Doppler features within the one of the water-jet cells. The VBG laser was required for another experiment, so it was replaced with a home-built external cavity diode laser (ECDL) [48].

The spectrum provided in Fig. 3.7 (b), was obtained with a beam waist of ≈ 2 mm ($1/e^2$ radius) and peak intensity of 5 mW/cm^2 . For this room temperature measurement, we are able to readily observe sub-Doppler resonances with a linewidth of ≈ 20 MHz and observe a peak D_2 absorption of $\approx 7.5\%$ from the ^{85}Rb $F = 3$ ground states. It was noted that the linewidth of the sub-Doppler feature were found to be $\approx \times 1.4$ broader than comparable measurements in a 7 cm glass-blown reference cell over a range of incident intensities in the same experimental setup. The cause of the additional broadening within the micro-fabricated cell was believed to be due to collisions with non-Rb content released during pill activation with a more thorough investigation into the residual gas

within micro-fabricated cells fabricated with water-jet cutting discussed in chapters 4 and 7. These results indicate that the water-jet fabrication process does not leave behind a contaminants within the cell, which can significantly degrade the vacuum within the cell.

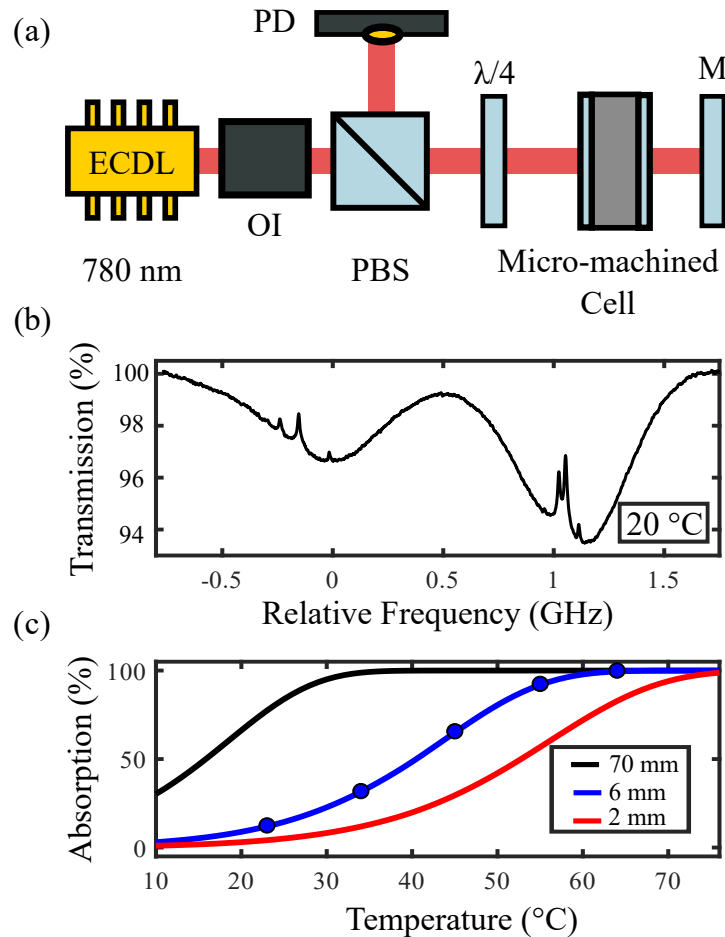


Figure 3.7: (a): Experimental setup for absorption spectroscopy in a micro-fabricated cell. ECDL:External Cavity Diode Laser. OI:Optical Isolator. PBS:Polarising Beam Splitter. $\lambda/4$:Quarter Waveplate. M:Mirror. PD:Photodiode. (b): Typical D_2 line saturated absorption spectrum (single-shot) for the 6 mm meandering micro-machined cell at room temperature. (c): Peak absorption from the ^{85}Rb $F = 3$ ground state Doppler-broadened profile as a function of temperature for retro-reflected vapour cells of 7 cm (black), 6 mm (blue) and 2 mm (red) path-lengths. Blue data points represent measurements taken with the meandering 6 mm vapour cell.

Finally, we monitored the transmission through the 6 mm thick cell in a double-passed configuration as a function of cell temperature to demonstrate the advantages of the increased path length. Additionally the experimental results are then compared against the simple absorption model discussed in chapter 2. For these measurements, we used the same experimental setup as shown in Fig.3.7 with a beam waist of ≈ 2 mm ($1/e^2$ radius) and a peak intensity of $I=0.2$ mW/cm², which were used to reduce the influence of saturation and hyperfine pumping effects [32], which are not considered within the absorption model used here [28].

Fig.3.7 shows the peak absorption of the ⁸⁵Rb $F = 3$ ground state as a function of the measured cell temperature. The blue data points and curve show the measured and theoretically expected absorption at various temperatures for a 6 mm cell length respectively. The 6 mm cell data are compared to theoretical curves for a typical 7 cm long glass blown cell (black), and a 2 mm path length micro-fabricated cell (red). We observed good correlation between experimental and theoretical absorption indicating that the vapour cell is sufficiently filled with Rb. For an operation temperature of 47 °C, the 6 mm cell is capable of achieving the same absorption level as a room temperature 7 cm cell, while the 2 mm cell would require heating to 60 °C.

3.3 Conclusion and Future Work

In this chapter we have demonstrated the suitability of deep micro-machined silicon frames for the production of micro-fabricated atomic vapour cells. While the first demonstration has a silicon feature width limitation of 1.5 mm, the inclusion of a meandering channel has been demonstrated to sufficiently restrict unwanted glass discoloration from the pill activation process outside of the main chamber, for unhindered optical interrogation. The increased optical path length was demonstrated in saturated absorption spectroscopy, with an atomic absorption significantly larger than is achievable in standard 2 mm micro-fabricated vapour cells. The manufacturing simplicity and cost reduction of this technique makes

this a highly attractive route for macro-scale cell fabrication in atomic sensors where increased optical path lengths are desired. Consequently, this fabrication technique was employed for the fabrication of cells featured in chapters 4,6,7.

Chapter 4

Nitrogen Buffer Gas Pressure Tuning

Many atomic clocks and magnetometers are based on building a spin-coherence within an atomic ground state [4, 35, 49, 50] and therefore, their performance is critically dependent on the lifetime of this coherence. In vapour cell-based devices, the coherence time is constrained by the ballistic motion of the atoms, resulting in collisions with the cell walls that induce relaxation. For vapour cells with compact geometries such as micro-fabricated cells, this effect can be the dominant factor limiting device performance [51].

The rate of relaxation from wall collisions can be reduced by several methods. These include altering the dimensions of the cell [52], employing anti-relaxation coatings such as paraffin [53], which allows an atom to experience thousands of wall collisions before relaxing, or introducing an inert buffer gas, such as He, Ne, N₂ or Ar, into the cell, which, through collisions, modify the motion of the atoms from ballistic to diffuse.

For micro-fabricated cells the main technique employed to reduce the relaxation rate from wall collisions is to introduce buffer-gas into the vapour cell before sealing [21, 49, 54]. However, atom-buffer gas collisions also have a weak decohering effect on the atoms such that at high buffer gas pressures this can become the dominant relaxation mechanism [37]. Due to these competing effects, there

is an optimal buffer gas pressure for a particular cell design, which provides a minimum relaxation rate [10, 55]. This is an important consideration when designing a vapour cell for an atomic device to maximise performance. Models exist for these relaxation mechanisms and are described in [55]. Following the description provided in [55], we consider a cylindrical vapour cell, which has a 6 mm path length and diameter, containing Cs atoms in a N₂ buffer gas environment, operating at a temperature of 50 °C.

The relaxation rate arising from wall collisions γ_{rmWC} (assuming a cylindrical cell geometry) is given by [55],

$$\gamma_{WC} = \left[\left(\frac{\pi}{t} \right)^2 + \left(\frac{2.405}{r} \right)^2 \right] \frac{D_{0:\text{Cs-N}_2}}{n_{\text{N}_2}} \sqrt{\frac{T}{273.15K}}, \quad (4.1)$$

where t and r represent cell thickness and radius respectively, $D_{0:\text{Cs-N}_2}$ is the diffusion of Cs atoms in N₂ (given at 1 amg and 273 K), n_{N_2} is the number density of N₂.

The relaxation rate arising from Cs-N₂ collisions is given by [55]:

$$\gamma_{BC} = \eta n_0 \sigma_{\text{Cs-N}_2} \bar{v}_{\text{Cs-N}_2}, \quad (4.2)$$

where $\sigma_{\text{Cs-N}_2}$ is the cross-section of the Cs-N₂ collisions and $\bar{v}_{\text{Cs-N}_2}$ is the relative thermal velocity between the two species [56].

Additional relaxation mechanisms can occur when Cs atoms collide with each other and decohere either via spin-exchange or spin-destruction collisions [55]. Here we only consider the effects of spin-exchange as spin-destruction collisions have a much weaker effect on the relaxation rate [55]. The spin-exchange relaxation rate γ_{SE} is given by [55]:

$$\gamma_{SE} = q_{SE} n_{\text{Cs}} \sigma_{SE} \bar{v}, \quad (4.3)$$

where $q_{SE} = \frac{7}{32}$ is the spin-exchange-broadening factor for Cs [29], n_{Cs} is the number density of Cs, σ_{SE} is the spin-exchange cross-section ($2.2 \times 10^{-18} \text{ m}^{-2}$) and \bar{v} is the relative thermal velocity of the Cs atoms. The total relaxation rate

is then given by the sum of each of these relaxation rates. The calculated results for a range of N_2 buffer gas pressures is illustrated in Fig.4.1 where the optimal buffer gas pressure is indicated with a star.

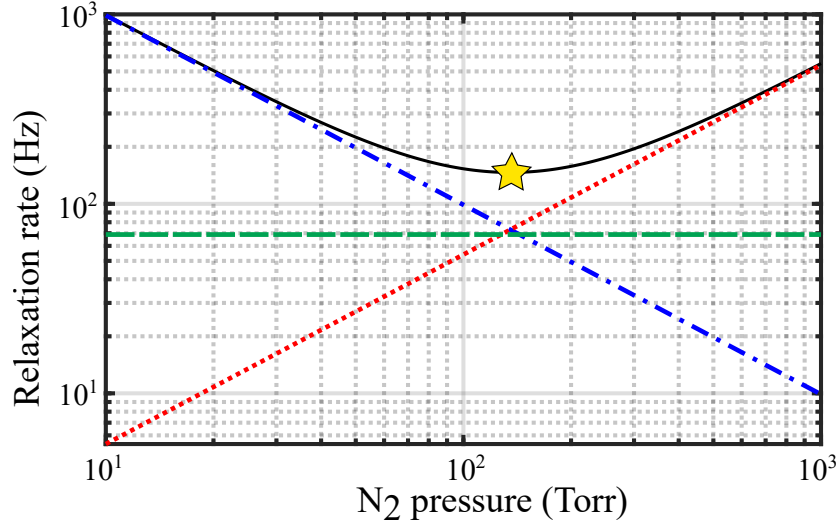


Figure 4.1: Influence of buffer gas pressure on relaxation rates. The red dotted line represents the relaxation rate from Cs- N_2 collisions γ_{BC} , the blue dot-dashed line Cs-wall collisions γ_{WC} , the green dashed line spin exchange collisions γ_{SE} and the solid black line the total relaxation rate γ . The star represents the optimal buffer gas pressure corresponding to the lowest relaxation rate.

However, utilising these models to determine the optimal buffer gas pressure for a vapour cell is made difficult by the range of values reported in the literature for both σ_{Cs-N_2} and $D_{0:Cs-N_2}$ shown in Table.4.1. Additionally, the model for γ_{WC} assumes a cylindrical cell, thus the calculated relaxation rates may be incorrect for alternative cell geometries.

$D_{0:Cs-N_2}$ ($cm^2 s^{-1}$)	σ_{Cs-N_2} ($10^{-26} m^2$)	Ref.
0.12	30	[10]
0.073 ± 0.015	5.52 ± 0.44	[57]
0.22	0.47	[58]
0.098 ± 0.01	5.52 ± 0.55	[59]

Table 4.1: Reported values of $D_{0:Cs-N_2}$ and σ_{Cs-N_2} in literature.

Due to the uncertainty in the estimated optimal buffer gas pressure for a given cell geometry it is best to measure the relaxation rate at a range of buffer gas pressures to determine the optimal pressure for a given cell geometry. However, as buffer gas is typically introduced into micro-fabricated cells by back-filling a vacuum bonder with a buffer gas species and pressure of choice before sealing, all cells derived from the same wafer are restricted to a single pressure. This can require the fabrication of several wafers with different buffer gas pressures, which is both a costly and time consuming endeavor. A recent study from Maurice et al. [60] has demonstrated the ability to increase the buffer gas pressure within a micro-fabricated cell post-sealing via a laser actuated break-seal with demonstrated pressure step sizes of 10 Torr. However, this comes at the cost of additional cell complexity.

Here we investigate the feasibility of finely controlling the N_2 buffer gas pressure within a micro-machined Cs vapour cell by its depletion via the controlled heating of a non-evaporable getter material. This technique could prove useful as a simple route to optimise the buffer gas pressure within a micro-fabricated cell post-sealing, which could prove useful for a variety of applications such as magnetometry [61], quantum memories [62] and atomic wavelength referencing [47].

4.1 Buffer Gas Cell Fabrication

The vapour cells discussed in this chapter were fabricated by KNT. A simplified schematic of the vapour cell bonding procedure is shown in Fig. 4.2. A 6 mm thick silicon wafer was water-jet cut to the desired cavity geometry, with two chambers connected via a meandering channel to avoid glass darkening from pill activation in the main spectroscopy region of the cell as discussed in section 3.6. The processed silicon wafer was first pre-bonded to a borosilicate glass (BSG) wafer. Caesium pill dispensers (SAES Cs/AMAX/Pill/1-0.6) are then deposited within the silicon frame. The final bond was carried out within a vacuum apparatus, with the process illustrated in Fig. 4.2 (a). The pre-formed wafer stack and

upper BSG wafer are held on independent surface electrodes while the vacuum was pumped down to the order of 10^{-5} Torr. Following vacuum evacuation, N_2 was back-filled within the chamber to a pressure of 305 Torr while the wafers are heated to 300°C , shown in Fig. 4.2 (b).

A high voltage was applied across the wafers to anodically bond a hermetic seal for vacuum encapsulation. The wafers are then removed from the chamber and mechanically diced into constituent vapour cells, shown in Fig. 4.2 (c). To create an alkali metal density, the activation laser was set to 3 W for 40 s and was focused onto the centre of the pill dispenser with a 400 mm lens, ensuring that all of the light was confined within the pill's 1 mm surface diameter. After an hour of heating the cell at 100°C to encourage alkali metal diffusion through the meandering channel, the Cs spectra could be observed.

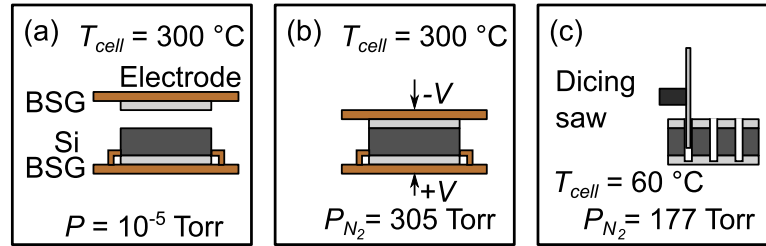


Figure 4.2: (a)-(c): Wafer bonding procedure. Wafers are heated to 300°C and chamber was pumped down to a vacuum pressure of $P = 10^{-5}$ Torr. N_2 was back-filled to the target pressure at this temperature. The wafer was then diced into constituent vapour cells.

4.2 Extracting Buffer Gas Pressure

Collisions with buffer gas species imparts a pressure dependent modification to the optical spectra of the atom. This modification of the atomic spectra can be used to determine both the buffer-gas pressure and the species within a vapour cell. A collision with the buffer gas species results in an atom in the excited state decaying back to the ground state prematurely leading to a broadening [63] of

the Lorentzian component of the spectroscopic profile, which takes the form,

$$\Gamma_L = \Gamma_{\text{nat}} + \gamma_{\text{N}_2} P, \quad (4.4)$$

where Γ_L is the total Lorentzian linewidth, γ_{N_2} is the broadening rate of the buffer gas species and P is the N_2 buffer gas pressure. Collisions with the buffer gas also result in a characteristic shift in the transition frequency. This shift occurs due to interactions between the atoms and the buffer gas species, which arise during collisions, leading to a modification of the atomic structure [37] and shift of the transition frequency, which takes the form:

$$\Delta_{\text{N}_2} = \delta_{\text{N}_2} P, \quad (4.5)$$

where Δ_{N_2} is the induced collisional frequency shift caused by the buffer gas, and δ_{N_2} is the shift rate of the buffer gas species. These effects are evident in the Cs D_1 absorption spectra, depicted in Fig. 4.3, comparing two 6 mm cells at 60°C , one with 150 Torr of N_2 buffer gas and the other with no buffer gas. Here we can observe that the buffer gas cell experiences a red shift due to the presence of N_2 . Additionally, it can be seen that the four hyperfine transitions are no longer individually resolvable, and instead, two broad absorption peaks are observed. This broadening effect also leads to a reduction in the peak absorption.

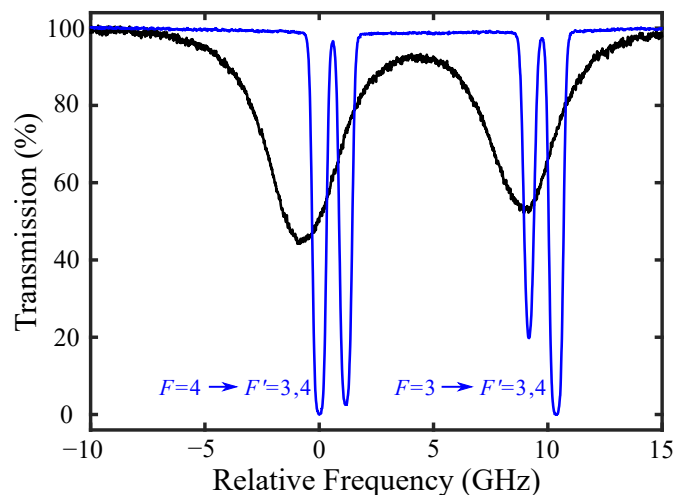


Figure 4.3: Measured spectroscopy of the Cs D_1 line from 6 mm thick cells at 60°C with 150 Torr of N_2 buffer gas pressure (black) and a cell without buffer gas (blue).

The broadening and shift rates for the D₁ line of Cs in the presence of N₂ has been previously characterised [64–66] with a large discrepancy as shown in table.4.2.

γ_{N_2} (MHz/Torr)	δ_{N_2} (MHz/Torr)	$\gamma_{\text{N}_2}/\delta_{\text{N}_2}$	T_r (K)	Ref.
19.51 ± 0.06	-8.23 ± 0.02	-2.37 ± 0.01	294	[64]
15.66 ± 0.08	-7.41 ± 0.02	-2.11 ± 0.01	333	[65]
14.73 ± 0.69	-8.9 ± 0.69	-1.66 ± 0.15	393	[66]

Table 4.2: Reported broadening γ_{N_2} and shift δ_{N_2} coefficients for the D₁ transitions of Cs in the presence of N₂ buffer-gas measured at a reference temperature T_r .

The broadening and shift coefficients are temperature sensitive and are known to follow the power laws [65,67]:

$$\gamma_{\text{N}_2}(T) = \gamma_{\text{N}_2} \left(\frac{T_r}{T} \right)^{1/2} \quad (4.6)$$

$$\delta_{\text{N}_2}(T) = \delta_{\text{N}_2} \left(\frac{T_r}{T} \right)^{0.82} \quad (4.7)$$

where T is the temperature of the cell under-test ($T = 60^\circ\text{C}$) and T_r the reference temperature at which γ_{N_2} and δ_{N_2} were measured. There is an expected ratio of the broadening and the shift for specific buffer gas species, which has a weak temperature dependence. The measured ratio can then be used as validation of the extracted buffer gas pressure as well as the purity of the buffer gas species.

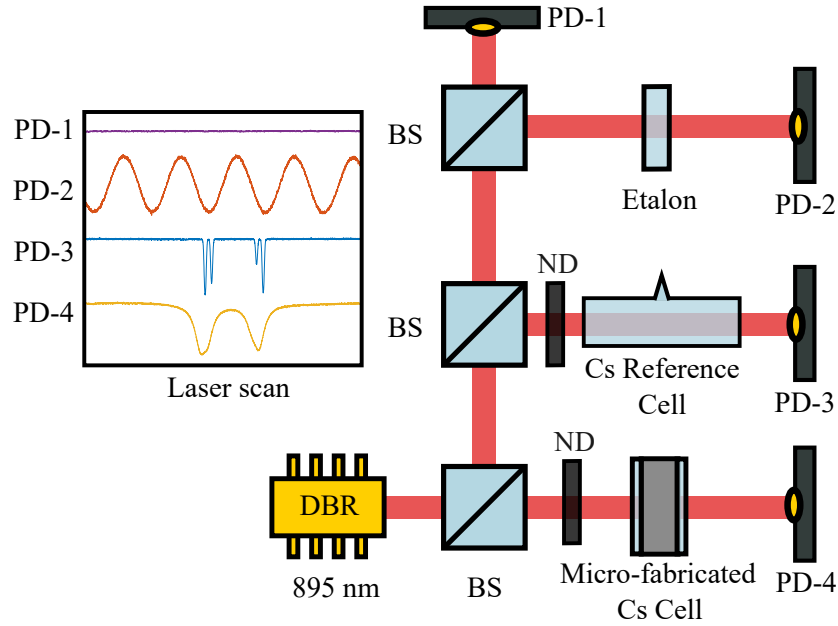


Figure 4.4: Experimental setup for determination of buffer gas pressure within a micro-fabricated cell. DBR:Distributed Bragg Reflector Laser. BS:Beam Splitter. PD:Photodiode. ND:Neutral Density Filter.

An optical spectroscopy setup was assembled shown in Fig.4.4 to determine the amount of N_2 buffer gas within the micro-fabricated cell. This system allowed calibrated measurements of both the buffer gas induced broadening and shift. The setup consisted of an 894.6 nm distributed Bragg reflector (DBR) laser, with a typical linewidth reported by the manufacturer of 1 MHz, which was scanned over approximately 40 GHz at a scan rate of 1 Hz by ramping the laser's set temperature. The laser scan was centred around the D_1 transitions from the $F = 3$ and $F = 4$ ground states of Cs. The light was linearly polarized and split into four paths and detected on separate photodiodes. These paths consisted of an intensity monitor (PD-1), etalon (PD-2), Cs reference cell (PD-3) and the micro-fabricated cell under test (PD-4). Each photodiode was connected to a DAQ device (Picoscope model 5444D) to record data from each photodiode. This spectroscopy setup is an adaption of the setup presented in the thesis of S. Piccolomo [67].

The intensity monitor signal served to compensate for any undesired intensity fluctuations that occurred as the laser's frequency was scanned, which could affect

the other recorded traces. To compensate for this the signal from PD-1 was fit with a 3rd order polynomial and the resulting fit was used to normalise the other recorded traces.

The etalon signal is used to measure and compensate for non-linearities in the laser frequency as the laser's temperature is swept. The etalon is a solid, uncoated glass plate with a free-spectral range of $\nu_{\text{FSR}} \approx 10.2$ GHz and finesse of $F=0.2$ with the transmitted light from the etalon detected on a photodiode (PD-2). The transmission T through the etalon can be described as,

$$T = \frac{1}{1 + F \sin^2 \left(\frac{2\pi\nu}{\nu_{\text{FSR}}} \right)}, \quad (4.8)$$

where ν is the laser frequency. However, due to the low finesse of the etalon its frequency response can be approximated to be,

$$T \approx 1 - \frac{F}{2} \left(1 - \cos \left(\frac{2\pi\nu}{\nu_{\text{FSR}}} \right) \right). \quad (4.9)$$

The recorded signal from PD-2 can then be used to linearise the laser frequency scan and provide a relative frequency reference. This was achieved by fitting the etalon trace with a fit of the form,

$$T = c_1 + c_2 \sin (2\pi(p^n(t) + c_3)). \quad (4.10)$$

Where c_1 represents the offset, c_2 the amplitude, c_3 the phase and p^n an nth order polynomial the coefficients of which are used as frequency scaling factors. By using the extracted polynomial coefficients along with the ν_{FSR} of the etalon a frequency array can be generated. The etalon's ν_{FSR} is known to a high accuracy as it has been calibrated with respect to the well defined hyperfine spacing of the Cs ground states [26] by S. Piccolomo [67].

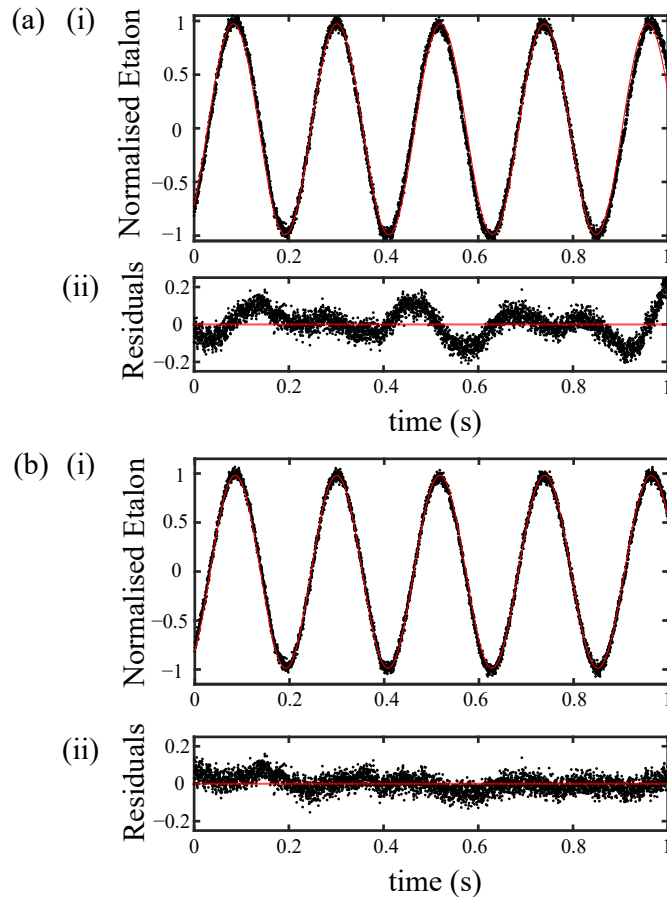


Figure 4.5: (a): (i) Etalon data (black) with a 1st order polynomial etalon fit and residuals. (ii) Residuals (black) and straight line at 0 (red). (b): (i) Etalon data (black) with a 2nd order polynomial etalon fit (red) and residuals. (ii) Residuals (black) and straight line at 0 (red).

Initially, the laser frequency scan was assumed to be linear and a first-order polynomial was employed for fitting. The resulting fit and residuals are depicted in Fig. 4.5 (a). It is apparent that the fitting model doesn't adequately capture the data with higher order structure clearly present in the residuals, which yield an $\text{RMS} = 0.073$. To account for non-linearity in the laser scan, a second-order polynomial was then employed, as depicted in Fig. 4.5(b). This yields a better fit to the etalon data evidenced by the residuals with a reduced $\text{RMS} = 0.045$. However, some high order structure remains within the residuals. In an attempt to completely flatten the residuals higher order polynomials were subsequently employed. They were found to have a negligible effect on the extracted frequency

array and fitting residuals and thus we find a second-order polynomial to be sufficient for our applications. From the error in the second-order etalon fit we estimate a frequency scaling error of $\sigma_{\text{Etalon}} = \pm 7$ MHz.

Now with a relative frequency array provided by the etalon, the next step is to translate this array into frequency with respect to the Cs D₁ line. To this end the third arm was aligned through a room-temperature 7-cm-long Cs reference cell onto a photodiode (PD-3) with a beam waist of 700 μm ($1/e^2$ radius) and an average intensity $I = \frac{P}{\omega_0^2 \pi}$ of ≈ 0.9 mW/cm². The intensity of the interrogation beam was set to be $< I_{\text{sat}} = 2.5$ mW/cm² [26] to prevent power broadening. The reference cell provides an unperturbed spectrum of the Cs D₁ line, which is comprised of 4 hyperfine transitions as can be seen in Fig.4.6. Each of these hyperfine transitions can be readily resolved with simple absorption spectroscopy as the hyperfine spacing of the excited states are greater than the Doppler width $\Gamma_D/2\pi \approx 400$ MHz. These transitions can be used as frequency references as the transition frequencies are well known due to their wide use in atomic physics [26, 68, 69].

i	Transition	C_F^2	ν_0 (GHz)
1	$F=4$ to $F'=3$	7/12	0
2	$F=4$ to $F'=4$	5/12	1.16768
3	$F=3$ to $F'=3$	1/4	9.19263
4	$F=3$ to $F'=4$	3/4	10.36031

Table 4.3: Transition strength for each transition within the D₁ line of Cs and their relative transition frequency with respect to the $F=4$ to $F'=3$.

The signal from PD-3 is first normalised with respect to the off-resonant part of the scan to obtain transmission. Then by fitting the reference cell trace with an absorption profile the relative frequency position of each of the hyperfine transitions can be obtained, and a frequency offset ν_{offset} can be determined. This frequency offset can then be used to modify the relative frequency array into a frequency array with respect to the D₁ line. The absorption profile fit is of

the form of the Beer-Lambert law as previously discussed in chapter 2,

$$T = \exp \left(-L \sum_i^4 \alpha_i (C_F^2, V(\nu_0 + \nu_{\text{offset}}, \Gamma_{\text{nat}}; \Gamma_D)) \right), \quad (4.11)$$

where ν_0 represents the transition frequency of each of the D₁ transitions, C_F^2 their respective transition strengths see Table 4.3 and V represents a pseudo-Voigt function previously discussed in Chapter 2. Here other potential broadening mechanisms are ignored, with the Lorentzian and Gaussian components of the pseudo-Voigt taken to be the natural linewidth $\Gamma_{\text{nat}}/2\pi = 4.5$ MHz and the Doppler width $\Gamma_D/2\pi \approx 400$ MHz respectively.

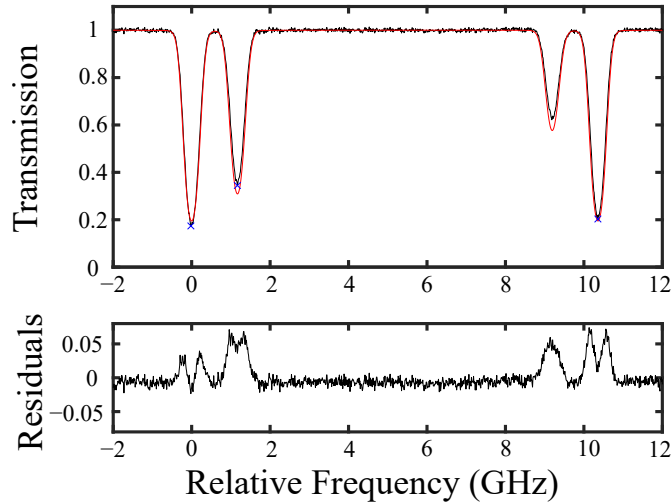


Figure 4.6: Cs D₁ absorption spectra data (black), fit line (red) and residuals.

The resulting fit shown in Fig.4.6 has a discrepancy in the peak absorption of $\approx 5\%$ for each hyperfine transition. This discrepancy is likely caused by a weak retroreflection from the cell's uncoated glass windows, producing small sub-Doppler resonances at the centre of the absorption profiles, which seem to be present within the fitting residuals. From the uncertainty in determining the line centre of each transition a frequency offset error of $\sigma_{\text{Cs ref}} = \pm 5$ MHz was determined. By combing the fitting errors obtained from both the etalon and Cs reference cell traces we obtain a total frequency calibration error $\sigma_{\text{cal}} = \pm 8$ MHz.

Now with a calibrated frequency scan we are able to analyse the absorption spectra obtained from the micro-fabricated cell to extract N₂ pressure. For this

purpose the laser was aligned through the main chamber of the micro-fabricated cell onto a photodiode (PD-4) to record the absorption spectra. The micro-fabricated cell was heated to $60 \pm 1^\circ\text{C}$ to provide a sufficient absorption signal for fitting. The integration beam had a beam waist of $700 \mu\text{m}$ ($1/e^2$ radius) and average intensity of $I = 75 \mu\text{W}/\text{cm}^2$.

The photodiode offset was measured for PD-4 to improve normalisation as this could effect the measured width of the spectra. This was done by heating the micro-fabricated cell to $>100^\circ\text{C}$ such that no resonant light would be transmitted through the cell and the transmission minimum was taken as the photodiode offset. [70]. Here, it was observed that after normalisation using the intensity monitor, residual intensity variations persisted in the off resonant sections of the scan. These variations were attributed to etalons, which had formed due to the reflections between the reflective surfaces within the spectroscopy arm containing the cell. To account for this a 3rd order polynomial was fit to the off resonant part of the scan and the resulting fit was used to re-normalise the scan.

The fitting function used to extract the broadening and the shift was similar to the function described for the reference cell however, in this instance the Lorentzian component of the Voigt was allowed to be broadened by $\Gamma_{\text{N}_2} = \gamma_{\text{N}_2} P$ to account for pressure broadening and the Gaussian Doppler width was constrained to simply the fitting process. By constraining the Doppler width during this fit we estimate an error of $\approx 1\text{MHz}$ from the uncertainty in the cell temperature. Finally, the transition frequency ν_0 was allowed to be shifted by ΔN_2 to account for the pressure induced shift. The resulting fit used for N_2 pressure extraction was of the form,

$$T = \exp \left(-L \sum_i^4 \alpha_i (C_F^2, V(\nu_0 + \Delta\text{N}_2, \Gamma_{\text{nat}} + \Gamma_{\text{N}_2}; \Gamma_{\text{D}})) \right). \quad (4.12)$$

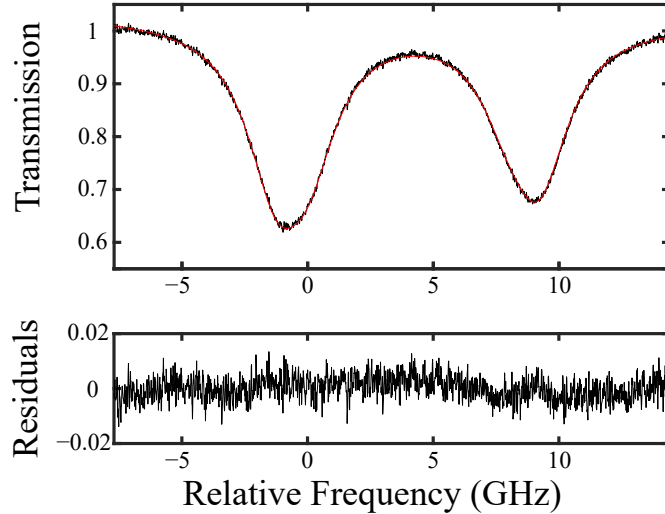


Figure 4.7: Cs D₁ absorption spectra from a micro-fabricated cell filled with N₂ after re-normalising the scan. data (black), fit line (red) and residuals.

The absorption profile and resulting fit for a micro-fabricated cell after alkali dispensing is shown in Fig.4.7. To account for shot-to-shot fluctuations in the fits the extracted values for the broadening and shift were averaged over 5 sequential shots and are tabulated in Table.4.4 for a single cell after alkali dispensing.

$\Gamma_{N_2}/2\pi$ (MHz)	$\Delta_{N_2}/2\pi$ (MHz)	$\Gamma_{N_2}/\Delta_{N_2}$
2654 ± 18	1171 ± 8	-2.23 ± 0.02

Table 4.4: Extracted N₂ induced broadening and shift for a micro-fabricated cell at 60 °C after alkali dispensing.

The measured value for the ratio of $\Gamma_{N_2}/\Delta_{N_2} = -2.23 \pm 0.02$ at 60 °C was closest to the ratio determined by Andalkar *et al.*, [64], which when scaled to our measurement temperature is $\Gamma_{N_2}/\Delta_{N_2} = -2.28 \pm 0.01$. Thus, we use their coefficients for the broadening and shift of $\gamma_{N_2} = 17.6$ MHz/Torr and $\delta_{N_2} = -7.7$ MHz/Torr respectively for a cell at 60 °C. With these coefficients, we obtain an N₂ pressure of 151.3 ± 0.9 Torr from the broadening and 152.6 ± 1.0 Torr from the shift. The final N₂ pressure estimation is taken as the weighted average of the N₂ pressure extracted from both the broadening and the shift from which 152.0 ± 1.3 Torr is obtained.

The vapour cell was filled with N_2 at 300°C with a target pressure of 305 Torr. Through simple extrapolation with the ideal gas law we can roughly estimate the N_2 pressure at the cell measurement temperature of 60°C to be ≈ 170 Torr. The initial pressure reading from this cell was lower than the estimated pressure inferred from the ideal gas law. This discrepancy was attributed to N_2 consumption by the non-evaporable getter material within the pill source during the alkali dispensing process.

4.3 Laser Controlled Gettering

A non-evaporable getter (NEG) is comprised of compressed alloys of reactive materials such as titanium and zirconium, which will react with active gases typically found in vacuum systems (CO , CO_2 , N_2 , O_2 and H_2O) to form stable compounds on the surface of the NEG reducing the vacuum pressure. This gettering process over time saturates the outer surface of the NEG material with bound compounds, significantly reducing its pumping rate [71]. The outer surface can be cleaned via the heating of the NEG material, which allows the stable compounds formed at the surface to diffuse into the bulk of the NEG, leaving behind metal alloy ready to bind more gas. This process is known as activation and typically requires temperatures ranging from $200\text{--}800^\circ\text{C}$ depending on the composition of the NEG material [71]. The consumption of gases such as N_2 is irreversible; i.e. once consumed it cannot return to the vacuum again [72]. The quantity of gas, which diffuses into the bulk of the NEG can be described by the following equation [73]:

$$D = A \exp\left(\frac{-B}{T}\right) \sqrt{t}, \quad (4.13)$$

where A and B are coefficients dependent on the chemical composition of the NEG [72], T represent the activation temperature in Kelvin and t the duration of the activation. Here we can see that the amount of gas that is diffused into the bulk of the NEG is exponentially dependent on the activation temperature but also has a square root dependence on the duration of the activation.

Approximately 67% of the alkali pill source's mass is comprised of NEG material and a previous experiment has demonstrated the removal of 700 Torr of N_2 from a micro-fabricated vapour cell [51]. Here we aim to controllably decrease the N_2 pressure through the heating of the NEG material within the pill dispenser in an attempt to realise fine control of the buffer gas pressure at the Torr level.

To test this hypothesis, the same laser used during alkali dispensing was aligned onto the surface of the pill with the same beam waist and power, whilst the cell remained in the pressure monitoring setup. The beam waist and laser power were unchanged for getter activation as they were sufficient to release Cs from the dispenser. This indicates that the pill reaches a temperature ≥ 600 °C, which should be adequate for activation of the NEG material.

Using the same cell as discussed in section 4.2 with a starting pressure of 152 Torr, the activation laser was turned on for a period of 15 s. Subsequent pressure measurements revealed that the N_2 pressure within the vapour cell had depleted to 135.0 ± 1.4 Torr. After this first successful depletion the buffer gas pressure was continuously monitored whilst shorter activation times of 5 and 10 s were explored with the aim of realising smaller changes in N_2 pressure. At the end of these tests the N_2 pressure was found to be depleted to 113.4 ± 1.4 Torr with spectra taken before and after the tuning process shown in Fig. 4.8 (a). The decrease in N_2 pressure led to a change in the observed lineshape, as the reduction in pressure broadening causes the observed two peaks to split into the four distinct hyperfine transitions.

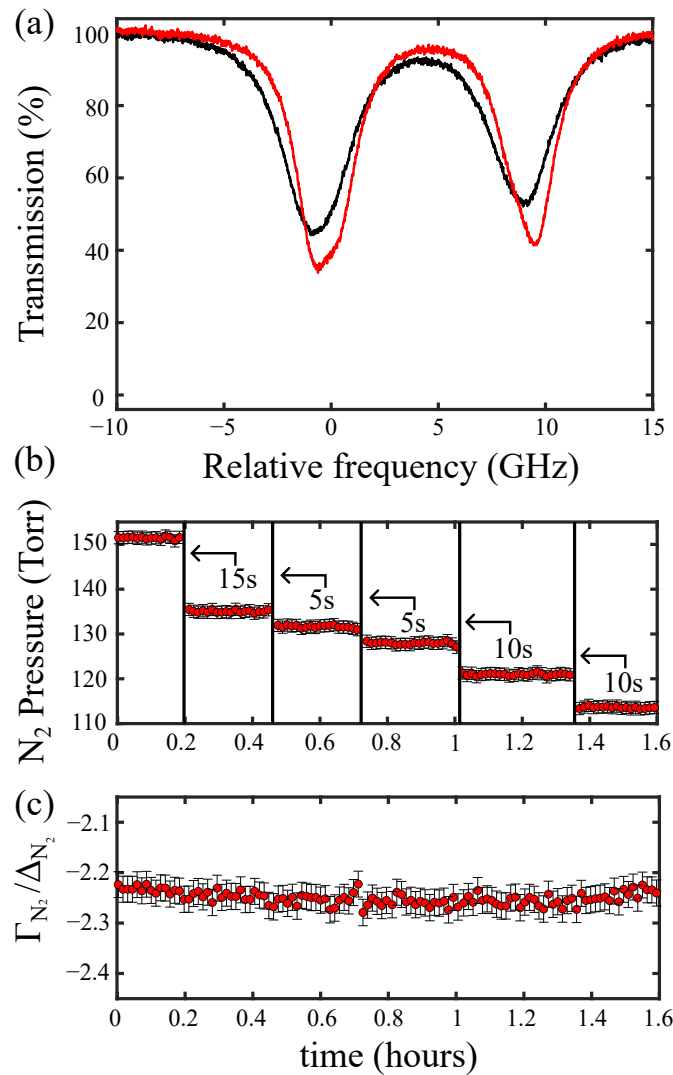


Figure 4.8: (a): Measured spectroscopy of the Cs D₁ line for N₂ pressures of 150 Torr (black) and 110 Torr (red) at 60 ° C. (b): Time sequence of the inferred N₂ pressure as it is decreased with vertical black lines indicating when the 1070 nm laser is on. (c): Ratio of the measured linewidth broadening and frequency shift as a function of time.

The inferred N₂ pressure throughout the gettering process is shown in Fig. 4.8 (b), where the pressure is shown with red data points and each subsequent activation period, indicated by vertical black lines. After each activation period the N₂ pressure was measured for > 20 minutes, over this time there was no observable change in N₂ pressure indicating that the gettering process either stopped due to the saturation of the outer surface of the NEG or the gettering rate was signifi-

cantly reduced to a level not resolvable with the current experimental apparatus over this timescale. The resulting change in N_2 pressure for each exposure time for this NEG material under these specific laser activation parameters is displayed in Table.4.5 with the smallest step being 3.6 ± 2.0 Torr for an activation period of 5 s. We also investigated turning the activation laser on for a brief period of ≤ 1 s to try and get a smaller amount of N_2 , which resulted in a N_2 pressure changes of ≈ 1 Torr.

Activation time (s)	Δ_{N_2} (Torr)
5	3.6 ± 2.0
10	7.2 ± 1.5
15	16.2 ± 1.5

Table 4.5: N_2 depletion for different activation times with 3 W of incident power.

Additionally, throughout the pressure depletion process, the ratio of the broadening and shift was found to remain constant at $\Gamma_{N_2}/\Delta_{N_2} \approx -2.23\pm 0.02$ as shown in Fig. 4.8 (c). This indicates that during repeated activations the alkali dispenser did not release a large quantity of residual gases. However it is worth noting that this argument only holds under the assumption that any potential gas species released has a net ratio, which is different to that of N_2 .

4.4 Optimising Relaxation Rate

After the successful demonstration of the controlled reduction of N_2 via the heating of a NEG, we investigated using this technique to map out the intrinsic relaxation rate of Cs with a micro-fabricated cell as a function of N_2 buffer gas pressure. For this study a 6 mm thick cell with a cubic spectroscopy chamber ($6\text{ mm} \times 6\text{ mm} \times 6\text{ mm}$) was used, as shown in Fig.4.9.

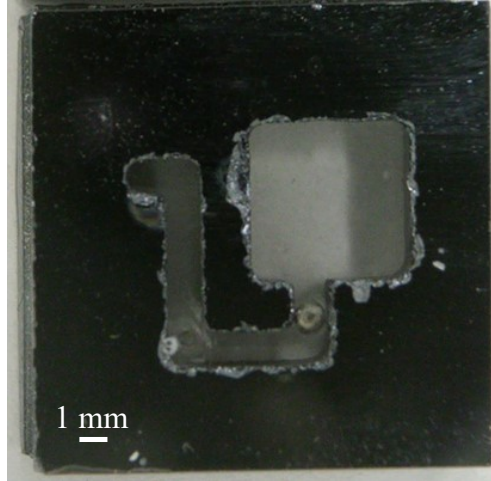


Figure 4.9: The cuboid cell geometry employed in the relaxation rate measurements.

To measure the relaxation rate a free induction decay (FID) magnetometry technique [35,74] was employed. This technique involves optical pumping the Cs atoms within the micro-fabricated cell with circularly polarised light to create a net spin polarisation in the $F=4$, $m_F=4$ ground-state. The pump beam is turned off and the atoms are allowed to freely precess around a transverse magnetic field. The frequency of this precession is the Larmor frequency given by,

$$\omega_L = \gamma_g |\vec{B}| \quad (4.14)$$

where γ_g is the gyromagnetic ratio of Cs [75] and $|\vec{B}|$ is the strength of the transverse magnetic field. This precession can be measured by a weak probe beam with linear polarisation, which will experience a polarisation rotation as the atoms precess. This rotation can then be detected on a balanced polarimeter, with a typical signal shown in Fig. 4.10.

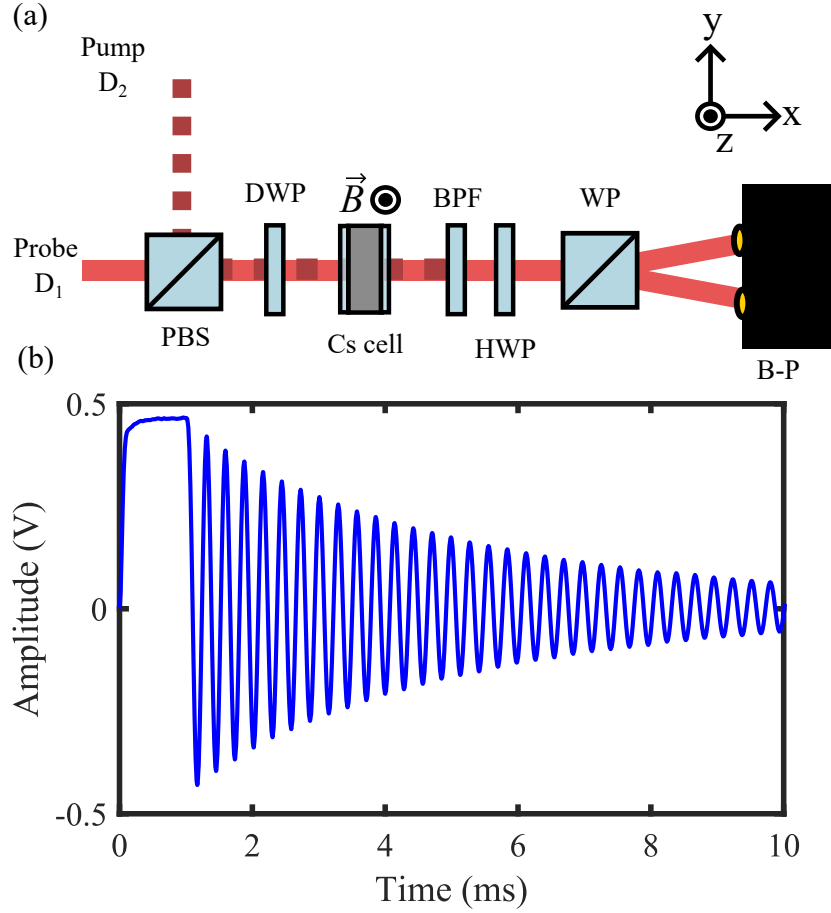


Figure 4.10: (a): FID setup with independent pump and probe beams passing through a micro-fabricated cell with a transverse magnetic field. PBS: polarising beam splitter, DWP: dual-wavelength waveplate. BPF: band-pass filter, WP: Wollaston prism, B-P: balanced polarimeter. (b): Typical FID trace obtained for a 6 mm thick cuboid cell with ≈ 160 Torr of N₂.

The detected signal is then fit with a damped sinusoid of the form,

$$S(t) = A \sin(\omega_L t + \phi) \exp(-\gamma t), \quad (4.15)$$

where A represents the amplitude of the signal and γ the relaxation rate. Due to the effects of power broadening from the probe beam, the relaxation rate will be increased and so to account for this the measurement is repeated at a range of intensities to extrapolate back to the relaxation rate at zero intensity [74]. The FID measurements were carried out by A. McWilliam; more details on the experimental setup and procedure can be found here in his PhD Thesis [56].

For this study the cubic cell was iteratively pressure tuned from a starting pressure of 160 Torr down to 60 Torr. During this process short activation periods of ≤ 5 s were employed until the desired pressure change of ≈ 10 Torr was achieved. Between each pressure reduction the relaxation rate was measured as shown in Fig.4.11.

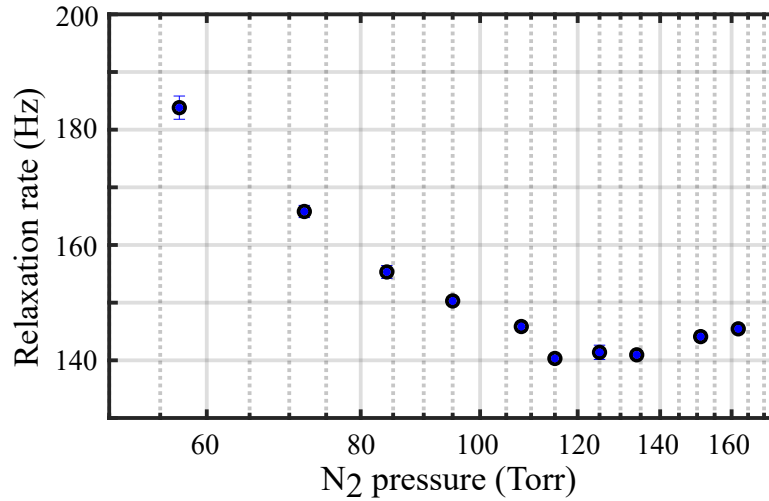


Figure 4.11: Relaxation rate (γ) as a function of N₂ pressure. Blue data points relate to measurements using the cuboid cell.

Initially as the buffer gas pressure was depleted from 162 to 115 Torr we observed that there was a small change in the relaxation rate of < 5 Hz as the rate of Cs-N₂ collisions were reduced. Beyond this point as the N₂ pressure was decreased the relaxation rate increased as the atomic motion became more ballistic increasing the wall collision rate. Through these measurements we observe that the relaxation rate was minimised for this cell geometry at ≈ 140 Hz for N₂ pressures between 115 and 130 Torr.

The preliminary results presented here show that this pressure tuning technique is a promising route to determine the optimal buffer gas pressure to minimise the relaxation rate for different vapour cell geometries, requiring only a single vapour cell opposed to several wafers.

4.5 Buffer Gas Pressure Stability

Next the stability of the N_2 pressure was assessed to determine if the NEG material continued to getter after the activation process had ceased. This is an important consideration when looking to implement these pressure tuned cells into an atomic sensor, such as a magnetometer, as the continued depletion of buffer gas pressure would degrade the sensor performance overtime.

For this study, two cells designated L_1 and L_2 were tuned to $P_{N_2} \approx 100$ Torr at 60°C . After tuning cells L_1 and L_2 were removed from the experimental setup and maintained at 60°C and 120°C respectively. The cells were held at two different temperatures to determine if a higher operational temperature impacted pressure stability, potentially occurring from an increased N_2 diffusion rate into the getter material at higher temperatures. Periodically the cells were returned to the spectroscopy setup and pressure was then measured again at an operational temperature of $\approx 60^\circ\text{C}$.

An issue that arose when returning cells to the spectroscopy setup was that the pressure determined from the broadening was found to be sensitive to changes in cell position. Even subtle adjustments in the cell's placement as it was returned to the setup resulted in deviations of ≈ 10 Torr in the inferred pressure from the broadening. The underlying mechanism for this is not well understood but, it is thought to arise due to changes in the etalons formed within the micro-fabricated cells spectroscopy arm as the position of the cell was moved, which wasn't sufficiently compensated for during the fitting process. However, the pressure extracted from the shift remained largely unaffected, with deviations of < 1 Torr. As such only the pressure determined by the shift was used to monitor the N_2 pressure stability.

Additionally, over the course of the measurement, as cells were swapped into the apparatus, the cell temperature was not consistently recorded. To account for this we looked to infer the temperature of the cell after the fact via monitoring the peak absorption of the $F=4$ to $F'=3,4$ buffer gas broadened transitions.

This required a calibration where the transmission through cell L_1 was tracked as the temperature of the cell was cooled from 66°C to 48°C over a period of 8 minutes. The resulting transmission against temperature calibration curve shown in Fig.4.12 was then used during data analysis to determine the cell temperature from the peak absorption of the $F=4$ to $F'=3,4$ transitions. This transmission to temperature calibration was only taken once for cell L_1 , under the assumption that L_2 would exhibit the same temperature dependence due to its similar buffer gas pressure. Additionally, any potential deviations in buffer gas pressure were presumed to have a negligible effect on the transmission through the cell. This calibration was then used during the fitting process to account for temperature variations, which could effect the extracted buffer gas pressure.

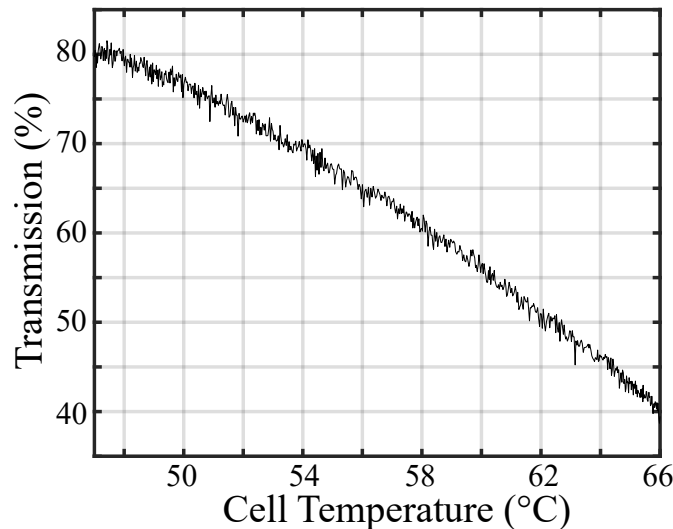


Figure 4.12: Peak transmission of the $F=4$ to $F'=3,4$ buffer gas broadened transitions vs the measured cell temperature for L_1 .

Long term pressure monitoring was carried out for a period of > 100 days with the inferred pressure over this measurement period shown Fig. 4.13 in blue squares and red circles for the cells maintained at 60°C and 120°C respectively. Over the course of the measurement, there was no significant change in the observed N_2 pressure, which remained constant at $\approx 102 \pm 2$ Torr. A linear fit to the cell pressure as a function of time in the cells maintained at 60°C and 120°C provide drifts of $\approx -1.7 \pm 2.1$ mTorr/day and $\approx 0.1 \pm 0.6$ mTorr/day respectively,

consistent with no observable change of buffer gas pressure. From the typical N_2 pressure measurement error of ± 1 Torr an upper bound can be placed on the the observable pressure drift of ≈ 10 mTorr/day. Pressure deviations at this level will have an insignificant effect on the performance of a magnetometer based on the results reported in section.4.4.

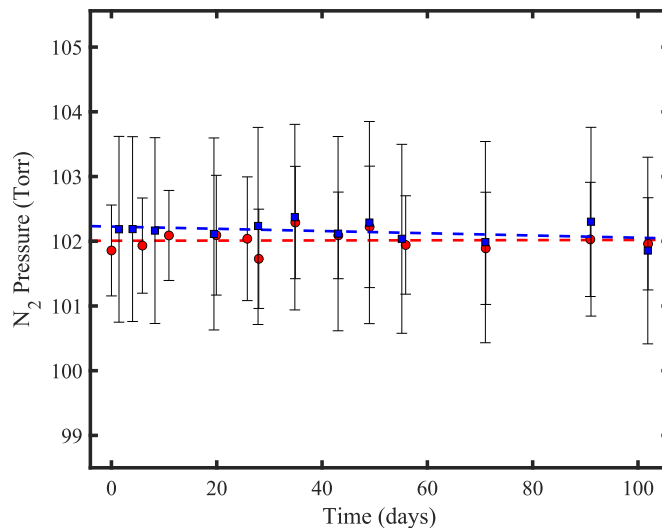


Figure 4.13: Inferred buffer gas pressure from the shift Δ_{BG} for a cell kept at 60 °C (blue squares) and another at 120 °C (red circles).

In the future we look to further investigate any potential depletion of N_2 pressure induced by the NEG by implementing a pressure tuned cell into a vapour cell based atomic clock. These atomic clocks have recently been used to monitor changes in residual gas pressure at the mTorr level over the period of a few days [76].

4.6 Nitrogen Evacuated Cell

Finally, to demonstrate the potential range of the pressure tuning technique we investigated removing as much of the N_2 content within the cell as possible with the goal of realising a vapour cell with a low residual gas pressure. Micro-fabricated vapour cells within this pressure range have found use as compact atomic wavelength references for laser stabilisation [77]. Additionally, by totally depleting the

N₂ content within the cell it is then possible to evaluate the presence of residual non-getterable gases within the cell, which have been released during alkali dispensing and NEG activation.

A separate cell derived from the same wafer as discussed in section.4.1 was implemented into the absorption spectroscopy setup and activated with 3 W of incident power with an activation duration of several minutes. This activation process was repeated until no change in N₂ pressure was registered.

An alternative approach to estimate pressure broadening in lower pressure cells is to employ saturation absorption spectroscopy, which provides a spectroscopic feature much closer to the natural width of the atomic transition such that the effects of pressure broadening are more prominent than in the Doppler broadened absorption spectra [78–80]. However, a sub-Doppler resonance provided by saturation absorption spectroscopy will experience a power broadening of the form [79],

$$\Gamma = \Gamma_0 \sqrt{1 + I/I_{\text{sat}}} \quad (4.16)$$

where Γ_0 represents the zero intensity linewidth, which includes contributions from the natural linewidth and broadening mechanisms such as pressure broadening, laser linewidth, transit-time, etc. I_{sat} is the saturation intensity of the addressed transition, and I is the intensity of the pump beam. To account for the effects of power broadening the linewidth of the sub-Doppler feature has to be measured at a range of intensities and then by extrapolating back to a zero-intensity linewidth an estimation can be made on the level of pressure broadening.

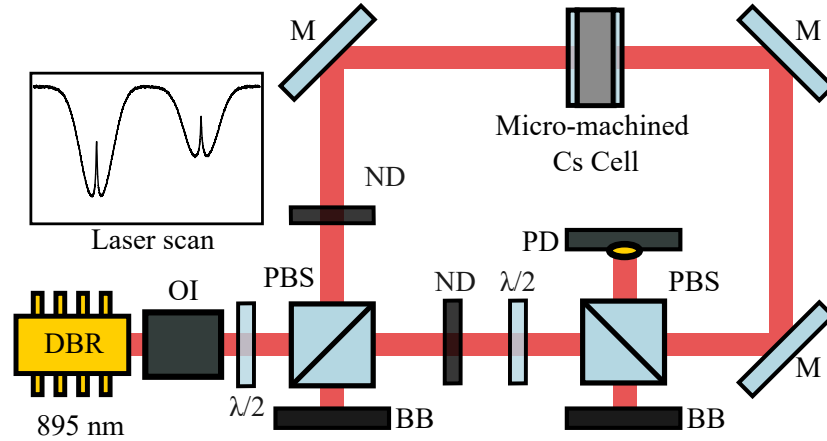


Figure 4.14: Saturation absorption spectroscopy setup for determination of residual broadening within a low pressure vapour cell. DBR:Distributed Bragg Reflector. OI:Optical Isolator. $\lambda/2$:Half Waveplate. PBS:Polarising Beam Splitter. BB:Beam Block. PD:Photodiode. M:Mirror. ND:Neutral Density Filter.

The spectroscopic setup was modified to allow for saturation absorption spectroscopy to be performed as illustrated in Fig.4.14. The light from the DBR was collimated to a beam waist of $\omega_0=0.9$ mm ($1/e^2$ radius) and split into independent pump and probe beams with a $\lambda/2$ wave-plate and a PBS. This configuration was chosen over the simpler retro-reflecting configuration discussed in section.2.3 to allow for the pump intensity to be varied without influencing the probe intensity. The light transmitted(reflected) by the PBS was used as the pump(probe) beam. The pump beam passed through another combination of a $\lambda/2$ wave-plate and PBS, which was used in conjunction with neutral density filters to adjust the intensity of the pump beam. The light was then aligned through the cell and terminated on a beam block. The probe beam was attenuated with ND filters to an average intensity of 0.1 mW/cm². This probe power was selected as it provided the best trade off between having a sufficient SNR for fitting whilst still maintaining a weak probe beam to prevent a significant systematic contribution to the sub-Doppler linewidth. The probe beam was then aligned through the cell and detected on a photodiode and recorded on an oscilloscope. The pump and probe beams were aligned to be overlapped within the cell with an estimated

angle between the two beams of < 10 mrad.

To increase the number of data points taken across the sub-Doppler features the laser frequency scan was reduced to ≈ 3 GHz centred between the $F=4$ to $F'=3$ and $F=4$ to $F'=4$ hyperfine transitions as shown in Fig.4.14. Due to the reduced scan range the etalon previously discussed in section.4.2 could not be employed to linearise the frequency scan; therefore, over this range the scan was assumed to be linear. The peaks of the two sub-Doppler features were used as frequency references to calibrate the frequency scan with respect to the $F=4$ to $F'=3$ transition. From this calibration the frequency scaling error was estimated to be <1 MHz across the 1.1 GHz between the two transitions. During analysis only the width of the $F=4$ to $F'=3$ transition was considered. To extract the linewidth of the sub-Doppler feature the spectroscopic signal was truncated to $\approx \pm 40$ MHz around the sub-Doppler resonance. The sub-Doppler feature was then fit with a Lorentzian line shape with a typical spectra and fit shown in Fig. 4.15 (a)-(b) for an average pump intensity of 1.2 mW/cm^2 . For each pump intensity 10 traces were recorded and the average linewidth was taken.

The extracted sub-Doppler linewidths were fit with a function of the form of Eq.4.16 to extrapolate back to a zero-intensity linewidth where both Γ_0 and I_{sat} were left as free parameters within the fit. A zero-intensity linewidth of $\Gamma_0/2\pi = 8.4 \pm 0.5$ MHz and saturation intensity of $I_{\text{sat}} = 2.4 \pm 0.4 \text{ mW/cm}^2$ was obtained as demonstrated in Fig. 4.15 (c). While the saturation intensity was found to be in good agreement with the expected value of $I_{\text{sat}} = 2.5 \text{ mW/cm}^2$ the linewidth is significantly larger than the natural width of this transition ($\Gamma_{\text{nat}}/2\pi = 4.5$ MHz). This could be due to a number of systematic broadening mechanisms such as residual Doppler broadening, laser linewidth, transit-time broadening, etc.

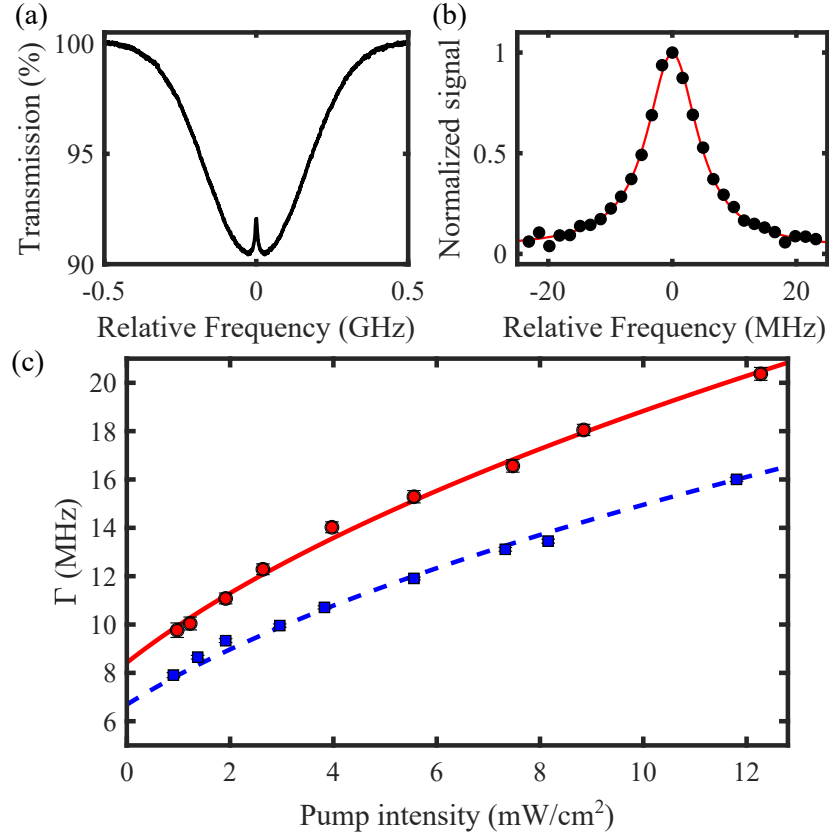


Figure 4.15: (a): Sub-Doppler spectroscopy of the $F = 4 \rightarrow F' = 3$ transition (single-shot) with pump intensity $1.2 \text{ mW}/\text{cm}^2$ and vapour cell at room temperature. The Doppler broadened absorption provides a FWHM of $\sim 400 \text{ MHz}$, with a sub-Doppler linewidth of $\sim 10 \text{ MHz}$. (b): Spectra (black circles) and Lorentzian fit (red line) of the sub-Doppler resonance extracted from (a). (c): The sub-Doppler linewidth as a function of pump intensity for the micro-fabricated cell (red circles) and glass-blown cell (blue squares) with fit lines of the form $\Gamma = \Gamma_0 \sqrt{1 + I/I_{\text{sat}}}$ shown in solid red and dashed blue lines respectively.

To try and account for these systematic broadening mechanisms the measurements were repeated within the same setup with a 7-cm long glass-blown reference vapour cell, which yielded a zero-intensity linewidth of $\Gamma_0/2\pi = 7.0 \pm 0.4 \text{ MHz}$ and saturation intensity of $I_{\text{sat}} = 3.0 \pm 0.5 \text{ mW}/\text{cm}^2$. By comparing the zero-intensity linewidths a residual broadening of $\approx 1.4 \pm 0.6 \text{ MHz}$, was obtained for the depleted micro-fabricated vapour cell. Further activation of the NEG material was subse-

quently performed; however, this was found to have no noticeable effect on the residual broadening within the cell. If we attribute this discrepancy to pressure broadening arising from the remaining N_2 within the cell, this would place an upper bound on the N_2 pressure of 100 mTorr at 21°C. However, the observed residual pressure broadening is likely arising due to a combination of gas-species, which were introduced into the cell during dispenser pill activation making estimating an exact pressure difficult.

A recent publication by Klinger *et al.* used an alternative version of the power broadening equation, which takes the form,

$$\Gamma = \Gamma_{\text{nat}} \sqrt{1 + I/I_{\text{sat}}} + \Gamma_{\text{R}} \quad (4.17)$$

where Γ_{R} is the additional broadening arising due to the spectroscopic broadening mechanisms mentioned previously. By fitting the extracted linewidths for the micro-fabricated cell and glass-blown cell with Eq.4.17 and comparing the results we obtain a similar level of residual broadening within the micro-fabricated cell of 1.0 ± 0.6 MHz.

In the future to better estimate the residual pressure broadening we will investigate alternative spectroscopic techniques, which provide narrower features such as two-photon spectroscopy, [81, 82] which has been used to resolve residual pressure broadening in a micro-fabricated cell at the level of ≈ 100 's kHz [81].

4.7 Conclusion

This chapter introduced a simple approach to buffer gas pressure tuning in micro-machined vapour cells. This approach greatly simplifies current methods for in-situ tuning of the cell pressure ratio with a minimal footprint on the cell dimensions. The demonstrated tunability and expected longevity from this technique could prove advantageous to the fabrication of buffer gas-based atomic sensors, such as clocks and optically pumped magnetometers, where such a method could be used for real-time fine-tuning of the sensor sensitivity [55]. Additionally, this

approach could greatly reduce manufacturing costs by enabling an array of cell target pressures to be extracted from a single wafer with a back-filled buffer gas pressure.

Chapter 5

Compact Zeeman Tunable Wavelength Reference

A key component in cold-atom based atomic devices, such as atom interferometers [2, 83] and cold-atom atomic clocks [84–88], is the laser system employed in the cooling and trapping of neutral atoms. These cold-atom experiments typically begin with the formation of a magneto-optical trap (MOT), which is employed to both cool and trap atoms (more details in Chapter 6). The laser employed for trapping is required to be frequency stabilised with frequency deviations < 1 MHz [89], whilst being red-detuned from the cycling transition by $\Delta = -\Gamma \rightarrow -2\Gamma$ [40], where Γ is the natural linewidth of the transition with larger detunings required to cool the atoms to down to the μK level. Trapping and cooling 10^6 to 10^7 ^{87}Rb atoms for cold atom based atomic clocks requires ≈ 30 mW of optical power [40].

Laser systems for laser cooling typically consist of an atomic reference used to stabilise the laser frequency and an acoustic optical modulator (AOM), which can be used to provide intensity control, frequency offsets and frequency sweeps all of which are key for the production of cold atoms [90]. However, the inclusion of an AOM can significantly increase both the complexity and size of the laser system with the need for additional optics and RF components. To facilitate the miniaturisation of laser systems for cold-atom applications, we explore a compact Zeeman tunable wavelength reference [91–95] that enables laser frequency tuning

and stabilisation in a micro-fabricated vapour cell, sandwiched between a printed-circuit-board (PCB) coil pair. The detuning range and stability of this package are evaluated as a potential replacement for an AOM for frequency control in compact atomic devices.

5.1 Atomic Wavelength Referencing

Before discussing the Zeeman tuning technique we will first give a brief description of an atomic wavelength reference. Here, we focus on the frequency modulation technique, which has a simple and compact implementation, making it well-suited for miniaturisation [96]. This method involves stabilising a laser's frequency to an atomic transition, typically a sub-Doppler feature provided by saturation absorption spectroscopy as illustrated in Fig.5.1.

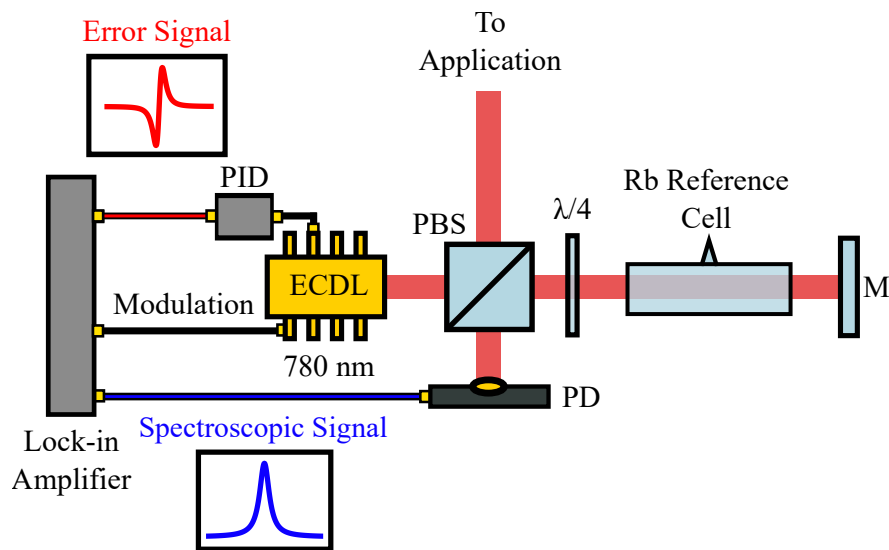


Figure 5.1: A simple rubidium wavelength reference setup using the frequency modulation technique. ECDL:external cavity diode laser, PBS:polarising beam splitter. M:mirror. PD:photodiode.

This technique entails frequency modulating the laser light. This can be achieved in a variety of ways, for example either via an external modulator such as an electro-optic modulator (EOM) or via direct modulation of the laser diode current. As the laser's frequency is scanned over the atomic resonance, the

frequency modulation is translated to amplitude modulation, which alters the detected spectroscopic signal. Subsequently a component emerges at the modulation frequency, which is proportional to the derivative of the spectroscopic signal [97]. Synchronous demodulation and low-pass filtering can then be employed to extract the derivative signal. This is typically achieved by utilising either a lock-in amplifier [97] or a field programmable gate array (FPGA) [98]. The resulting derivative signal has a zero-crossing slope where zero corresponds to the centre of the atomic resonance. This signal can then be fed into a PID controller where its zero-crossing slope can be used as an error signal to feed back on the laser frequency to keep it on resonance.

5.2 Zeeman Tunable lock

The Zeeman tuning technique employs circularly polarised light to probe magnetically sensitive atomic transitions. The Zeeman effect allows for the frequency of these transitions to be tuned thereby shifting the error signal used to stabilise the laser. This method can be employed to controllably shift the laser frequency while avoiding the optical losses typical of an AOM setup [99]. For the case of a weak magnetic field, transitions between m_F levels will experience a linear frequency shift of the form:

$$\Delta\omega_{F,m_F} = \frac{1}{\hbar}\mu_B B_z (g_{F'} m_{F'} - g_F m_F) \quad (5.1)$$

We look to exploit this effect to achieve the red detuning required to form a MOT whilst stabilising the lasers frequency directly to the cycling transition. Here we focus on ^{87}Rb as it is commonly used in cold atom experiments within our research group. For ^{87}Rb the D_2 $F=2$ to $F'=3$ cycling transition is typically employed for cooling. For this transition the ground ($F=2$) and excited states ($F'=3$) have g_F factors of $g_F = \frac{1}{2}$ and $g_F = \frac{2}{3}$ respectively. Thus the largest frequency shift occurs for transitions between the $F=2$, $m_F=\pm 2$ to $F'=3$, $m_{F'}=\pm 3$ Zeeman sub-levels with a magnetic sensitivity of ≈ 1.4 MHz/G.

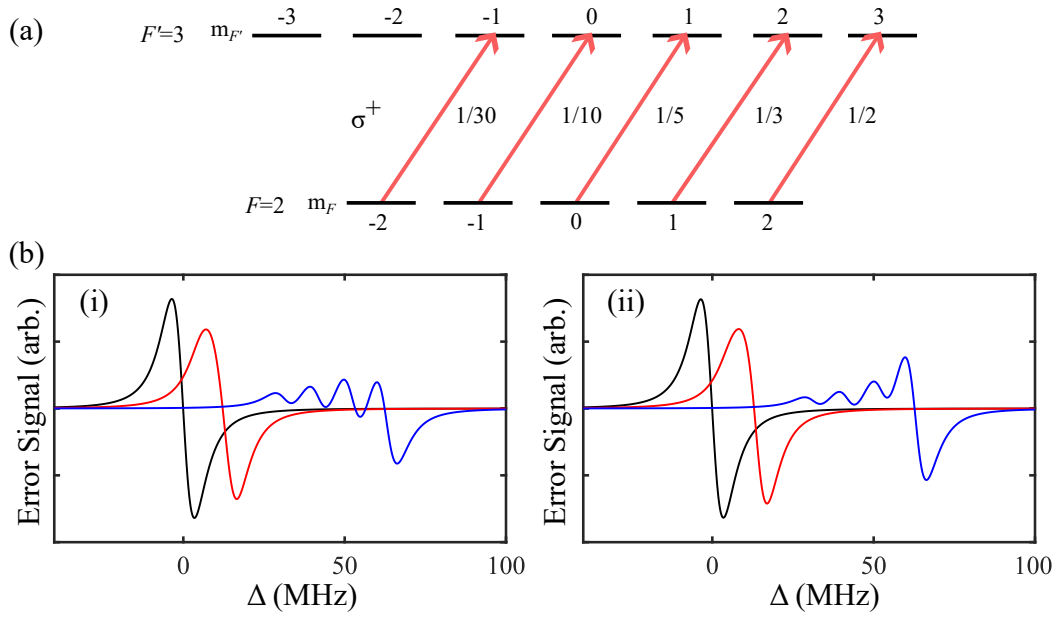


Figure 5.2: (a): An illustration depicting σ^+ transitions between the Zeeman sub-levels of the $F = 2$ to $F' = 3$ hyperfine transition, with their relative transition strengths highlighted. (b): The sum of the error signals produced for each Zeeman transition for an applied magnetic field along the beam propagation axis of 0 G (black), 10 G (red) and 46 G (blue). Accounting for their relative transition strength and magnetic sensitivity. (i): Only accounting for the relative strengths each transition. (ii): Increases the relative strength of the $m_F=2$ to $m_{F'}=3$ transition by a factor of two to account for the effects of optical pumping.

To address these transitions, we can use circularly polarised light with a magnetic field applied along the beam propagation axis. This will drive σ^+ or σ^- transitions depending on the handedness of the light and the direction of the magnetic field. For σ^+ transitions when a resonant photon is absorbed the atom is excited to the $F'=3$ state and the photon transfers its angular momentum to the atom, which leads to $\Delta m_F = +1$ as illustrated in Fig.5.2. For this configuration the $F=2, m_F=2$ to $F'=3, m_{F'}=3$ transition has the largest transition strength however, other weaker transitions are also driven, which have a smaller magnetic sensitivity. As a result of driving these additional transitions at higher magnetic fields distortions in the error signal can arise as the individual Zeeman transitions

become resolvable as shown in Fig.5.2 (b) for a 46 G bias field however, the severity of the distortion in the signal can be reduced due the effect of optical pumping. These additional transitions can reduce the induced frequency shift in the error signal for a given magnetic field with values reported in literature ranging from 1.05 to 1.4 MHz/G [91, 93] with the variation attributed to the different levels of optical pumping achieved in each experimental realisation. Additionally, this technique has demonstrated a frequency tuning range of $\approx \pm 60$ MHz [93] around the atomic transition.

5.3 Physics Package

The compact Zeeman tunable wavelength reference was comprised of saturation absorption spectroscopy through a micro-fabricated vapour cell, as shown at the centre of Fig.5.3 (a). The micro-fabricated vapour cell, shown in Fig. 5.3 (b), was fabricated by the University of Glasgow (UOG) and was composed of a 1 mm thick silicon frame anodically bonded at both interfaces to 0.5 mm thick borosilicate glass wafers, as highlighted in Fig. 5.3 (c). The silicon frame is deep reactive-ion etched using an anisotropic Bosch process [100] to form a two-chamber cell. The first chamber houses a micro-pill based alkali vapour source (SAES Rb/AMAX/Pill1-0.6).

The second chamber acts as the spectroscopy region with a 2 mm diameter aperture. The two chambers were connected via $6 \times 50 \mu\text{m}$ wide, non-line-of-sight channels to prevent glass damage in the spectroscopy region from hot alkali released in the dispensing process. The cell is mechanically diced to dimensions of $10 \text{ mm} \times 10 \text{ mm} \times 2 \text{ mm}$ and a surface-mounted resistor adhered to the side of the silicon frame to heat the cell to a typical operating temperature of 60° C . Prior to the implementation of the spectroscopy cell in the apparatus, the pill source was laser activated. Here, it was found that utilising the activation setup discussed in section.3 with activation conditions of 1 W for 10 s [101] was sufficient to fill the cell with a saturated amount of Rb. The lower required dispensing power com-

pared to the previously discussed 6 mm waterjet cell was attributed to reduced alkali consumption during the vapour cell curing process [102], arising from the smaller surface area of the cell walls.

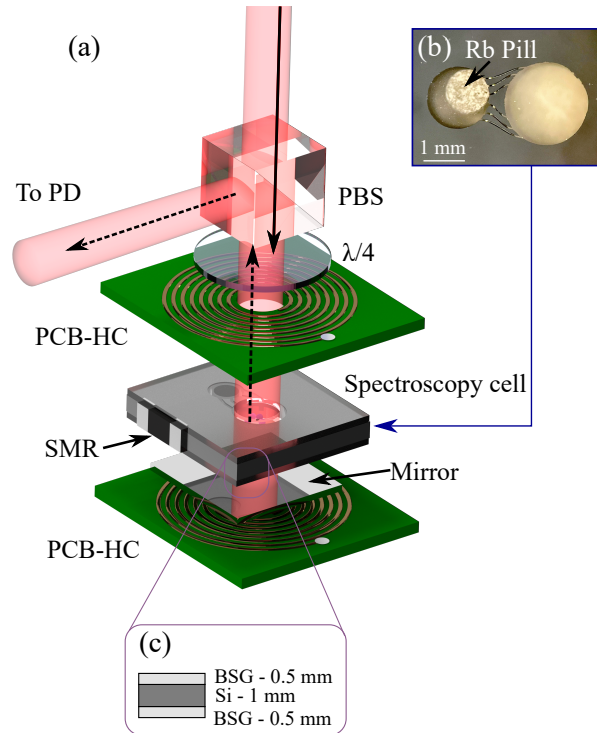


Figure 5.3: (a): A micro-fabricated cell based wavelength reference using saturated absorption spectroscopy. Solid/dashed lines indicates the incident/retro-reflected beam. PD: Photodiode. PCB: Printed-circuit-board coils. PBS: Polarizing beam splitter. SMR: Surface mounted resistor. (b): Microscope image of the micro-fabricated cell in the wavelength reference package. (c): Layer structure for the wavelength reference micro-fabricated cell stack. BSG: Borosilicate glass. Si: Silicon.

The required bias magnetic field for Zeeman tuning was produced by a pair of PCB coils, which sandwiched the micro-fabricated cell. Each 1 mm thick PCB was double-side printed and electrically connected via a circuit through-hole to increase the number of turns over the given board volume. The coil was formed of $35 \mu\text{m}$ thick copper layer wires with $170 \mu\text{m}$ width deposited on the surfaces of the board to form a spiral pattern with a total of 14 turns, with a mean radius

of 3.3 mm ($R_{min} = 2.2$ mm, $R_{max} = 4.5$ mm). The PCB coils were designed by J. McGilligan utilising a numerical solution to the Biot-Savart law [90] with the resulting field shown in Fig.5.4. When designing/modelling the coils the effects of the spiral pattern were ignored and the magnetic field generated by the coils was modelled assuming two coils with 14 turns and a radius of 3.3 mm separated by 3.3 mm to fulfill the Helmholtz configuration. From this model, we can estimate the strength of the field within the cell, which can be used in conjunction with the expected shift of 1.4 MHz/G to determine a frequency tuning rate of 25.4 MHz/A. The centre of the coil had a 1.5 mm radius aperture that was aligned with the spectroscopy chamber for optical interrogation of the cell. The coils and cell were held firmly in location within a 3D printed mount, formed from high temperature plastic that ensured robust alignment through a press-fit and were further secured with epoxy.

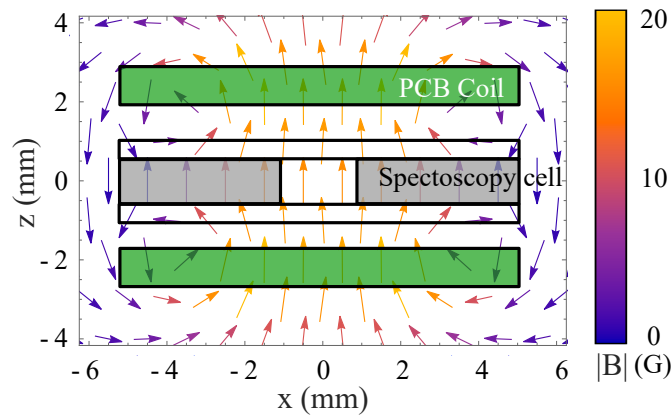


Figure 5.4: Simulated magnetic field for the offset lock PCB Helmholtz coils carrying 1 A.

The 3D printed mount containing the vapour cell and PCB coils was then implemented into an optical setup similar to that depicted in Fig.5.1. Light from a home-built external cavity diode laser [48] (ECDL-1) was transmitted through a PBS, circularly polarized with a $\lambda/4$ wave-plate before the vapour cell. The light then passes through the cell with an incident power of $300 \mu W$ and $1/e^2$ beam radius of 1.5 mm. The light transmitted through the cell was retro-reflected by a dielectric reflector, behind the micro-fabricated cell. The

output transmission from the spectroscopy system passed back through the $\lambda/4$ wave-plate, ensuring that the light was reflected by the PBS to a photodiode for detection. The laser was scanned across the ^{87}Rb $F = 2$ D_2 hyperfine transitions and frequency modulated at 250 kHz via current dithering, provided by the laser controller (MOGLABS DLC), with a modulation depth < 1 MHz. The signal from the photodiode was passed back to the laser controller, which had an integrated demodulation circuit and PID controller. The resulting error signal was then used to electronically feed-back to ECDL-1 for frequency stabilisation. The resulting saturation absorption and error signals are shown in Fig.5.5. The sub-Doppler features are broadened due to the presence of residual gases within the vapour cell, which were released during alkali dispensing. The level of residual gas could be reduced by activating the NEG material within the pill as discussed in Chapter 4 however, within these 1 mm vapour cells this was found to release an excess of Rb, which would condense within the spectroscopy chamber blocking optical access.

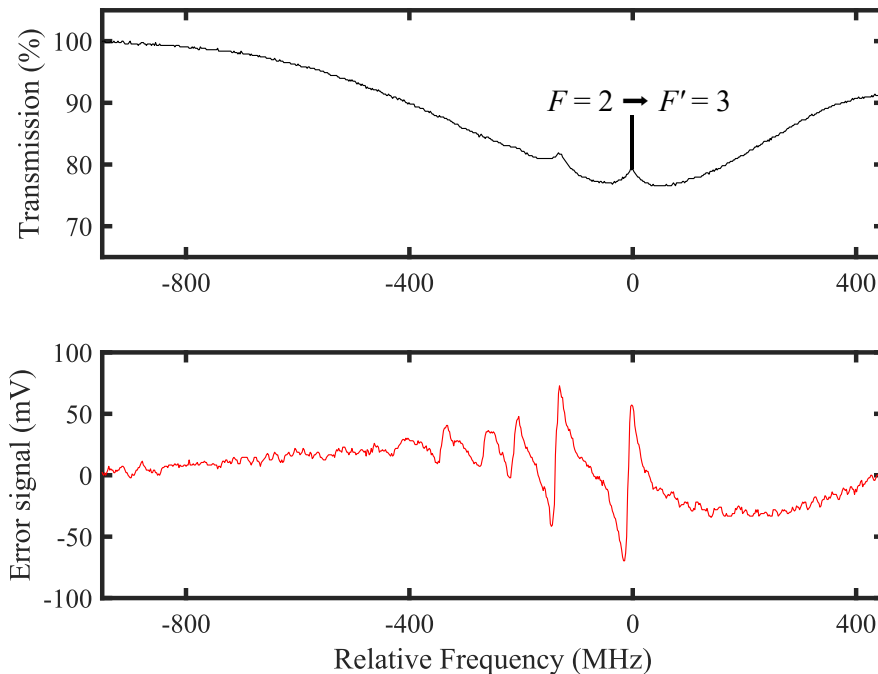


Figure 5.5: Saturation absorption spectroscopy (black) and error signal (red) from the compact package with PCB coils turned off and the vapour cell heated to 60 °C.

5.4 Frequency Tuning

Once the compact wavelength reference was assembled, the next step was to assess the frequency tuning range provided by the PCB coils. This was achieved by stabilising ECDL-1 to the $F = 2 \rightarrow F' = 3$ transition in ^{87}Rb and measuring a beat note against a second ECDL (ECDL-2), which was stabilised to the $F = 2 \rightarrow F' = 2, 3$ cross-over transition in ^{87}Rb using saturation absorption spectroscopy on a separate 7 cm long reference cell with the same experimental parameters as used with ECDL-1. The beat note signal was obtained by aligning ≈ 1 mW of light from each stabilised laser onto a fast photodiode. When the two beams are well overlapped with the same polarisation, a beat frequency at the difference in frequency between ECDL-1 and ECDL-2 can be observed at ≈ 130 MHz (the frequency separation of the two sub-Doppler resonances). The beat frequency was then measured on a frequency counter as illustrated in Fig.5.6.

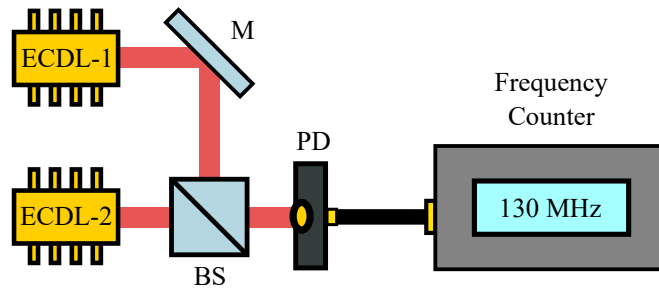


Figure 5.6: Beat note measurement setup. ECDL:External Cavity Diode Laser, M:Mirror, BS: Beam Splitter and PD:Photodiode.

The beat note frequency was then measured for a range of coil currents. For each coil current the beat frequency was tracked for a period of 5 s with a gate time of 1 ms with typical frequency deviations of ≈ 100 kHz arising due to frequency instability of the locked lasers. From these measurements the induced frequency shift from the coils was found to be 25.5 ± 0.3 MHz/A as, shown in Fig. 5.7(a) consistent with the value calculated from the coil parameters of 25.4 MHz/A. Additionally, the frequency offset was observed to be tunable over ± 60 MHz, a range similar to other implementations of this technique that employ more robust coil assemblies [93, 94], suggesting that the magnetic field generated by the PCB

coils does not impose a limitation on performance.

For larger frequency offsets we observe a discrepancy between the expected and observed shift, attributed to distortions in the error signal, which arise at higher magnetic fields, as the individual transitions between m_F levels become resolvable. The error signal from the micro-fabricated cell, shown for $\Delta/2\pi = -12$ MHz in Fig. 5.7 (b) with a red line, has no significant amplitude or linewidth degradation compared to the resonant signal, shown in black. However, for stronger magnetic fields, a distortion becomes apparent as can be seen with the blue line at a detuning of $\Delta/2\pi = -66$ MHz. The frequency offset range is thought to be limited due this distortion, which produces additional zero-crossing slopes with the opposite phase, which when fed into the PID loop would result in the laser unlocking.

The demonstrated frequency offset range is sufficient to achieve a red-detuned lock for a magneto-optical trap [103], where the trapped atom number is typically optimum in Rb for a detuning between $\Delta = -\Gamma_{D_2} \rightarrow -2\Gamma_{D_2}$, where $\Gamma_{D_2}/2\pi = 6.1$ MHz [24]. Over this range the PCB coil pair require < 0.7 W of electrical power as shown in Fig.5.7(c). Frequency offsets > 20 MHz cannot be employed continuously due to the excess heat produced by the coils. Over time, this heat increases the Rb vapour density within the cell to the point where no light is transmitted through the cell. Consequently, no light reaches the photodiode, resulting in no error signal being produced, which ultimately leads to the laser becoming unlocked. Thus, larger detunings can only be employed for short time intervals. However, this is unlikely to be an issue as larger detuning are typically only required for an additional cooling stage known as optical molasses where the frequency is swept up to 50 MHz [104] over a period of several milliseconds. While this heating effect is detrimental to achieving continuous operation at larger detunings, it could potentially be exploited in future iterations of the compact Zeeman tunable package as a means of heating the cell, thereby circumventing the need for an independent heater.

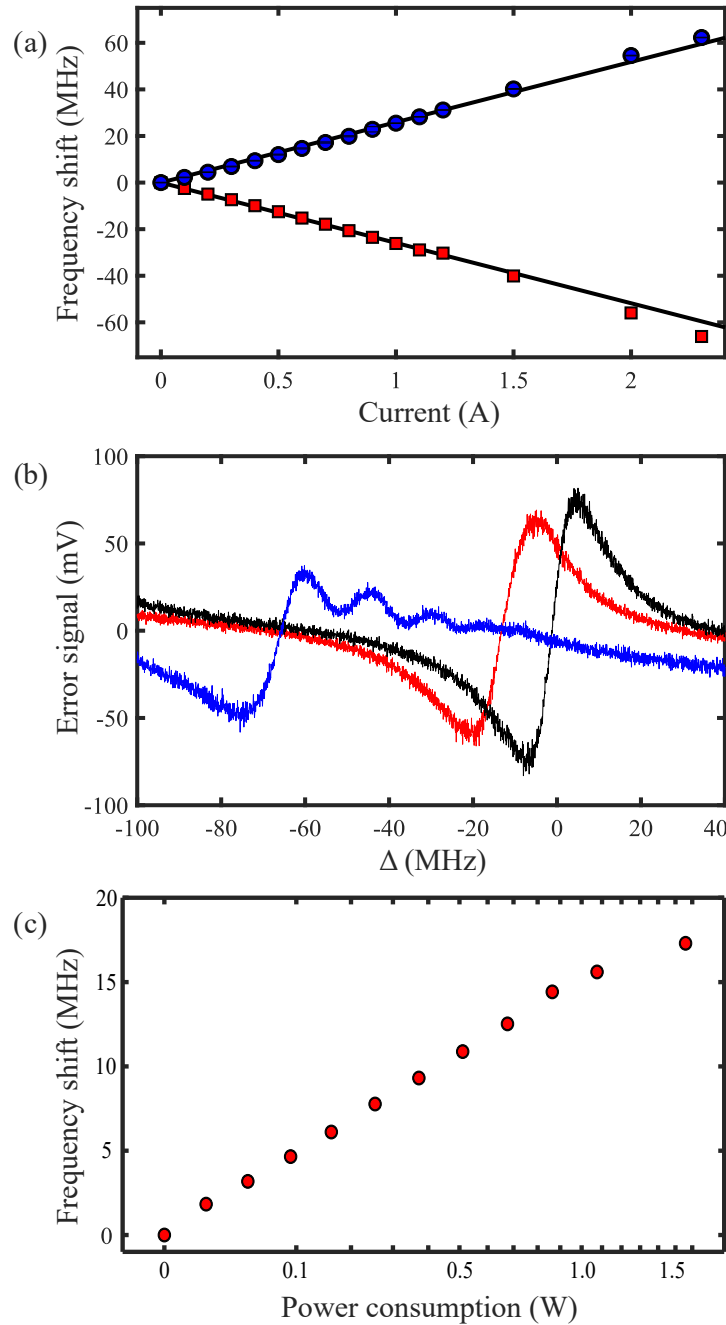


Figure 5.7: (a): Measured frequency shift as a function of the coil current, where blue circles/red squares represent a positive/negative applied current. The black lines highlight the expected shift as calculated from the coil parameters. (b): The Zeeman shifted error signal measured with a single shot on resonance (black), at -12 MHz detuning (red) and at -66 MHz detuning (blue). (c): Measured frequency shift as a function of the power drawn by the PCB coils with the x axis scaled in the square root of the power.

5.5 Frequency Stability

The next step after demonstrating the frequency tuning range was to determine the frequency stability achievable with the compact Zeeman tunable package. For this study the PCB coils were used to red detune ECDL-1 by $\Delta/2\pi = -15$ MHz from the $F=2$ to $F'=3$ transition, which was selected as a typical detuning to form a MOT. The stability was assessed by tracking the beat note frequency over a period of 10 minutes as demonstrated in Fig.5.8 (a). For this measurement the gate time was set to 10 ms.

The Allan variance is the recommended measure of frequency stability of an oscillator by the IEEE [105] therefore, it is what will be used here to assess stability. It is common to express the Allan variance in terms of fractional frequency, requiring that the recorded frequency data be translated into a dimensionless fractional frequency array $y(t)$ using the equation,

$$y(t) = \frac{\nu_{\text{beat}}(t) - \overline{\nu_{\text{beat}}}}{\nu_{\text{carrier}}}, \quad (5.2)$$

where ν_{beat} is the recorded beat frequency and ν_{carrier} is the frequency of the stabilised laser ≈ 380 THz. The Allan variance is defined as:

$$\sigma^2(\tau) = \frac{1}{2(M-1)} \sum_{i=1}^{M-1} (\bar{y}_{i+1}(\tau) - \bar{y}_i(\tau))^2, \quad (5.3)$$

where $\bar{y}_i(\tau)$ is the mean frequency over an averaging window τ and M is the number of recorded data points.

The Allan variance does not fully utilise the available data set and thus has largely been superseded by the overlapping Allan variance, which uses the available data set more effectively improving the confidence bounds in the extracted stability. This method employs overlapping averaging windows to ensure that all data separated by $\tau = n\tau_0$ is used, where n is a factor, which represents the length of the averaging window and τ_0 the sample time, i.e. the gate time. The overlapping Allan variance can be defined as:

$$\sigma^2(\tau) = \frac{1}{2n^2(M-2n+1)} \sum_{j=1}^{(M-2n+1)} \sum_{i=j}^{(J+n-1)} (\bar{y}_{i+n}(\tau) - \bar{y}_i(\tau))^2 \quad (5.4)$$

The resulting overlapping Allan deviation $\sigma(\tau)$, is shown in Fig.5.8 (b).

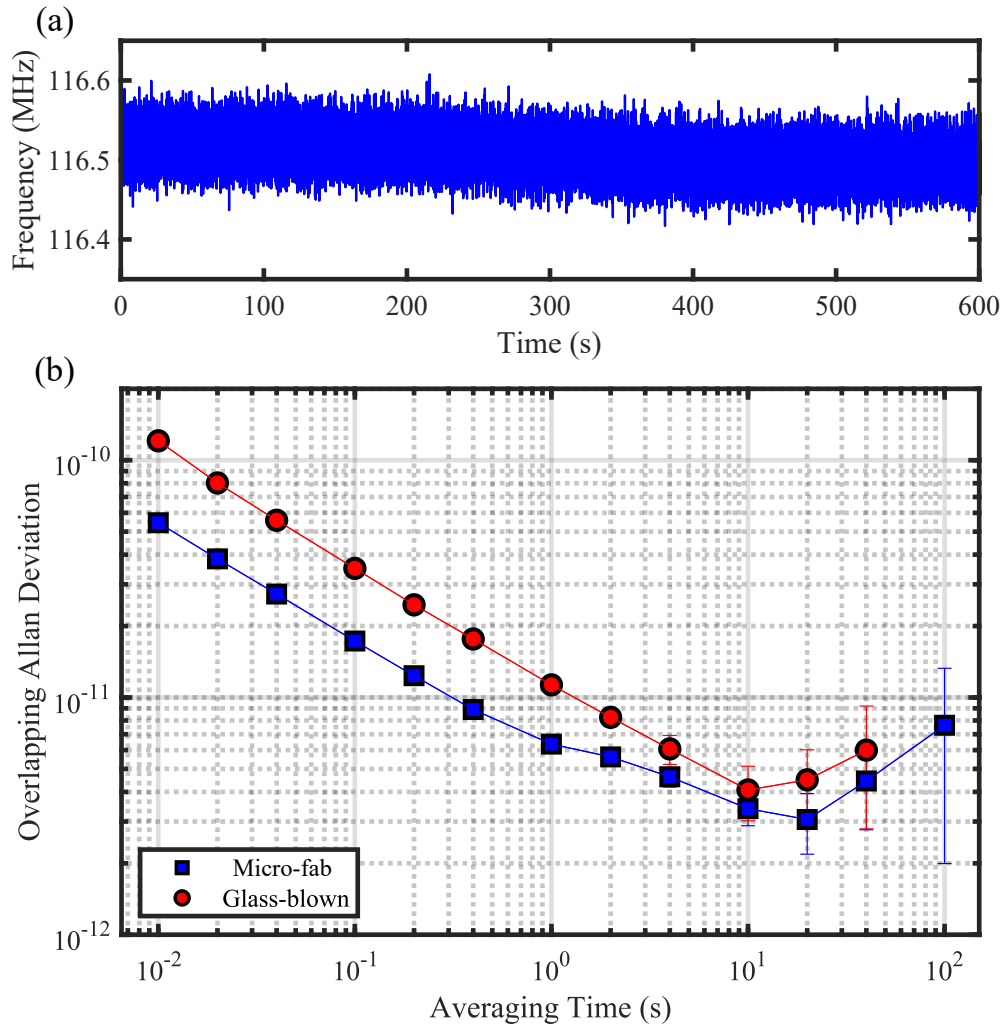


Figure 5.8: (a): Beat note frequency recorded by the frequency counter when ECDL-1 is stabilised to the tunable wavelength reference at 60 °C with a 15 MHz red detuning. (b): Overlapping Allan Deviation of the beat note when ECDL-1 is stabilised to the tunable wavelength and a 7 cm room-temperature reference cell, shown in blue squares and red circles respectively.

The slope of the overlapping Allan deviation provides insight into the noise sources limiting the oscillator's stability across different timescales. For averaging times up to 10 s, the wavelength reference package integrates down with a slope of $1/\sqrt{\tau}$. In such cases, the oscillator's stability is primarily limited by the SNR

of the error signal and can be approximated with:

$$\sigma(\tau) \approx \frac{\Delta\nu}{\nu_{\text{carrier}}} \frac{1}{\text{SNR} \sqrt{\tau}}. \quad (5.5)$$

Where $\Delta\nu$ is linewidth of the atomic feature used for stabilisation. Beyond 10 s the frequency of the wavelength reference begins to drift. To determine if the drift was related to the Zeeman tunable package, the stability measurement was repeated with ECDL-1 stabilised to a 7 cm room-temperature reference cell, which demonstrated a similar drift. This drift is likely due to a combination of factors including intensity and fluctuations in room temperature, which can impart shifts in the atomic transition [47,96]. However, these fluctuations can be suppressed by implementing servo loops [47]. It is worth mentioning that the Allan deviation's error bars increase with averaging time due to the reduced number of data points available.

We determine that the physics package was able to reach a stability of $\approx 5 \times 10^{-12}$ at 1 s, which is a comparable level of performance to other wavelength references based on the D₂ line of Rb [47, 106–108]. To confirm that the Zeeman tuning technique had no adverse effect on the attainable stability. We repeated the stability measurements for a range of offset frequencies as shown in Fig.5.9. Here we can observe that over this range of frequency offsets the change in stability is negligible indicating that any distortions in the error signal induced by the bias field has a negligible effect on the linewidth of the sub-Doppler feature $\Delta\nu$.

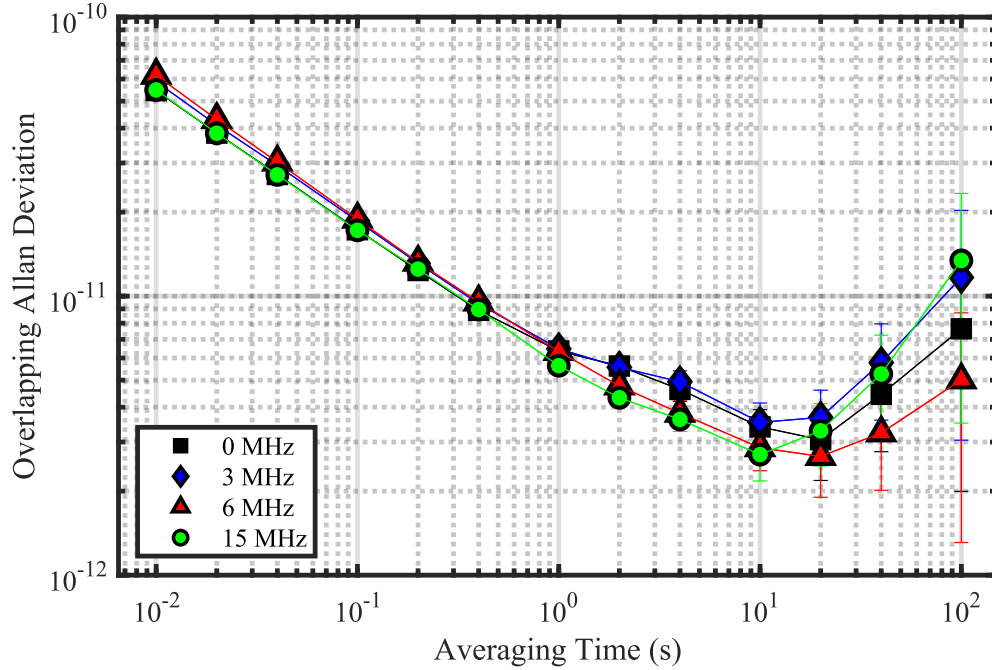


Figure 5.9: Overlapping Allan deviation of the beat note frequency for a range of red detunings. black squares: 0 MHz, blue diamond: 3 MHz, red triangle: 6 MHz and green circle: 15 MHz.

Finally, the stability of the Zeeman tunable package was systematically monitored for various cell temperatures as shown in Fig.5.10(a) to determine an optimal operating temperature. These measurements were taken with no offset applied from the PCB coils. It was observed that with increasing cell temperature, the short-term stability ($\tau \leq 10$ s) of the wavelength reference also increased. This phenomenon is attributed to the increased alkali density at higher cell temperatures, resulting in more atoms contributing to the sub-Doppler signal. This is evident from the increase in amplitude of the sub-Doppler resonance, as observed in Fig.5.10(b), thereby improving the SNR and subsequently the stability. However, it is noteworthy that above ≈ 70 °C there is no longer an increase in the amplitude of the sub-Doppler resonance with temperature. This is attributed to the attenuation of the interrogating beam at higher vapour densities. This effect is reflected in the observed stability with no discernible benefit to operating the cell above ≈ 70 °C. Nevertheless, it is worth highlighting that across all demonstrated operating temperatures, the wavelength reference consistently delivers a

stability sufficient for laser cooling applications of $\approx 10^{-10}$ [109].

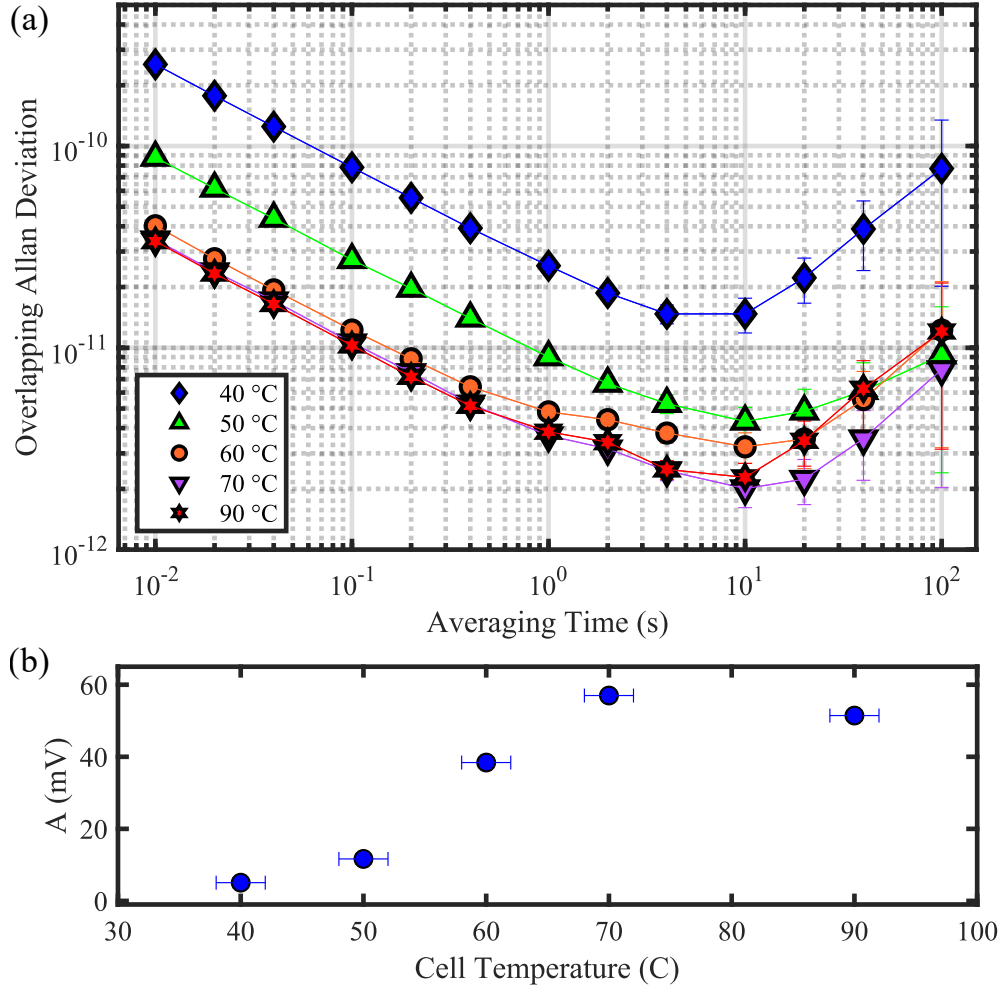


Figure 5.10: (a): Overlapping Allan deviation of the beat note frequency for a range of temperatures: 40 °C blue diamonds, 50 °C green triangles, 60 °C orange circles, 70 °C purple inverted triangles and 90 °C red hexagams. (b): Amplitude of the Sub-Doppler feature as a function of cell temperature.

5.6 Conclusion and Future Work

We have demonstrated a compact Zeeman tunable wavelength reference package, which uses a simple architecture and mass-producible components. The demonstrated stability is competitive with existing wavelength references based on the D_2 line of ^{87}Rb and the frequency offset range is sufficient for the generation of cold atoms. In chapter 6 we will discuss the implementation of this compact

wavelength reference package into a cold atom system.

Although the Zeeman tunable package presented here represents a step towards a compact laser system for the generation of cold atoms, it cannot fully replace the role of an AOM. As an AOM allows for the control of the cooling light's intensity, which allows for a more effective laser cooling sequence [90, 110] resulting in a colder cloud of atoms. Thus to fully replace an AOM future studies are required to realise an alternative method of controlling the laser intensity within a compact physics package.

Chapter 6

Chip-scale Cold Atom Platform

Since the initial demonstrations of laser cooling of ions in 1978 [111] and neutral atoms in 1982 [112], the technique of laser cooling has been widely adopted by the atomic physics community [84, 113–115]. The reason for this wide adoption is owed to the fact that atoms can be cooled to the order of $1\ \mu\text{K}$ [116]. At such temperatures the atoms will move at a velocity ν of around $1\ \text{cm/s}$, a drastic reduction compared to $\nu = 240\ \text{m/s}$ for room temperature ^{87}Rb atoms. This significant reduction in velocity greatly decreases the relaxation rate of the atoms allowing for coherence times $> 100\ \text{ms}$. Due to the long coherence times achievable with cold atoms, they have found particular use in the field of metrology, with the second being realised by the interrogation of laser cooled Cs atoms [117].

The development of a chip-scale cold atom platform has tantalising prospects for the miniaturisation of next-generation quantum technology [1, 2, 40]. Such a platform could find use in a wide range of applications, including navigation, geological surveying, communication and precision timing [40]. Recent studies have demonstrated cold-atom sensor scalability through the coupling of photonic integrated circuits [118–121], meta-surfaces [122, 123], diffractive optics [90, 103, 124], planar coil systems [125] and micro-fabricated alkali sources [126, 127]. More recently, micro-fabricated vapour cells capable of sustaining ultra-high-vacuum (UHV) have been shown in conjunction with micro-fabricated grating chips as an on-chip platform for cold-atoms [128]. Here we discuss the fabrication and

characterisation of a micro-fabricated vapour cell for the generation of cold atoms, which could be used as a platform for a chip-scale cold atom atomic clock [85].

6.1 Laser Cooling

Here, we provide a brief overview of laser cooling, with more detailed explanations of the underlying mechanisms available in references [116, 129].

6.1.1 Optical Molasses

Laser cooling is the process of removing energy from an atom via the transfer of momentum from a laser beam. When an atom absorbs a photon and is excited into a higher energy state it experiences a recoil with momentum,

$$p = m\vec{v} = \hbar\vec{k}, \quad (6.1)$$

where m is the mass of the atom and \vec{k} is the wave vector of light. When the photon is spontaneously emitted the atom will experience another recoil. However, due to the random nature of the spontaneous emission over many absorption and decay cycles, there is no net change in the momentum of the atom. In the case of an atom traveling along z with an anti-parallel resonant light field the transfer of momentum will decelerate the atom bringing it to a halt and then start to accelerate the atom in the opposite direction. The radiation force exerted by the beam on the atom can be expressed by,

$$F = \frac{dp}{dt} = R_{sc}(I, \Delta)\hbar k, \quad (6.2)$$

where $R_{sc}(I, \Delta)$ is the photon scattering rate for a two-level atom. To make this scattering force useful for cooling atoms we can employ two counter-propagating beams, which are red detuned with respect to an atomic transition. In the case of a thermal ensemble of atoms with a 1D velocity distribution the total radiation pressure experienced by an atom is given by,

$$F = \frac{\hbar k \Gamma}{2} \left(\frac{I/I_{sat}}{1 + I_T/I_{sat} + \left(\frac{2\Delta - 2kv}{\Gamma}\right)^2} - \frac{I/I_{sat}}{1 + I_T/I_{sat} + \left(\frac{2\Delta + 2kv}{\Gamma}\right)^2} \right), \quad (6.3)$$

where I is the intensity of each beam, I_{sat} is the saturation intensity of the transition, I_T is the total intensity incident upon the atoms and Δ is the detuning with respect to the atomic transition. Due to the Doppler effect, a moving atom will experience a stronger force from the beam it propagates towards as shown in Fig.6.1. This viscous dampening force acts to cool the atoms. When expanding this cooling technique to 3D it is referred to as optical molasses due to the viscous force the atoms experience, which can slow down them to extremely low velocities [116].

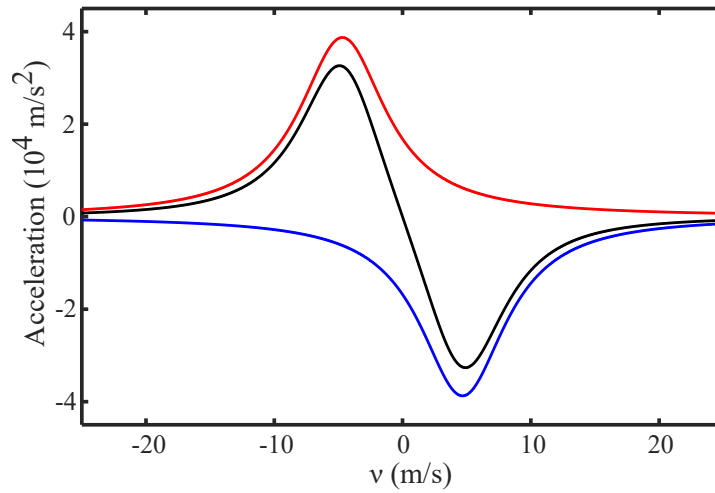


Figure 6.1: Acceleration experienced by ^{87}Rb atoms as a function of velocity. The red and blue lines represent the acceleration from each of the counter-propagating beams with the total acceleration shown in black. For $I=I_{sat}$, $I_T=2I_{sat}$ and $\Delta=-\Gamma$.

The final temperature attainable from this laser cooling mechanism is limited by the spontaneous emission process, which induces a random walk in the atoms that acts as a heating mechanism. The final temperature can be predicted by balancing the cooling and heating rates, leading to the Doppler limit T_D , which is given by [130],

$$T_D = \frac{\hbar\Gamma}{2k_B}. \quad (6.4)$$

For the case of the D_2 line in ^{87}Rb the Doppler limit predicts a temperature of $145 \mu\text{K}$. However, initial experiments in laser cooling Na found that the temperature of the atoms was 6 times lower than the Doppler limit [130]. The issue

here is that so far we have only considers the case of a two-level atom. In reality atoms are comprised of many energy levels. This added complexity gives rise to a sub-Doppler cooling mechanism. In the case of a 1D molasses with two counter-propagating beams with orthogonal polarised linear light, a standing wave will form with a spatially varying polarisation at the scale of the photon wavelength λ . As the atoms move through this changing polarisation they experience a spatially varying potential well induced by the AC stark shift given by,

$$\Delta E = \frac{\Gamma}{8\Delta} \frac{I}{I_{sat}}. \quad (6.5)$$

This configuration allows for an atom moving through the potential wells to translate its kinetic energy to potential energy by climbing to the top of a well. At this stage the atom can then be optical pumped into a ground state with a lower potential energy, resulting in the atom's loss of energy. The minimum achievable temperature with this technique is $T \propto I/\Delta$. However, this cooling mechanism does not allow for cooling to $T=0$ K as it is limited by the heat produced by the recoil induced by the spontaneous emission of a photon. This is known as the recoil limit T_{recoil} given by [129],

$$T_{\text{recoil}} = \frac{\hbar^2 k^2}{2mk_{\text{B}}}, \quad (6.6)$$

where m is the mass of the atom. For ^{87}Rb we determine a recoil limited temperature of $0.36 \mu\text{K}$ with practical demonstrations of this technique routinely reaching temperatures $<10\mu\text{K}$ [90, 116, 131].

6.1.2 Magneto-Optical Traps

Although molasses can be used to cool atoms they are not trapped and are free to diffuse out of the overlap volume of the beams where they are then lost. This diffuse motion is a result of the spontaneous emission process, which causes the atoms undergo a random walk. To trap the atoms we require a spatially dependent force. This can be achieved by combining optical molasses with a magnetic field gradient to form a magneto-optical trap (MOT). Here again we

consider the 1D case for a $F=0$ to $F'=1$ transition, which can be generalised to 3D. The magnetic field gradient for trapping has a zero field centre with a linear gradient on either side. This magnetic field gradient through the Zeeman effect acts to shift the m_F sub-levels as a function of position as illustrated in Fig.6.2. In the case of an ensemble of atoms being interrogated by two counter-propagating red detuned laser beams, which are right-hand circularly polarised. The beams will drive σ^+ transitions if the B field is parallel to the beam and σ^- when anti-parallel. As an atom moves away from the centre the $m_F=-1$ will be Zeeman shifted closer into resonance with the anti-parallel beam, which will exert a force on the atom opposing its motion returning the atom to the centre. This configuration acts to trap the atom within the confines of the beams.

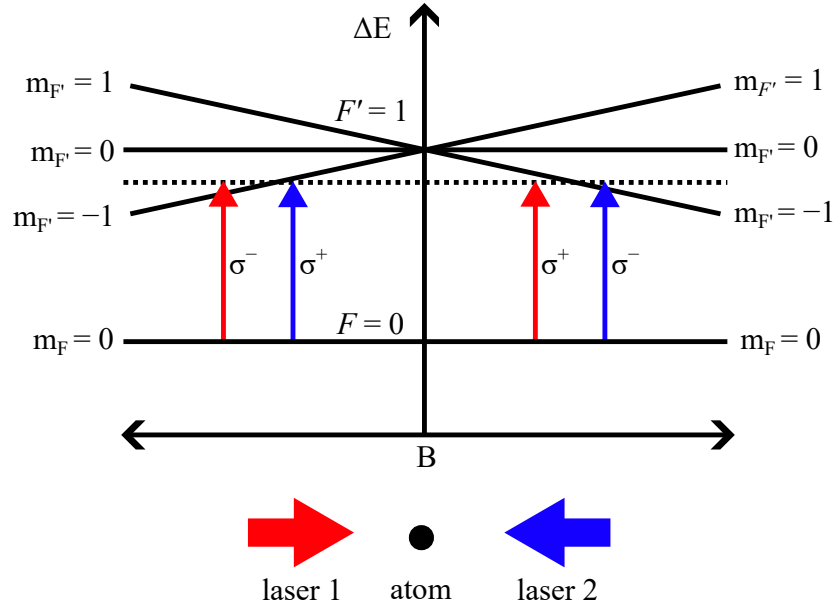


Figure 6.2: Schematic of a 1D MOT for a $F=0$ to $F'=1$ transition with two counter-propagating beams, which are circularly polarised with the same handedness.

For the trapping and cooling of ^{87}Rb the $F=2$ to $F'=3$ cycling transition is driven as the selection rules for the D_2 transition do not allow for decay into the $F=1$ state. However, the nearby $F=2$ to $F'=2$ will also be off-resonantly driven, which over time results in the atomic population accruing in the $F=1$ state and the atoms are lost from the trap. To prevent this from happening a second light

field is required to drive the $F=1$ to $F'=2$ transition, which allows for atoms to decay back into the $F=2$ state. This process is typically referred to as hyperfine re-pumping.

6.1.3 Grating Magneto-Optical Traps

Conventionally, a MOT for trapping and cooling of atoms in 3D is comprised of 6 overlapping beams, with pairs of counter-propagating beams along each Cartesian axis and a set of anti-Helmholtz coils, which create a quadrupole magnetic field. However, the required number of beams for trapping and cooling is $N+1$, where N is the number of dimensions the atom is being cooled in. Thus, 3D cooling can be achieved with only 4 beams. There is a variety of 4 beam MOT configurations with a breakdown of each discussed in [40]. In this work, we employ the grating MOT (GMOT) configuration, which requires only a single incident beam onto a micro-fabricated grating chip. In this work, we use a TRI grating [104], which is comprised of three regions of linear grating orientated at $\frac{2\pi}{3}$ rad with respect to each other. The 1st order diffracted beams produced by these regions form 3 beams, which along with the incident beam, form the 4 required beams in a tetrahedral configuration. A 2D schematic of this configuration is illustrated in Fig.6.3.

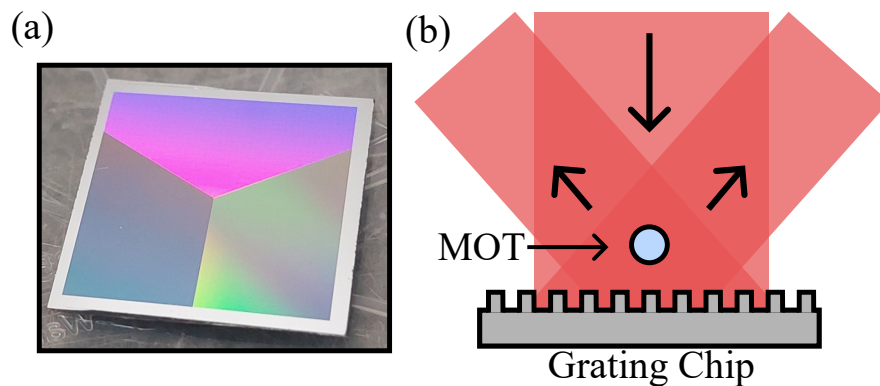


Figure 6.3: (a): A photograph of a TRI grating chip 20 mm x 20 mm. (b): 2D schematic of the GMOT configuration with a MOT forming within the overlap volume of the four beams.

The number of atoms trapped within a MOT is related to the overlap volume of the trapping beams [132], which determines the maximum velocity that can be captured by the trap. In the case of the GMOT the number of trapped atoms has been empirically determined to be proportional to $N \propto V^{1.2}$ [103] where V is the overlap volume of the trapping beams. The GMOT configuration has been well studied within our research group and is discussed in more details within the theses of Vangeleyn [133] and McGilligan [104].

6.2 Micro-fabricated UHV Vapour Cell

Laser cooling requires a vapour cell with a UHV environment, i.e., a vapour cell with a background gas pressure of $<10^{-7}$ Torr [40, 134]. This is because collisions from thermal background gases can eject atoms from the trap, reducing the number of trapped atoms [135]. The micro-fabricated vapour cells discussed throughout this thesis have internal pressures of $\approx 10^{-2}$ Torr, which is orders of magnitude above the required pressure, making them unsuitable for a miniaturised cold atom platform. This background pressure primarily results from contaminants outgassed from the alkali pill source, with an estimated pressure contribution of 10^{-2} Torr, and could be improved by utilizing a cleaner alkali source [136]. However, an additional issue can arise from atmospheric He permeating into the cells through the glass windows, which can raise the cell pressure to 10^{-3} Torr. Once He has permeated inside the vapour cell it cannot be removed with passive pumping techniques such as the non-evaporable getters discussed in Chapter 4 since it is a noble gas. When constructing a vacuum chamber for laser cooling care has to be taken to account for He permeation by either including an active pump, typically an ion pump, which can remove He from the system or by alternatively reducing the rate He can permeate into the cell. This can be achieved by selecting specific glasses with low He permeation rates [134, 135, 137].

Both of these techniques have recently been translated to micro-fabricated vapour cells, with researchers at NIST [128] demonstrating micro-fabricated silicon vapour cells with active pumping provided from an ion pump, which was

capable of sustaining cold-atoms. The micro-fabricated cell was coupled with a micro-fabricated diffractive optic to realise a chip-scale laser cooling platform however, there was an ambiguity in determining the trapped atom number, which arose due to light scattering from the grating surface as well as limited optical access. A subsequent study by Bregazzi *et al.* [138] looked to determine the attainable trapped atom number within a chip-scale cold atom platform with a similar design. In this work a trapped atom number of $\approx 10^5$ atoms was obtained where the trapped atom number was found to be limited by the overlap volume of the trap, which was restricted due to the cells 3 mm thick silicon frame.

Here, we will discuss the fabrication of a next-generation UHV micro-fabricated vapour cell with an increased internal cell thickness of 6 mm. This thicker cell should allow for more atoms to be trapped, as $\approx 93\%$ of the overlap volume will fall within the cell. The fabrication process is illustrated in Fig.6.4. Similar to the other thick micro-fabricated vapour cells discussed in this thesis, the process starts with a 6 mm thick silicon wafer, which is water-jet cut to form the vacuum cavity. After cleaning, the silicon frame was anodically bonded to a 700 μm thick alumina-silicate glass (ASG) wafer (SD-2 HOYA) to form a cell preform using an atmospheric bonding station. An ASG wafer was selected over the BSG used with other cells due to its reduced He permeation rates compared to the conventionally employed BSG [139] whilst still being suitable for anodic bonding to silicon due to its similar CTE.

Next a second ASG glass wafer was mechanically drilled to form a through hole with a diameter of 5 mm. This wafer was then bonded to the upper surface of the cell preform again using an atmospheric bonding station. At this stage a copper stem was placed over the drilled hole and adhered to the cell with vacuum grade epoxy (EPO-TEK 353ND) to form a hermetic seal. This stem was then connected to a small vacuum chamber containing both an ion pump (2 L/s) and Rb dispensers. These Rb dispensers are different from the laser heated dispensers employed in earlier chapters as these dispenser can be restively heated and can be connected to an external power supply via electrical feed-through in the vacuum

chamber. A copper stem was employed, as it could be pinched to isolate the cell from the ion pump, allowing for an assessment of the longevity of a passively pumped micro-fabricated UHV cell. However, this is beyond the scope of the work presented here.

Now, with the micro-fabricated chamber assembled, the next step involved connecting the system to a vacuum pumping station containing both a roughing pump and turbo molecular pump. These pumps were used to reduce the pressure in the chamber to $<10^{-7}$ Torr inferred from the pressure gauge on the pumping station. While still connected to the pumping station, the Rb dispensers were restively heated to remove any contaminants that may have formed on the surface during their fabrication process, which can detrimentally increase the pressure within the UHV cell [140].

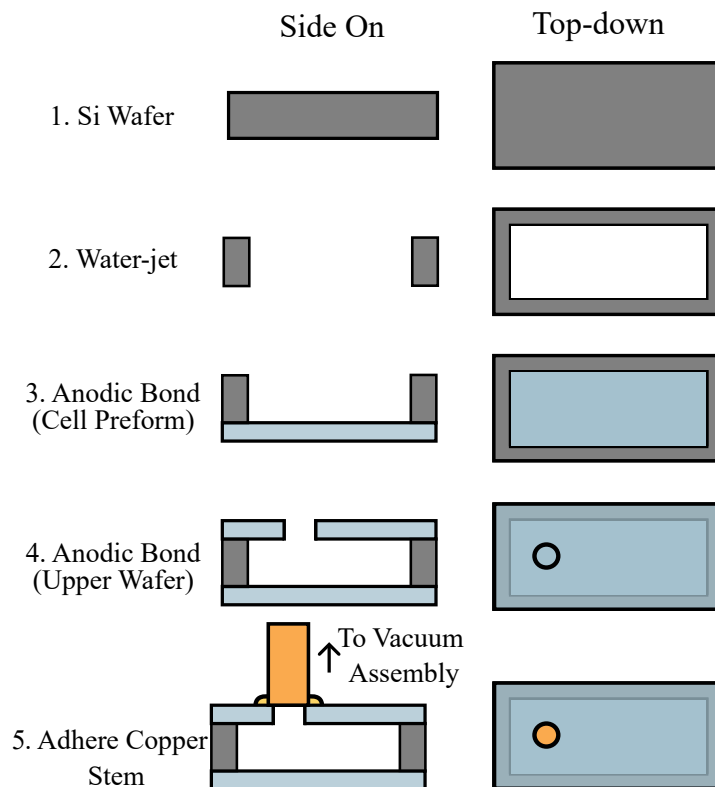


Figure 6.4: Illustration of the UHV micro-fabricated vapour cell fabrication process.

The ion pump was then turned on and the cell was disconnected from the

pumping station. Subsequently, the dispensers were heated continuously for a period of 2 weeks. This was done to coat the internal walls of the cell in a monolayer of Rb [71]. Care was taken during this process to ensure that the chamber pressure did not exceed 10^{-4} Torr, as this could damage the ion pump. After the walls were coated a weak absorption spectra could be observed within the UHV vacuum chamber as shown in Fig.6.5 indicating that the chamber was now ready to trap cold atoms. The absorption signal is weak due to the low Rb pressure within the UHV cell.

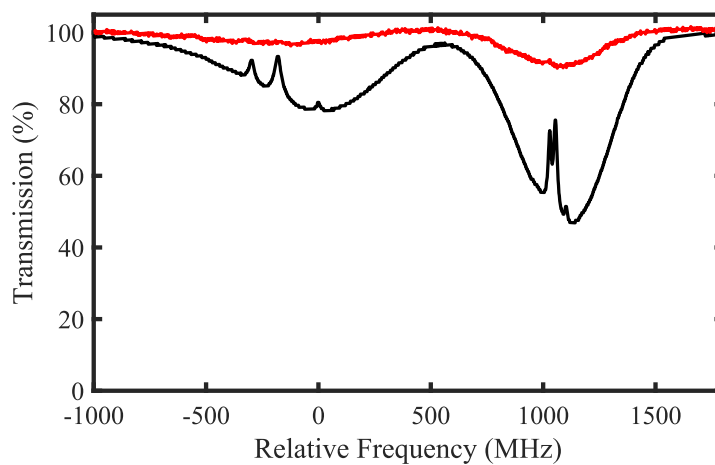


Figure 6.5: Simultaneously monitored absorption spectra of the D_2 line in Rb for a double passed 7 cm reference cell (black) and the UHV cell with 6 passes (red).

6.3 Experimental Setup

Now with the UHV cell prepared, it was integrated into a pre-existing laser cooling apparatus, which was previously employed by Bregazzi *et al* [138]. However, the AOM in the system, previously used for frequency tuning, was replaced with the Zeeman tunable wavelength reference discussed in Chapter 5. The trapping light was provided by a volume Bragg grating (VBG) laser, which was split into two arms with a polarising beam splitter. The first arm was coupled into the Zeeman tunable wavelength reference, which was employed to both stabilise the laser and provide the red-detuning required to form a MOT. The second arm

from the PBS was passed through a free-space electro-optical-modulator (EOM), which phase modulated the incident light at 6.58 GHz to generate 5% sidebands to address the $F=1$ to $F'=2$ transition for hyperfine re-pumping in the laser cooling process. The light is then fibre-coupled and expanded in free-space to the cold-atom system as shown in Fig.6.6.

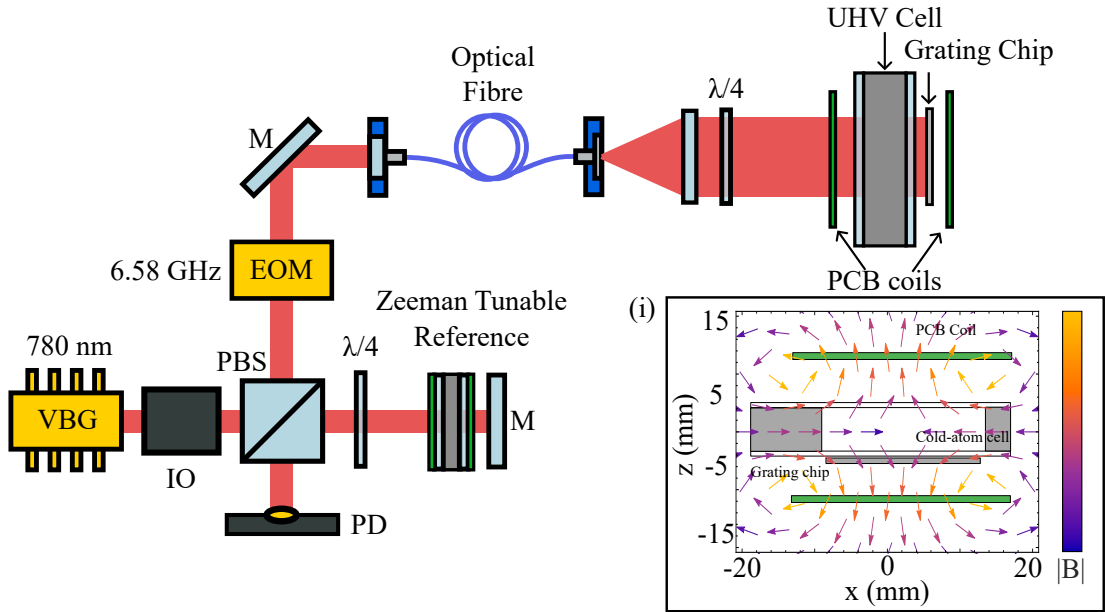


Figure 6.6: Laser system for chip-scale cold-atom platform. VBG: volume Bragg grating laser, IO: optical isolator, PBS: polarising beam splitter, $\lambda/4$: quarter waveplate, M: Mirror, PD: photodiode and EOM: electro-optic modulator. (i): Simulated magnetic field generated from the PCB coils for trapping.

To further aid miniaturization, of the cold atom system the traditionally large wire-wound anti-Helmholtz coils previously used to create the required gradient field for trapping have been replaced in favour of a pair of PCB coils, which sandwiched the cold-atom cell and grating chip. These PCB coils were designed alongside the offset lock PCB coils as discussed in Chapter 5 as such they had the same spiral pattern, board thickness and wire properties. Each of these PCB coils had a total of 30 turns, with a mean radius of 12.5 mm ($R_{min} = 10.2$ mm, $R_{max} = 14.9$ mm). Each double-sided PCB coil had a resistance of $10\ \Omega$ and are approximated to require 1 A of current to produce a magnetic field gradient

of 20 G/cm, with the field orientation relative to the other system components shown in Fig. 6.6 with opposite current polarity in each coil. The current flowing through the coils was controlled by a power supply in constant current mode.

The light was circularly polarized with a $\lambda/4$ wave-plate before being incident through the UHV cold-atom cell onto a micro-fabricated TRI grating chip, which provides the required beams for trapping. The light incident on the UHV cell had a peak intensity of $\approx 13 \text{ mW/cm}^2$. The grating chip was placed immediately below the cold-atom cell lower window to ensure a maximum optical overlap volume exists within the cold-atom cell vacuum volume. The cold-atom cell outer dimensions are $70 \text{ mm} \times 34 \text{ mm} \times 7.4 \text{ mm}$ with a $20 \text{ mm} \times 20 \text{ mm} \times 6 \text{ mm}$ laser cooling region, which accommodates the surface area of the grating chip. The 3-segment grating chip was fabricated with a 1100 nm period over the $2 \text{ cm} \times 2 \text{ cm}$ surface area of the chip. At the centre of the grating, a 2 mm diameter hole has been laser cut for optical access and imaging [138] however, it was not exploited within this work.

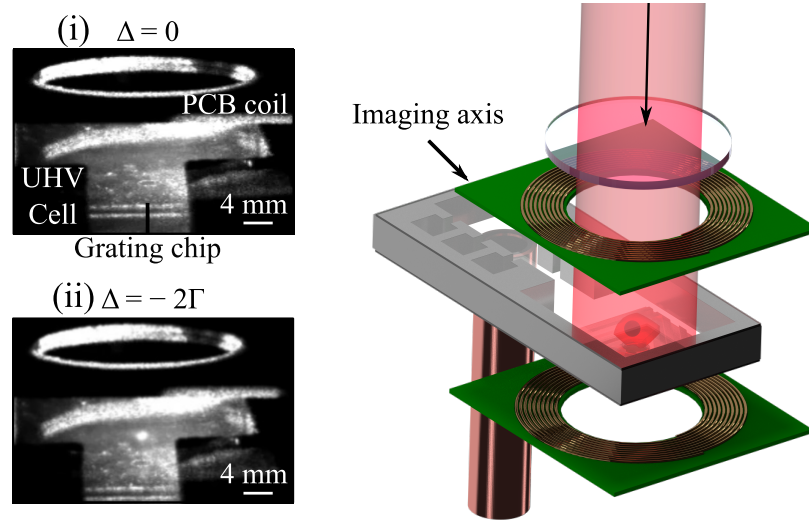


Figure 6.7: UHV cell-GMOT incorporated laser cooling platform with planar coils with example images of from the imaging axis (i) when $\Delta = 0$ no MOT visible and (ii) $\Delta = -2\Gamma$ with a MOT clearly visible.

In previous work, absorption imaging through the grating chip was required to overcome surface scatter and resolve the trapped atom number [138]. However,

this approach was not suited to the current apparatus due to the removal of the AOM from the laser system, which was previously used for intensity control in the imaging light sequence. Instead, this generation of the cold-atom cell was fabricated with a $30\text{ mm} \times 8\text{ mm} \times 6\text{ mm}$ channel leading from the pinch-off region to the cooling region to enable fluorescence imaging of the cold-atoms by allowing for a low angular displacement of $\approx 20^\circ$ between the cell and imaging system. The low incident angle for imaging avoids diffracted orders from the grating chip and greatly reduces the surface scatter from the cell walls, glass and grating. An example of this imaging axis is shown in Fig. 6.7 with typical images of the cold atom vapour cell taken from the imaging axis shown for trapping laser frequency detuning of $\Delta = 0$ and $\Delta = -2\Gamma$ respectively.

6.4 Results

To determine the number of trapped atoms within the MOT we employ fluorescence imaging. This technique involves measuring the change in fluorescence measured on a photodiode as atoms are loaded into the trap after the gradient field is turned on. This change in fluorescence is typically referred to as a 'rise-curve' from which both the trapped atom number and cell pressure can be extracted. An example rise curve from the cold-atom cell is shown in Fig.6.8.

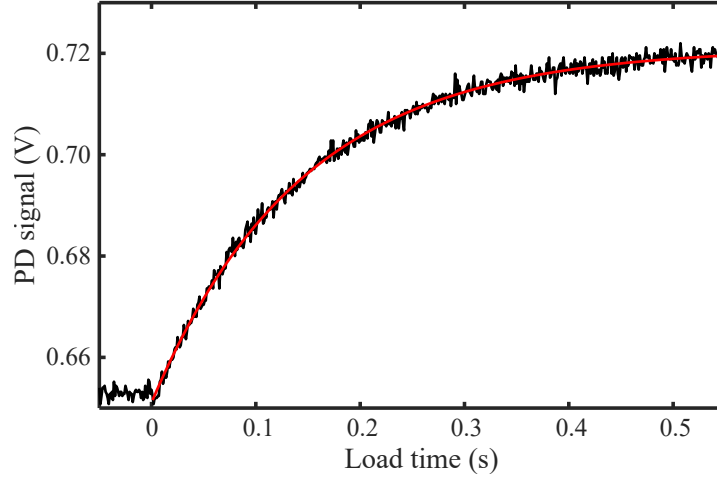


Figure 6.8: A typical MOT rise-curve obtained within the cold-atom vapour cell for a trapping laser detuning of $\Delta/2\pi = -12$ MHz and gradient field of 20 G/cm.

Assuming that the MOT behaves like a point source and isotropically radiates light, we can relate the number of trapped atoms to the measured voltage V by using the energy of the emitted photons ($E = hc/\lambda$), the rate at which photons are emitted R_{sc} , the efficiency of the photodiode η , and the relative solid angle Ω of fluoresced light, which reaches the photodiode. This relationship is given by,

$$N = \frac{4\pi}{\Omega} \frac{\lambda}{hc} \frac{V}{z R_{sc} \eta}, \quad (6.7)$$

where z is the impedance of the photodiode. Here we use $I_{sat} = 1.6$ mW/cm² [24] to calculate R_{sc} . Additionally by fitting the rise-curve with an exponential of the form,

$$V(t) = A \left(1 - \exp\left(-\frac{t}{\tau}\right) \right) + B, \quad (6.8)$$

for $t > 0$. Where A represents the amplitude of the signal and B the photodiode offset. From this fit, the loading time τ can be extracted, which can be related to the pressure within the cell through the relation 2×10^{-8} Torr/ τ [141]. From the MOT rise curve, we estimate the pressure within the UHV cell to be $\approx 1 \times 10^{-7}$ Torr.

To determine the maximum number of trapped atoms within the UHV vapour cell the trapped atom number was measured as a function of both the trapping

laser detuning Δ and the gradient field as shown in Fig.6.9. From these measurements we obtained an optimised atom number of $N = 4 \times 10^6$ atoms at $\Delta/2\pi = -11$ MHz with a gradient field of 20 G/cm. This trapped atom number is consistent with previous GMOT experiments, which for a grating with the same structure and experimental conditions have realised trapped atoms numbers of $\approx 10^6$ [142].

The atom number demonstrated here could be improved by an order of magnitude by increasing the trapping laser intensity [142] however, due to the limited available optical power in the laser system this could not be explored. The demonstrated trapped atom number is already an order of magnitude improvement in trapped atom number over previous generations of chip-scale cold atom vapour cells [138]. This improvement was attributed to the increased cell volume, which allows a majority of the GMOT optical overlap volume to coincide within the cold-atom cell [138].

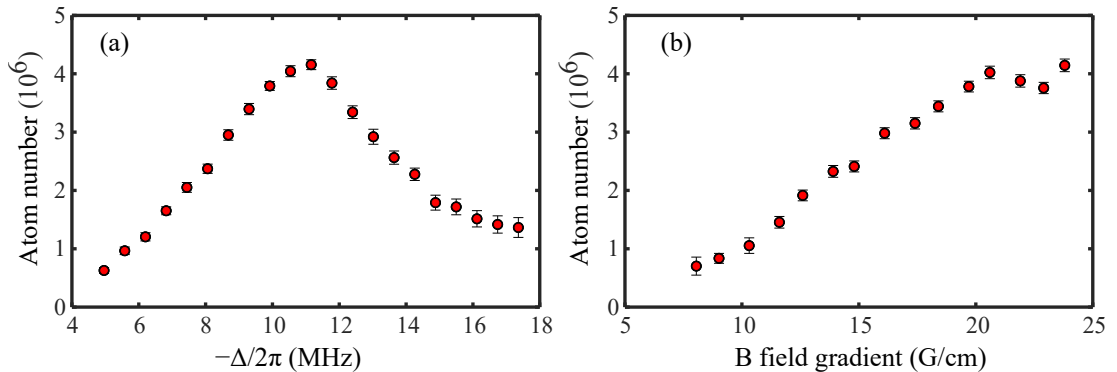


Figure 6.9: (a): Atom number as $\Delta/2\pi$ was tuned between -5 to -17 MHz with the gradient field held at 20 G/cm. (b): Atom number as the gradient field was varied with $\Delta/2\pi$ held constant at -11 MHz.

The demonstrated trapped atom number and cell pressure are promising for the development of a chip-scale cold atom platform for an atomic clock. In the case of an atomic clock utilising a Ramsey style interrogation [143], the attainable stability can be limited by the number of atoms being interrogated. This limitation is referred to as quantum projection noise, which can be approximated

by [144],

$$\sigma(\tau) = \frac{\Delta\nu}{\pi\nu_0} \sqrt{\frac{T_c}{\tau}} \sqrt{\frac{1}{N}}, \quad (6.9)$$

where ν_0 is the central frequency given by the hyperfine spacing of the ground states for ^{87}Rb $\nu_0 = 6.8$ GHz, $\Delta\nu$ is the linewidth of the Ramsey fringe given by $1/T$ where T is the Ramsey time and T_c is the experimental cycle time. Here we estimate an experimental cycle time of 200 ms to allow for the trapping of 10^6 atoms with a Ramsey time of $T = 10$ ms, from which we estimate an quantum shot-noise limited performance of $1 \times 10^{-12} \tau^{-1/2}$.

Finally, we investigated the compatibility of the chip-scale cold atom platform with the Zeeman tunable wavelength reference by monitoring the stability of the atom number over a period of 20 mins. This measurement time was limited to 20 mins as the trapping laser would periodically unlock, disrupting longer measurements. These laser unlocks were attributed to issues with the laser controller used to stabilise the trapping laser.

During this measurement $\Delta/2\pi$ was set to -12 MHz with a gradient field of 20 G/cm to realise an average trapped atom number of $\approx 3 \times 10^6$. Throughout this measurement the atom number was measured once every second via MOT rise curves, by switching the gradient field on and off with a 50% duty cycle, which was controlled through LabVIEW. Simultaneously the frequency stability of the cooling laser was monitored with the same beat note setup employed in Chapter 5 with a reference ECDL stabilised to the $F = 2 \rightarrow F' = 2, 3$ cross-over transition. The relative stability of the wavelength reference is illustrated in Fig. 6.10 (a) from which we observe a flat slope of τ^0 indicating a systematic limit [105]. The observed relative frequency stability is on the order of 10^{-11} for all averaging windows. While the observed stability is degraded compared to the results presented in Chapter 5, the laser's frequency only drifted by 100 kHz over the course of the measurement. This drift is well below the 6 MHz linewidth of the cooling transition. Further to this, when the tunable wavelength reference was replaced with a 7 cm reference cell, a similar stability was observed, as demonstrated in Fig. 6.10 (a), indicating that the stability was not limited by

the wavelength reference package.

The simultaneously measured atom number stability, shown in Fig. 6.10 (b), averages down with a slope of $\tau^{-1/2}$, demonstrating that over this measurement period, the frequency fluctuations of the trapping laser had no discernible effect on the stability of the trapped atom number. This result further validates the suitability of the Zeeman tunable wavelength reference as a replacement for an AOM for frequency control in laser cooling apparatuses.

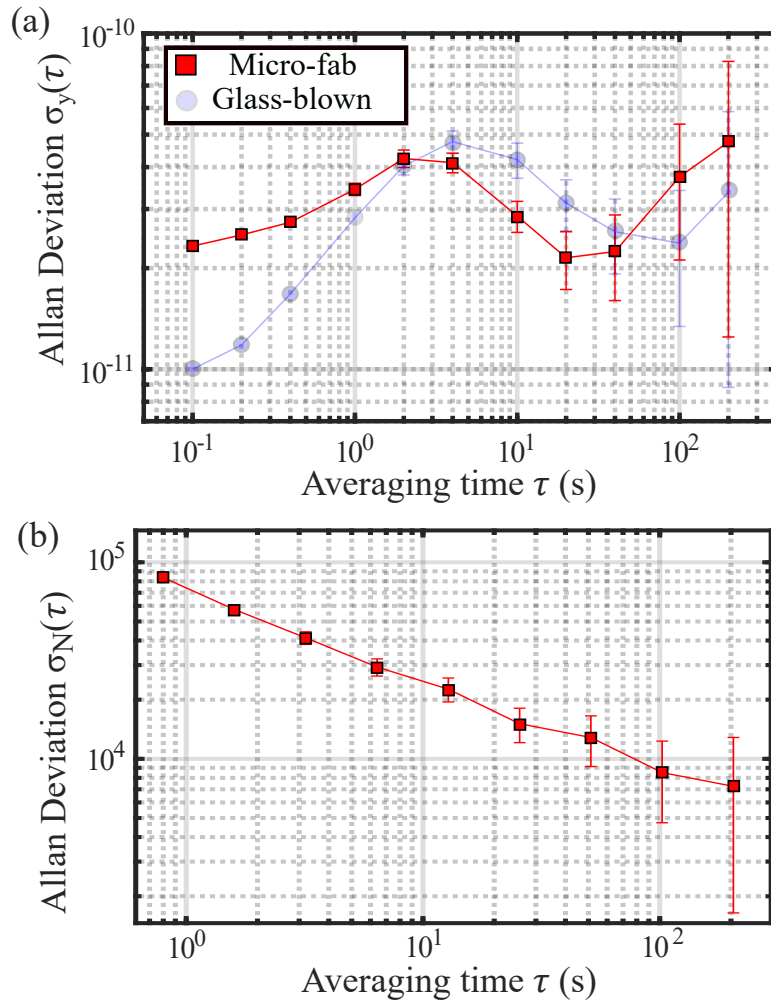


Figure 6.10: (a): Overlapping Allan deviation of the beat note signal when the VBG laser is stabilised to the tunable wavelength reference and a 7 cm reference cell, shown in red squares and blue circles respectively. (b): Simultaneously measured atom number stability from the cold-atom cell.

6.5 Conclusions and Future Work

To conclude, we have demonstrated a new generation of chip-scale cold atom platforms with a micro-fabricated UHV vapour cell with a demonstrated trapped atom number of 10^6 , which is compatible with miniaturisation of cold atom clocks. Additionally we have shown the compatibility of the cold atom platform with a compact Zeeman tunable wavelength reference package to aid in the further reduction in size of the cold atom apparatus.

Unfortunately, the cell experienced a blunt strike, which cracked one of glass windows compromising the hermeticity of the cell. Due to time constraints we never fabricated a replacement UHV cell and so the study was concluded. However, there were still some additional experiments we wanted to carry out with the setup, which hopefully can be addressed in future work.

Firstly, we would like to determine what is the attainable temperature of the cold atom cloud after an optical molasses sequence with the Zeeman tunable wavelength reference and how does it compare to the temperatures attainable with a more complex laser system. Additionally, we are interested in investigating the longevity of the UHV cell's vacuum pressure without the presence of active pumping, comparing the results to existing works on passively pumped UHV cells for cold atoms [134, 135, 137].

Chapter 7

Elongated Vapour Cell for a Two-Photon Optical Clock

Accurate timing plays a fundamental role in various aspects of modern life, including telecommunications, power distribution and financial trading [145, 146]. These critical infrastructures receive timing signals from global navigation satellite system (GNSS), which are susceptible to disruption via malicious attacks such as jamming [146, 147] that can lead to outages putting these vital services at risk. Due to this vulnerability there is a growing interest in the development of high performance field deployable atomic clocks, which can be employed to provide timing during GNSS outages [148]. The aim for these compact atomic clocks is to achieve a performance similar to or better than a caesium beam clock with a short-term stability of $\leq 10^{-12}/\sqrt{\tau}$ whilst maintaining a total package size of ≤ 1 L [149, 150].

In pursuit of this goal, there has been significant interest in compact optical clocks, which exploit simple Doppler-free spectroscopic techniques on thermal atoms and molecules [151–154]. A particularly promising candidate is based on the $5S_{1/2}$ to $5D_{5/2}$ two-photon transition in Rb, which offers a narrow transition with a natural width of 330 kHz. These transitions can be readily observed via fluorescence with a high SNR due to the large number of thermal atoms, which contribute to the signal [154]. Recently a team at NIST demonstrated a compact

optical frequency standard based on the interrogation of a 2 mm thick micro-fabricated vapour cell, which achieved a short-term stability of $\approx 1 \times 10^{-13}/\sqrt{\tau}$ limited by the SNR of the fluorescence signal [81].

Previous studies within our research group have found that the two-photon signal obtained from a micro-fabricated vapour with a 1 mm path length was $\times 75$ weaker than the signal obtained from a 25 mm glass-blown cell under the same experimental conditions [155], which was attributed to the reduced interaction length within the micro-fabricated cell. According to Eq.5.5, this reduction in SNR is expected to degrade the stability by a factor of 75. Here, we investigate the fabrication of micro-fabricated vapour cells with an elongated geometry with an optical path length of 40 mm. This increased optical path length has the potential to improve the performance of two-photon optical clocks whilst still maintaining a compact package size.

7.1 Degenerate Two-Photon Spectroscopy

Before discussing the fabrication and characterisation of micro-fabricated cells with an elongated geometry, we will give a brief overview of degenerate two-photon transitions. These transitions involve the simultaneous absorption of two photons from a single laser beam with frequency ω , which can occur when the following condition is satisfied [156],

$$E_e - E_g = 2\hbar\omega. \quad (7.1)$$

This two-photon excitation can be understood as a two-step absorption process from a ground state (E_g) via a virtual state to an excited state (E_e) as illustrated in Fig.7.1. The virtual state, represents the off-resonant interaction with intermediate transitions, which couple the ground and excited states [157]. The transition probability $A_{ge} \propto \frac{I^2}{\Delta}$ [157], where Δ is the detuning of the virtual state from any intermediate transitions and I is the intensity of the interrogating beam.

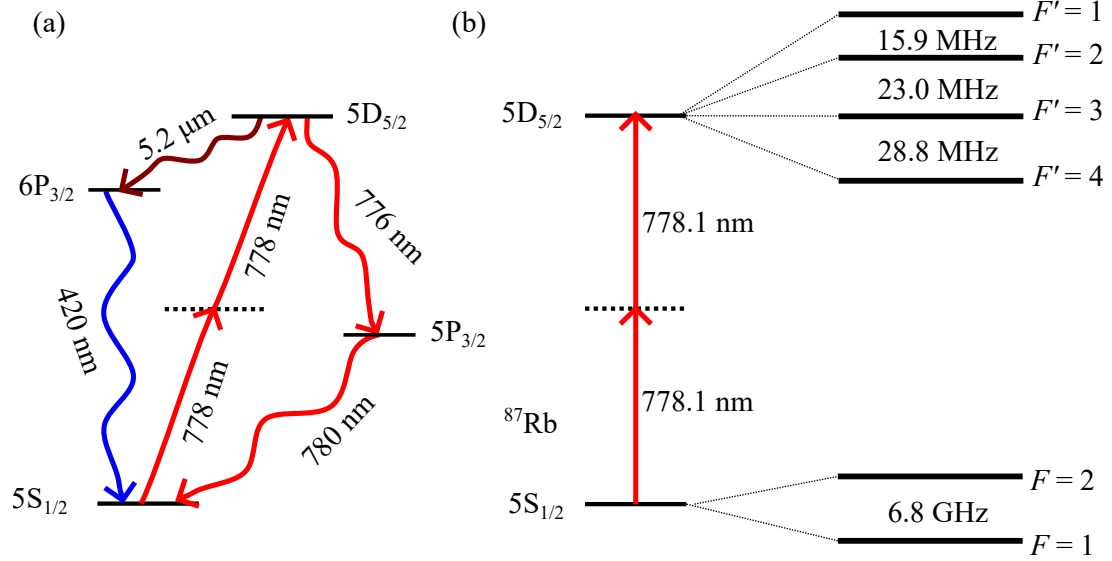


Figure 7.1: (a): An illustration of the degenerate two-photon excitation from $5S_{1/2}$ to $5D_{5/2}$ in Rb with the different decay paths back to the ground state highlighted. (b): The hyperfine energy levels for the $5S_{1/2}$ to $5D_{5/2}$ transition in the case of ^{87}Rb .

In the case of the $5S_{1/2}$ to $5D_{5/2}$ two-photon transition in ^{87}Rb , which is driven at 778 nm the intermediate state is detuned by 2 nm , allowing for a reasonable transition probability at modest probe intensities ($I \geq 0.1\text{ W/cm}^2$) [154, 155]. Additionally, the off-resonant interaction with the intermediate state has the effect of greatly reducing saturation effects such that power broadening has a negligible contribution to the observed two-photon line shape at intensities around 10 W/cm^2 [155]. This two-photon transition can be readily observed via the cascaded fluorescence either from $5D_{5/2}$ to $5P_{3/2}$ at 776 nm or from $6P_{3/2}$ to $5S_{1/2}$ at 420 nm . When decaying from the $5D_{5/2}$ state a 776 nm photon is $\times 10$ more likely to be emitted than a 420 nm photon [158]. The fluoresced light is separated from the probe light with the use of optical filters before detection. However, due to difficulties with separating the 776 nm light from the probe light the 420 nm light is typically observed with a larger SNR [158] and so is the preferred method of detection for two-photon based optical atomic clocks [81, 154, 159].

The natural width of the $5D_{5/2}$ state is $\Gamma_{\text{nat}}/2\pi = 670\text{ kHz}$ [160]. However, when being probed via the degenerate two-photon transition, the linewidth is ob-

served to be halved to ≈ 330 kHz. As discussed earlier in chapter 3, when probing a thermal ensemble of atoms, the Doppler effect leads to a dominant Doppler-broadened profile ($\Gamma_D/2\pi \approx 500$ MHz). However, in the case where the atoms are addressed by two counter-propagating beams, the two-photon resonance condition becomes modified to be [156],

$$E_e - E_g = \hbar(\omega - k \cdot v) + \hbar(\omega + k \cdot v) = 2\hbar\omega. \quad (7.2)$$

We can observe that since the counter-propagating beams experience an equal and opposite Doppler shift, the Doppler broadening is eliminated. This ensures that all atoms, irrespective of their velocity, can contribute to a Doppler-free signal [156]. While two co-propagating photons can still be absorbed, contributing to a Doppler broadened signal, it's strength is much weaker than the Doppler-free signal, since $\Gamma_D \gg \Gamma_{\text{nat}}$ [155, 161].

Notably, Doppler broadening is only fully suppressed when the two interacting photons are perfectly counter-propagating. When there is an angle θ between the interacting photons, a residual Doppler broadening of the Doppler-free spectroscopic signal is observed. This has been empirically determined for small angles to take the form $\Gamma_{\text{RD}} \approx \theta \Gamma_D$ [162]. Residual Doppler broadening can arise either through the misalignment [163] or scattering of the interacting beams [164].

7.2 Wet Etched Silicon Reflector

An established method to produce an elongated micro-fabricated cell is to wet etch silicon with potassium hydroxide (KOH) to create integrated reflectors out of the cell walls for light routing [18]. This fabrication approach has been leveraged by multiple research groups to increase the achievable optical path length within a micro-fabricated cell, which has benefited the performance of their chip-scale atomic devices [18, 23, 165]. This technique exploits the anisotropic nature of the KOH etch, which selectively attacks the $\{111\}$ plane of silicon at the slowest rate, resulting in angled walls inclined at 54.7° with respect to the $\{100\}$ wafer surface plane. However, due to the non-ideal angle of the $\{111\}$ plane reflectors,

additional optics are necessary to route light into and out of the cell such as diffractive optical elements (DOE) [23]. Unfortunately, these components require an additional independent fabrication process and introduce undesirable optical losses [23]. Alternatively, we investigated leveraging the same wet etching process used to form the internal cell reflectors to produce external reflectors at 54.7° , which can be arranged in a periscope configuration with the internal cell reflectors for light routing, as illustrated in Fig.7.2 (a).

The vapour cell fabrication was carried out by KNT with a simplified fabrication process illustrated in Fig.7.2 (b). Initially, a 1 mm thick silicon wafer with a surface plane of $\{100\}$ was coated with photoresist, which was patterned with DRIE to produce a mask for etching. The silicon wafer underwent wet etching with KOH to create a $900\ \mu\text{m}$ deep and 40 mm long trench with angled walls at 54.7° . Following this, DRIE etching was employed to create cavities where alkali dispenser and NEG pills could be inserted. The wet etched trench was then coated with 150 nm of aluminium via an evaporation process, enhancing the reflectivity of the internal reflectors from 33% to 87% at 778 nm [166]. A glass wafer was bonded to the lower surface to form a cell preform into which an alkali dispenser (SAES Rb/AMAX/Pill1-0.6) and NEG pills (SAES ST172) were placed. A final bonding step to seal the cell was conducted in a vacuum bonding station evacuated to $<10^{-5}$ Torr.

Simultaneously, another wafer was processed alongside the first wafer to produce the external reflectors. After processing, this wafer was mechanically diced into individual reflectors, which were then manually positioned by hand and adhered to the surface of the cell with UV curing epoxy. Epoxy was chosen over anodic bonding due to concerns about potential shifts in the reflector's position during the bonding process, which could impact the coupling both into and out of the cell. The cell was then placed within the laser activation setup and the alkali dispenser was activated with 1 W for 10 s, which was found to release an ample amount of Rb with condensed droplets still visible when operating the cell at 120°C . The NEG pills were then individually activated with 3 W for several

minutes with the goal of removing all getterable contaminants released during the cell fabrication and alkali dispensing processes.

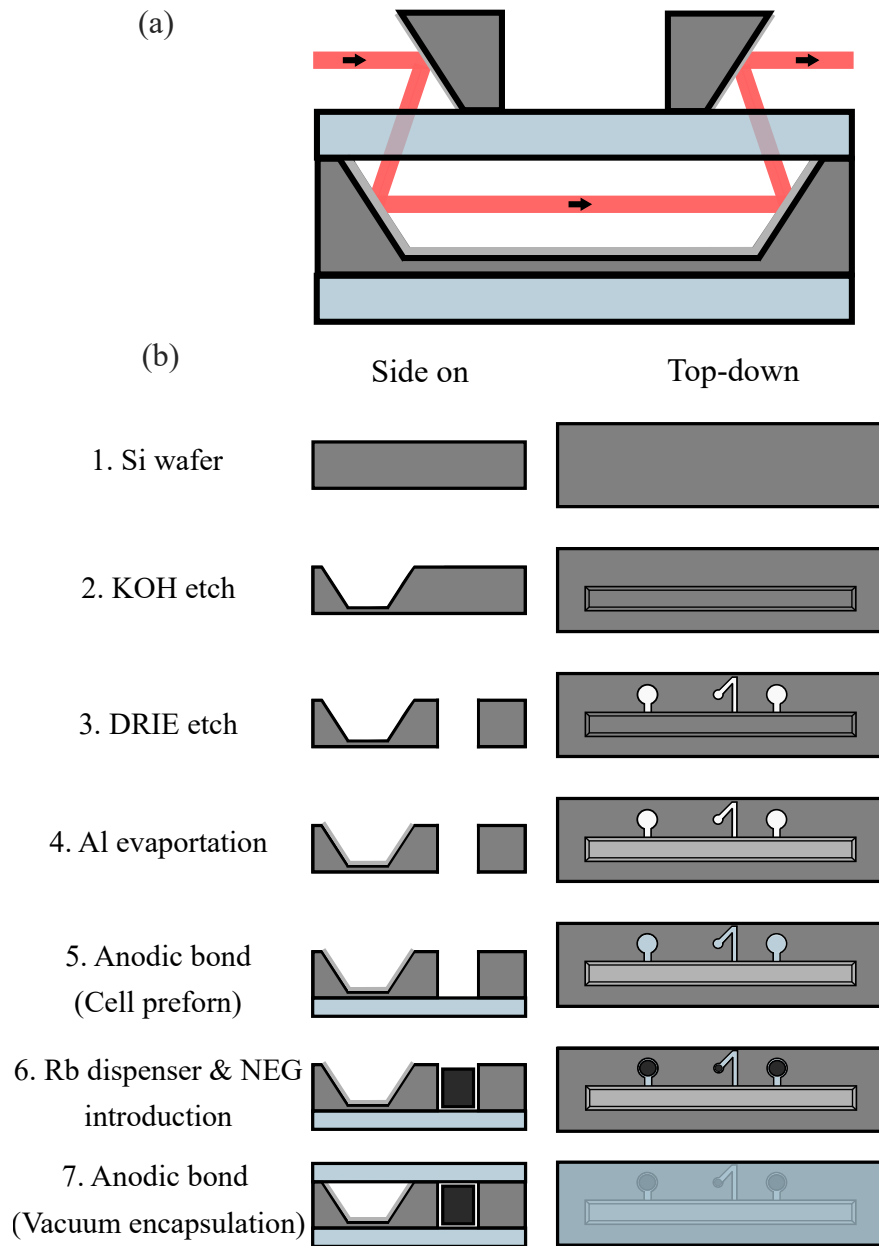


Figure 7.2: (a): An illustration of light routing in the assembled periscope cell. (b): Fabrication process of the elongated periscope cells. The side on illustrations show a cross-section through the middle of the cell.

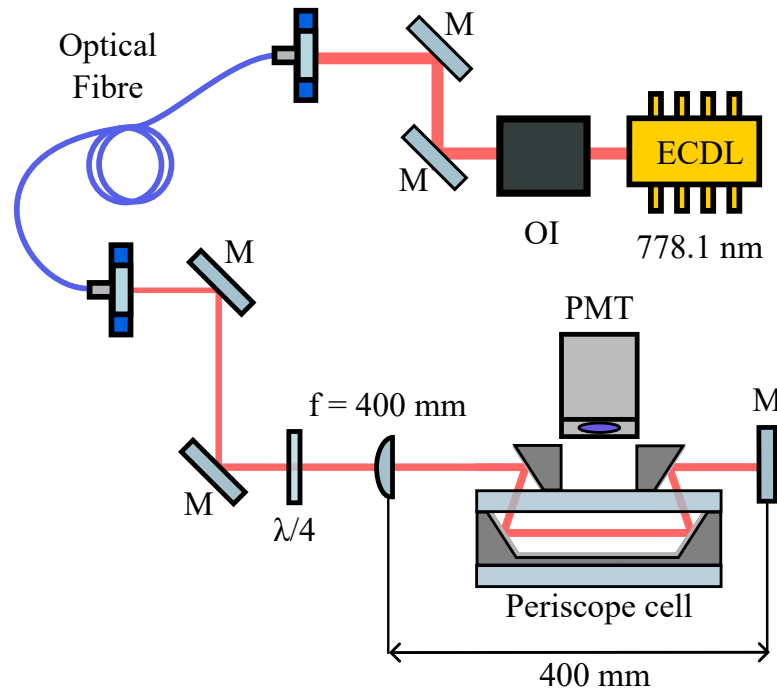


Figure 7.3: An illustration of the optical setup for two-photon spectroscopy. ECDC: External Cavity Diode Laser. OI: Optical Isolator. M: Mirror. PMT: Photomultiplier Tube.

The periscope cell was then implemented into a two-photon spectroscopy setup as illustrated in Fig.7.3. This experimental setup was comprised of an ECDC laser tuned to 778.1 nm, which was then coupled into a single-mode polarisation maintaining fibre. This was done to transfer the light to an optical board containing the spectroscopy setup and to improve the spacial mode of the laser to aid in coupling into the periscope cell. At the output of the fibre 8 mW of light was collimated to a Gaussian beam waist of 0.75 mm ($1/e^2$ radius), the beam was then incident onto two steering mirrors. Before the cell the light was circularly polarised with a $\lambda/4$ wave-plate to drive the atoms with the $\sigma^+ + \sigma^+$ scheme, which has previously been shown to maximise the strength of the two-photon signal for S to D transitions [161]. Subsequently the light was focused with a 400 mm lens onto the retro-reflecting mirror, producing a beam waist at the focus of $\approx 130 \mu\text{m}$. This was done to ensure that the beam diameter remained $< 900 \mu\text{m}$ to prevent clipping as the light traversed the cell in its retro-reflecting configuration. The steering mirrors were then used to optimise alignment through

the periscope cell, where the off-resonant transmission was found to be $\approx 50\%$, in reasonable agreement with the expected optical losses of 57% from four reflections off of aluminium coated surfaces, indicating good coupling into and through the cell.

The periscope cell was mounted on a piece of aluminium with an embedded ceramic heater, which was used to heat the cell to 110°C . This heating was required to achieve a sufficient alkali density, to produce a clear two-photon signal. A photomultiplier tube (PMT) was positioned 15 mm above the cell to detect the cascaded 420 nm fluorescence signal with a bandpass filter (Semrock: FF01-420/5-25) placed in front of the detector to block both the background light and the probe beam. The ECDL's frequency was scanned across the $5S_{1/2}$ to $5D_{5/2}$ two-photon transitions from the $F = 2$ ground state in ^{87}Rb and the frequency spacing between the $F' = 4$ and $F' = 3$ transitions was used to calibrate the laser frequency scan assuming that it is linear over this range.

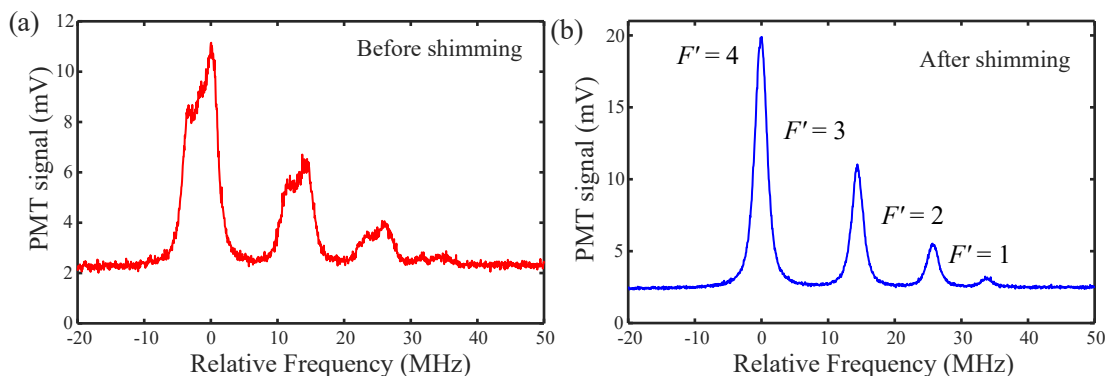


Figure 7.4: (a): The observed spectrum when scanning the laser frequency across the two-photon transitions from $F = 2$ without shimming. (b): After shimming the stray fields with three-axis Helmholtz coils.

Initially, we observed that the two-photon transitions were broadened with a linewidth of ≈ 5 MHz as shown in Fig.7.4 (a). Additionally, we observed that each transition exhibited a splitting that indicated that the broadening was due to the presence of stray magnetic fields. These stray magnetic fields lifted the degeneracy of the individual transitions between m_F levels resulting in a Zeeman

broadening of the transition [155]. To compensate for these stray fields, three-axis Helmholtz coils were placed around the cell. The current in each pair of coils was adjusted to maximise the signal strength and minimise the observed linewidth with the optimised spectra shown in Fig.7.4 (b). The linewidth was determined by fitting the $F = 2 \rightarrow F' = 4$ transition with a Lorentzian profile. After shimming we obtained a linewidth of 1.7 ± 0.1 MHz with the resulting fit shown in Fig.7.5.

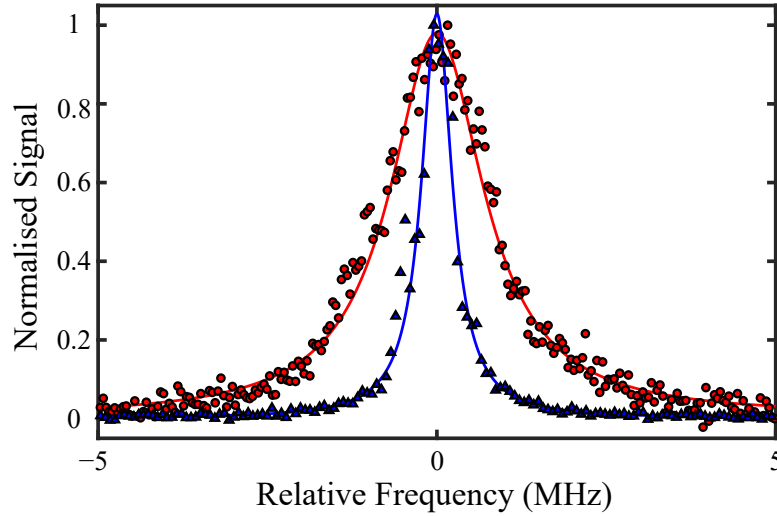


Figure 7.5: ^{87}Rb $F = 2 \rightarrow F' = 4$ two-photon signal (single-shot) from the periscope cell (red circles) and a glass-blown reference (blue triangles) with Lorentzian fits in solid red and blue lines respectively with FWHM of 1.7 ± 0.1 MHz (periscope) and 600 ± 100 kHz (glass).

To ensure that the observed linewidth was not arising due to an unknown experimental systematic the measurement was repeated in a 7 cm reference cell within the same experimental setup under the same conditions. For the reference cell a much narrower linewidth of 600 ± 100 kHz was observed. Assuming that the excess broadening observed in the glass-blown cell is arising due to broadening mechanisms with a Lorentzian profile, we can deduce a systematic broadening by simply subtracting the natural width from the observed width. We estimate this systematic broadening to be ≈ 300 kHz, likely arising from broadening mechanisms such as laser linewidth, pressure broadening and transit time [167].

Even after taking into account the systematic broadening, the periscope cell still exhibited roughly 1 MHz of residual broadening. This excess broadening was significantly greater than the expected pressure broadening of ≈ 200 kHz, attributed to non-getterable contaminants released from the alkali dispenser during activation [81]. Instead, the discrepancy in linewidth was attributed to residual Doppler broadening, arising from light scattering off the textured surface of the micro-fabricated reflectors, as clearly depicted in Fig. 7.6 (a) and (b). Surface irregularities are known to arise due to various technical issues, which can occur during the wet etching process [168, 169].

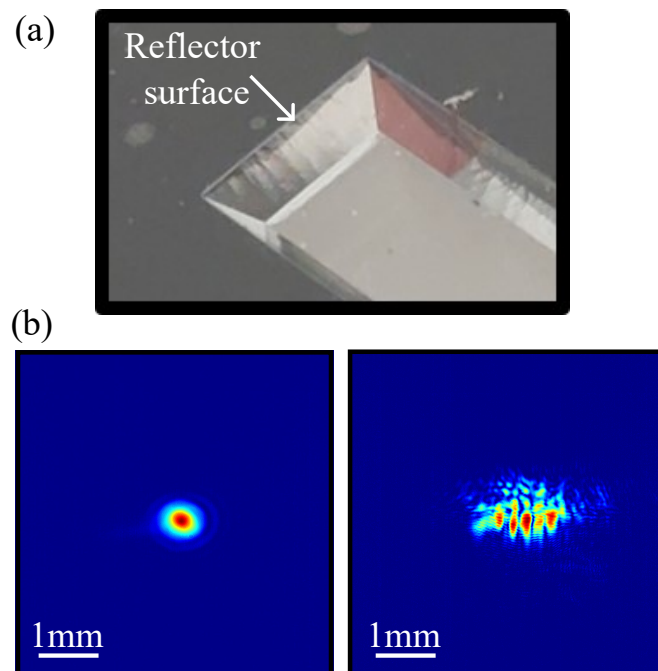


Figure 7.6: (a): Microscope image of an internal periscope cell reflector with the textured surface clearly visible. (b): Image of the interrogating beam taken on a CMOS sensor (i) before and (ii) after a single pass through the periscope cell.

From these results we can see that the current realisation of the periscope cell was not well suited for use in a high performance two-photon clock where the transition linewidth is typically ≈ 600 kHz [81, 154]. Due to time constraints subsequent iterations of the periscope cell with improved reflector quality were not pursued. Instead an alternative fabrication route was investigated to achieve

a two-photon signal with a narrow linewidth suitable for two-photon clocks.

7.3 Commercial Prism Reflectors

An alternative route to fabricating an elongated micro-fabricated cell was demonstrated by Nishino *et al.* [170], where they anodically bonded custom 45° BSG reflectors within a cell to realise an optical path length of 8 mm. This is a promising alternative to wet etched silicon reflectors however, it requires the fabrication of custom reflectors. Before investigating the fabrication of custom anodically bondable reflectors, we first examined the feasibility of utilising commercial off the shelf (COTS) prism reflectors as a potential route to realise an elongated cell. Additionally such a cell would allow for us to verify that the performance limitation of the periscope cell was indeed due to the quality of the wet-etched reflectors. The prism reflectors, sourced from Thorlabs (part no: MRA05-E03), are designed to reflect incident light at an angle of 90°, as depicted in Fig.7.7 (a).

This vapour cell was fabricated inhouse with an overview of the cell fabrication process illustrated in Fig.7.7 (b). The prism reflectors had a height of 5 mm, so the cell frame was constructed from a 6 mm thick silicon wafer, which was readily available at the time. The cell frame was water-jet cut to be 40 mm × 5 mm and include two square cavities where the prism reflectors could be securely positioned and held in place with friction. This approach to secure the reflectors was required as they were made from NKB-7 glass, which is not conducive to anodic bonding with silicon due to the large mismatch in CTE [171]. Next, a BSG glass wafer was anodically bonded to the base of the silicon frame to form a cell preform using the atmospheric bonding station. Within this preform, the prism reflectors were placed alongside an alkali pill source (SAES Rb/AMAX/Pill1-0.6) and a NEG pill (SAES ST172). Then the cell was sealed by anodically bonding a BSG wafer to upper surface of the silicon frame within a vacuum bonder at a pressure of $<10^{-5}$ mbar.

After fabrication, the alkali dispenser and NEG pill within the cell were ac-

tivated with a similar process to what was discussed in Section.7.2. Following this the COTS cell was implemented into the two-photon experimental setup and the FWHM of the ^{87}Rb $F = 2 \rightarrow F' = 4$ two-photon transition was measured to be 790 ± 40 kHz with the data and subsequent fit shown in Fig.7.8. The observed linewidth within the COTS cell was approximately 200 kHz wider than that obtained in the reference cell for the same experimental conditions. This discrepancy is consistent with the expected pressure broadening from the alkali pill source [81]. Furthermore this result from the COTS cell provides additional evidence that the performance of the periscope cells was limited by the quality of the wet etched reflectors.

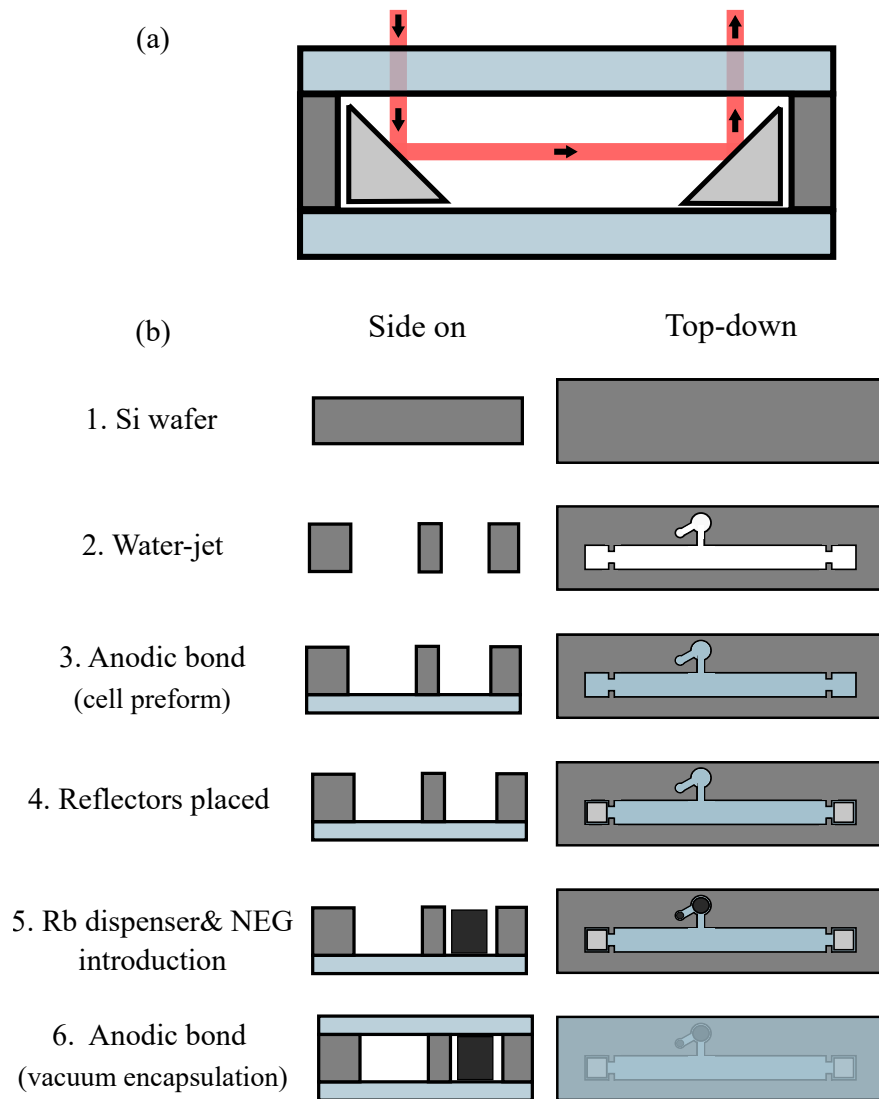


Figure 7.7: (a): Light routing in the COTS elongated cell. (b): Fabrication process of the COTS elongated cells. The side on illustrations show a cross-section through the middle of the cell.

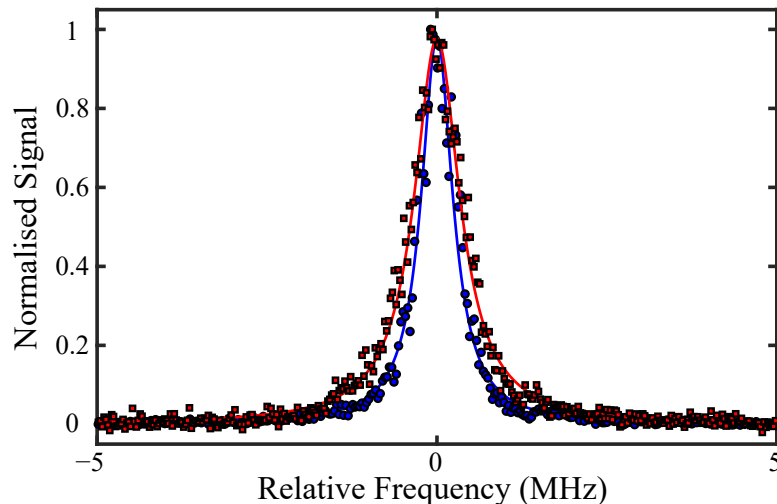


Figure 7.8: ^{87}Rb $F = 2 \rightarrow F' = 4$ two-photon signal (single-shot) from the COTS elongated cell (red circles) compared against the same signal obtained in a 7 cm reference cell (blue squares) and with Lorentzian fits in solid red and blue lines respectively with FWHM of 790 ± 40 kHz (COTS) and 600 ± 100 kHz (glass).

The demonstrated linewidth in the COTS is promising for use in a high performance two-photon optical clocks [81]. However, the reflectors within the cell are not adequately secured held in place and consequently, the cell was highly sensitive to misalignment and not robust enough for use in an optical atomic clock. Subsequent variations of the cell design were pursued to more tightly hold the prisms in place but this resulted in the prisms becoming damaged during the anodic bonding process due to the mismatched CTE between silicon and NKB-7 glass.

7.4 Conclusions and Future Work

While exploring fabrication methods for an elongated vapour cell intended for a two-photon optical clock, we have considered utilising wet-etched silicon reflectors and commercial off the shelf reflectors. However, both approaches encountered issues, rendering them unsuitable for our purposes. Consequently, we have shifted our focus towards the fabrication of custom-machined silicon reflectors. These reflectors can be anodically bonded to the base of the cell preform, as illustrated

in Fig.7.9.

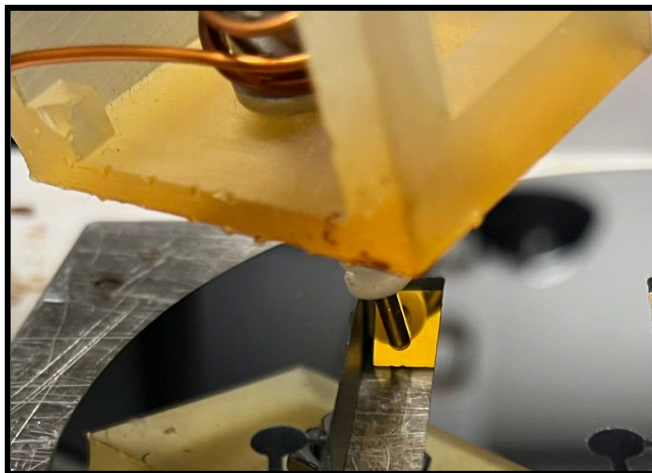


Figure 7.9: A photograph of a silicon reflector being anodically bonded into a cell preform.

The fabrication of the custom silicon reflectors as illustrated in Fig.7.10 begins with a 6 mm thick silicon wafer, which was initially mechanically diced into 6 mm×6 mm×6 mm cubes. The cubes are then diced diagonally to realise a surface at 45° with respect to its base, which will be used as the reflector surface. The dicing process leaves the 45° surface rough, which would lead to light scattering as was seen with the periscope cell so to reduce these effects the reflector surface was mechanically polished to improve its the surface quality.

The next step involves coating the silicon reflectors with gold to enhance their reflectivity. Previous studies have shown that alkali can react with gold, resulting in the darkening of the gold coating and subsequently a significant reduction in reflectivity [172]. However, recent work has demonstrated that gold coated mirrors can be integrated into micro-fabricated alkali vapour cells whilst still maintaining a high reflectivity [172]. This is achieved by applying a thin 10 nm protective layer of Al₂O₃ atop the gold coating. Although the fabrication of this cell is still ongoing at the time of writing this thesis once complete, it will be implemented into the two-photon experimental setup and undergo the same spectroscopic tests as previous cells to ensure the suitability of the reflectors.

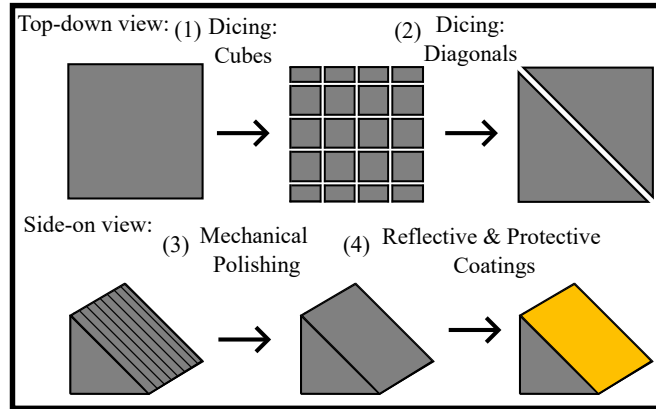


Figure 7.10: The fabrication process for the polished silicon reflectors.

After identifying a suitable approach for fabricating an elongated vapour cell for a two-photon optical clock, we can proceed to investigate the achievable stability with this cell geometry. To quantify the benefits of an elongated vapour cell, the obtained results will be compared against the performance obtained from micro-fabricated vapour cells of various path lengths under the same experimental conditions.

Chapter 8

Conclusion

Throughout this thesis we have discussed the development of micro-fabricated vapour cell technology for use in compact atomic devices such as magnetometers, optical wavelength references and cold atom sensors.

In Chapter 3 we introduced a novel vapour cell fabrication process using a water-jet cutter to create silicon frames. This process allowed for deep 6 mm cuts through silicon not achievable with conventional fabrication process. We then demonstrated micro-fabricated Rb vapour cells with a 6 mm optical path length. This fabrication process has since become the cornerstone of vapour cell production within our research group, being used to produce vapour cells discussed in chapters 4, 6 and 7.

Chapter 4 discussed a technique to controllably deplete the N_2 content within micro-fabricated cells via the laser heating of a NEG material. We then used this technique to investigate the relaxation rate of an FID magnetometer as a function of N_2 buffer gas pressure to determine the optimal pressure for a given cell geometry. We then investigated if the NEG material continued to consume N_2 after heating was removed. Over a period 100 days there was no observable change in N_2 pressure indicating the techniques suitability for atomic devices. Finally, we demonstrated that this gettering material can be used to remove all of the N_2 content within the cell to realise a low pressure cell, which could be used for a compact wavelength reference based on sub-Doppler spectroscopy.

Chapter 5 discussed a compact Zeeman tunable wavelength reference package, which could be used to miniaturise laser cooling setups. This package was comprised of saturation absorption spectroscopy on a 1 mm micro-fabricated vapour cell, which was sandwiched between two PCB coils. We observed that the lock point could be shifted ± 60 MHz, which is sufficient to form a MOT and for implementing an optical molasses sequence. Additionally we found that when detuned from resonance there was no observable change in stability to the resonant case.

Chapter 6 discussed the construction and characterisation of a 6 mm thick micro-fabricated UHV vapour cell for laser cooling. This UHV cell was then combined with a grating chip to realise a chip-scale cold atom platform, which was capable of trapping 4×10^6 atoms limited by the available laser power.

Chapter 7 discussed the fabrication and characterisation of micro-fabricated vapour cells with an elongated geometry for two-photon optical clocks. Initially we investigated the well established method of wet etching silicon with KOH to realise internal reflectors at 54.7° for light routing through the cell. However, this method resulted in imperfect reflectors, which scattered the probe light resulting in a residual Doppler broadening of the two-photon signal. We then investigated an alternative approach using COTS prism reflectors for light routing. This approach allowed for the two-photon transition to be resolved with a narrower linewidth however, due to the mismatched in CTE between silicon and the available prism reflectors(N-BK7) the reflectors could not be securely held in place. Informed from these studies into elongated cells we are now investigating silicon reflectors, which can be mechanically polished to reduce light scattering and can be anodically bonded into the cell pre-form securing them in place.

Bibliography

- [1] M. Takamoto *et al.*, *Test of general relativity by a pair of transportable optical lattice clocks*, Nat. Photon **14**, 411 (2020).
- [2] B. Stray *et al.*, *Quantum sensing for gravity cartography*, Nature **602**, 590 (2022).
- [3] M. T. Simons, A. B. Artusio-Glimpse, A. K. Robinson, N. Prajapati, and C. L. Holloway, *Rydberg atom-based sensors for radio-frequency electric field metrology, sensing, and communications*, Measurement: Sensors **18**, 100273 (2021).
- [4] R. Dawson *et al.*, *Portable single-beam cesium zero-field magnetometer for magnetocardiography*, Journal of Optical Microsystems **3**, 044501 (2023).
- [5] G.-W. Truong, E. F. May, T. M. Stace, and A. N. Luiten, *Quantitative atomic spectroscopy for primary thermometry*, Phys. Rev. A **83**, 033805 (2011).
- [6] M. Limes *et al.*, *Portable Magnetometry for Detection of Biomagnetism in Ambient Environments*, Phys. Rev. Appl. **14**, 011002 (2020).
- [7] B. Jadászliwer and J. Camparo, *Past, present and future of atomic clocks for GNSS*, GPS Solutions **25**, 27 (2021).
- [8] B. L. S. Marlow and D. R. Scherer, *A Review of Commercial and Emerging Atomic Frequency Standards*, IEEE Transactions on Ultrasonics, Ferroelectrics, and Frequency Control **68**, 2007 (2021).

- [9] J. Kitching, *Chip-scale atomic devices*, Applied Physics Reviews **5**, 031302 (2018).
- [10] J. Kitching, S. Knappe, and L. Hollberg, *Miniature vapor-cell atomic-frequency references*, Applied Physics Letters **81**, 553 (2002).
- [11] L.-A. Liew *et al.*, *Microfabricated alkali atom vapor cells*, Applied Physics Letters **84**, 2694 (2004).
- [12] Z. Cui, *Anodic Bonding* (Springer US, Boston, MA, 2008), pp. 50–54.
- [13] S. Knappe *et al.*, *A microfabricated atomic clock*, Applied Physics Letters **85**, 1460 (2004).
- [14] P. D. Schwindt *et al.*, *Chip-scale atomic magnetometer with improved sensitivity by use of the Mx technique*, Applied Physics Letters **90** (2007).
- [15] J. Kitching *et al.*, *NIST on a Chip: Realizing SI units with microfabricated alkali vapour cells*, Journal of Physics: Conference Series **723**, 012056 (2016).
- [16] L.-A. Liew, J. Moreland, and V. Gerginov, *Wafer-level filling of microfabricated atomic vapor cells based on thin-film deposition and photolysis of cesium azide*, Applied Physics Letters **90**, 114106 (2007).
- [17] M. Hasegawa *et al.*, *Microfabrication of cesium vapor cells with buffer gas for MEMS atomic clocks*, Sensors and Actuators A: Physical **167**, 594 (2011), Solid-State Sensors, Actuators and Microsystems Workshop.
- [18] M. A. Perez *et al.*, *Rubidium vapor cell with integrated Bragg reflectors for compact atomic MEMS*, Sensors and Actuators A: Physical **154**, 295 (2009), 21st IEEE International Conference on Micro Electro Mechanical Systems, Tucson, AZ, USA, 13-17 January 2008.
- [19] H. Nishino *et al.*, *A reflection-type vapor cell using anisotropic etching of silicon for micro atomic clocks*, Applied Physics Express **12**, 072012 (2019).

- [20] Y. Pétremand *et al.*, *Microfabricated rubidium vapour cell with a thick glass core for small-scale atomic clock applications*, *Journal of Micromechanics and Microengineering* **22**, 025013 (2012).
- [21] T. Dyer *et al.*, *Micro-fabricated caesium vapor cell with 5mm optical path length*, *Journal of Applied Physics* **132**, 204401 (2022).
- [22] R. Chutani, M. Hasegawa, V. Maurice, N. Passilly, and C. Gorecki, *Single-step deep reactive ion etching of ultra-deep silicon cavities with smooth sidewalls*, *Sensors and Actuators A: Physical* **208**, 66 (2014).
- [23] R. Chutani *et al.*, *Laser light routing in an elongated micromachined vapor cell with diffraction gratings for atomic clock applications*, *Scientific Reports* 2015 5:1 **5**, 1 (2015).
- [24] D. A. Steck, *Rubidium 87 D Line Data*, Available Online.
- [25] D. A. Steck, *Rubidium 85 D Line Data*, Available Online.
- [26] D. A. Steck, *Cesium D Line Data*, Available Online, 2001.
- [27] C. Foot, *Atomic physics* (Oxford University Press, USA, 2005).
- [28] P. Siddons, C. S. Adams, C. Ge, and I. G. Hughes, *Absolute absorption on rubidium D lines: comparison between theory and experiment*, *Journal of Physics B: Atomic, Molecular and Optical Physics* **41**, 155004 (2008).
- [29] S. J. Seltzer, *Developments in alkali -metal atomic magnetometry*, PhD thesis, Princeton University, 2008.
- [30] M. A. Zentile *et al.*, *ElecSus: A program to calculate the electric susceptibility of an atomic ensemble*, *Computer Physics Communications* **189**, 162 (2015).
- [31] Y. Liu, J. Lin, G. Huang, Y. Guo, and C. Duan, *Simple empirical analytical approximation to the Voigt profile*, *J. Opt. Soc. Am. B* **18**, 666 (2001).

- [32] B. E. Sherlock and I. G. Hughes, *How weak is a weak probe in laser spectroscopy?*, American Journal of Physics **77**, 111 (2009).
- [33] D. A. Smith and I. G. Hughes, *The role of hyperfine pumping in multilevel systems exhibiting saturated absorption*, American Journal of Physics **72**, 631 (2004).
- [34] R. Vicarini *et al.*, *Mitigation of Temperature-Induced Light-Shift Effects in Miniaturized Atomic Clocks*, IEEE Transactions on Ultrasonics, Ferroelectrics and Frequency Control **66**, 1962 (2019).
- [35] D. Hunter *et al.*, *Free-Induction-Decay Magnetometer Based on a Micro-fabricated Cs Vapor Cell*, Phys. Rev. Appl. **10**, 014002 (2018).
- [36] V. Shah, S. Knappe, P. D. Schwindt, and J. Kitching, *Subpicotesla atomic magnetometry with a microfabricated vapour cell*, Nature Photonics 2007 1:11 **1**, 649 (2007).
- [37] J. Kitching, *Chip-scale atomic devices*, Appl. Phys. Rev **5**, 31302 (2018).
- [38] S. Karlen, J. Haesler, T. Overstolz, G. Bergonzi, and S. Lecomte, *Sealing of MEMS Atomic Vapor Cells Using Cu-Cu Thermocompression Bonding*, Journal of Microelectromechanical Systems **29**, 95 (2020).
- [39] F. Laermer, S. Franssila, L. Sainiemi, and K. Kolari, *Chapter 16 - Deep reactive ion etching*, in *Handbook of Silicon Based MEMS Materials and Technologies (Third Edition)*, edited by M. Tilli *et al.*, Micro and Nano Technologies, pp. 417–446, Elsevier, , third edition ed., 2020.
- [40] J. P. McGilligan *et al.*, *Micro-fabricated components for cold atom sensors*, Review of Scientific Instruments **93**, 91101 (2022).
- [41] S. Woetzel *et al.*, *Microfabricated atomic vapor cell arrays for magnetic field measurements*, Review of Scientific Instruments **82**, 033111 (2011).
- [42] N. Cooper *et al.*, *Additively manufactured ultra-high vacuum chamber for portable quantum technologies*, Additive Manufacturing **40**, 101898 (2021).

- [43] K.-S. Chen, A. Ayon, X. Zhang, and S. Spearing, *Effect of process parameters on the surface morphology and mechanical performance of silicon structures after deep reactive ion etching (DRIE)*, *Journal of Microelectromechanical Systems* **11**, 264 (2002).
- [44] R. Straessle *et al.*, *Low-temperature indium-bonded alkali vapor cell for chip-scale atomic clocks*, *Journal of Applied Physics* **113**, 064501 (2013).
- [45] V. Maurice *et al.*, *Microfabricated vapor cells for miniature atomic clocks based on post-sealing activated cesium dispensers*, in *2017 Joint Conference of the European Frequency and Time Forum and IEEE International Frequency Control Symposium (EFTF/IFCS)*, pp. 636–637, 2017.
- [46] V. Maurice *et al.*, *Microfabricated vapor cells filled with a cesium dispensing paste for miniature atomic clocks*, *Applied Physics Letters* **110**, 164103 (2017).
- [47] M. T. Hummon *et al.*, *Photonic chip for laser stabilization to an atomic vapor with 10^{11} instability*, *Optica* **5**, 443 (2018).
- [48] A. S. Arnold, J. S. Wilson, and M. G. Boshier, *A simple extended-cavity diode laser*, *Review of Scientific Instruments* **69**, 1236 (1998).
- [49] E. Batori *et al.*, *μ POP Clock: A Microcell Atomic Clock Based on a Double-Resonance Ramsey Scheme*, *Phys. Rev. Appl.* **18**, 054039 (2022).
- [50] C. Carlé *et al.*, *Pulsed-CPT Cs-Ne microcell atomic clock with frequency stability below 2×10^{-12} at 10^5 s*, *Opt. Express* **31**, 8160 (2023).
- [51] V. G. Lucivero, A. Zanoni, G. Corrielli, R. Osellame, and M. W. Mitchell, *Laser-written vapor cells for chip-scale atomic sensing and spectroscopy*, *Opt. Express* **30**, 27149 (2022).
- [52] M. Jiang *et al.*, *Characterization of ^{87}Rb MEMS vapor cells for miniature atomic magnetometers*, *Applied Physics Letters* **123**, 062406 (2023).

- [53] M. T. Graf *et al.*, *Relaxation of atomic polarization in paraffin-coated cesium vapor cells*, Phys. Rev. A **72**, 023401 (2005).
- [54] M. C. D. Tayler *et al.*, *Miniature Biplanar Coils for Alkali-Metal-Vapor Magnetometry*, Phys. Rev. Applied **18**, 014036 (2022).
- [55] T. Scholtes, S. Woetzel, R. IJsselsteijn, V. Schultze, and H.-G. Meyer, *Intrinsic relaxation rates of polarized Cs vapor in miniaturized cells*, Applied Physics B **117**, 211 (2014).
- [56] A. McWilliam, *A Dual-Beam Free Induction Decay Magnetometer*, PhD thesis, University of Strathclyde, 2024.
- [57] N. Beverini, P. Minguzzi, and F. Strumia, *Foreign-Gas-Induced Cesium Hyperfine Relaxation*, Phys. Rev. A **4**, 550 (1971).
- [58] F. A. Franz and E. Lüscher, *Spin Relaxation of Optically Pumped Cesium*, Phys. Rev. **135**, A582 (1964).
- [59] F. A. Franz and C. E. Sooriamoorthi, *Spin relaxation within the $6^2P_{1/2}$ and $6^2S_{1/2}$ states of cesium measured by white-light optical pumping*, Phys. Rev. A **10**, 126 (1974).
- [60] V. Maurice *et al.*, *Wafer-level vapor cells filled with laser-actuated hermetic seals for integrated atomic devices*, Microsystems & Nanoengineering **8**, 129 (2022).
- [61] S. Ingleby, P. Griffin, T. Dyer, M. Mrozowski, and E. Riis, *A digital alkali spin maser*, Scientific Reports **12**, 12888 (2022).
- [62] R. Mottola, G. Buser, and P. Treutlein, *Optical Memory in a Microfabricated Rubidium Vapor Cell*, Phys. Rev. Lett. **131**, 260801 (2023).
- [63] W. Martin and W. Wiese, *Chapter 10: Atomic Spectroscopy*, in *Springer Handbook of Atomic, Molecular, and Optical Physics*, edited by G. Drake, pp. 175–198, Springer New York, New York, NY, 2006.

- [64] A. Andalkar and R. B. Warrington, *High-resolution measurement of the pressure broadening and shift of the Cs D1 and D2 lines by N₂ and He buffer gases*, Phys. Rev. A - At. Mol. Opt. Phys. **65**, 7 (2002).
- [65] G. A. Pitz, D. E. Wertepny, and G. P. Perram, *Pressure broadening and shift of the cesium D₁ transition by the noble gases and N₂, H₂, HD, D₂, CH₄, C₂H₆, CF₄, and ³He*, Phys. Rev. A **80**, 062718 (2009).
- [66] A. H. Couture, T. B. Clegg, and B. Driehuys, *Pressure shifts and broadening of the Cs D1 and D2 lines by He, N₂, and Xe at densities used for optical pumping and spin exchange polarization*, Journal of Applied Physics **104**, 094912 (2008).
- [67] S. Piccolomo, *Chip-scale atomic magnetometer*, Thesis, University of Strathclyde, 2016.
- [68] M. A. Hafiz, G. Coget, E. de Clercq, and R. Boudot, *Doppler-free spectroscopy on the Cs D1 line with a dual-frequency laser.*, Optics letters **41**, 2982 (2016).
- [69] R. Wynands and S. Weyers, *Atomic fountain clocks*, Metrologia **42**, S64 (2005).
- [70] D. Pizzey *et al.*, *Laser spectroscopy of hot atomic vapours: from 'scope to theoretical fit*, New Journal of Physics **24**, 125001 (2022).
- [71] J. A. Rushton, M. Aldous, and M. D. Himsworth, *Contributed Review: The feasibility of a fully miniaturized magneto-optical trap for portable ultracold quantum technology*, Review of Scientific Instruments **85**, 121501 (2014).
- [72] P. Manini and E. Maccallini, *NEG pumps: Sorption mechanisms and applications*, arXiv: Instrumentation and Detectors (2020).
- [73] SAES Getters, *ST 707 non evaporable getters activatable at low*, available online <https://psec.uchicago.edu/getters/St%20707%20Brochure.pdf>, Accessed: 20-03-2024.

- [74] D. Hunter, T. E. Dyer, and E. Riis, *Accurate optically pumped magnetometer based on Ramsey-style interrogation*, Opt. Lett. **47**, 1230 (2022).
- [75] J. R. Zimmerman and D. Williams, *Nuclear Gyromagnetic Ratios of Be^9 , Rb^{85} , Rb^{87} , and Cs^{133}* , Phys. Rev. **75**, 699 (1949).
- [76] C. Carlé *et al.*, *Reduction of helium permeation in microfabricated cells using aluminosilicate glass substrates and Al_2O_3 coatings*, Journal of Applied Physics **133**, 214501 (2023).
- [77] S. A. Knappe, H. G. Robinson, and L. Hollberg, *Microfabricated saturated absorption laser spectrometer*, Opt. Express **15**, 6293 (2007).
- [78] D. G. Bopp, V. M. Maurice, and J. E. Kitching, *Wafer-level fabrication of alkali vapor cells using in-situ atomic deposition*, Journal of Physics: Photonics **3**, 015002 (2020).
- [79] J. M. Pate, J. Kitching, and M. T. Hummon, *Microfabricated strontium atomic vapor cells*, Opt. Lett. **48**, 383 (2023).
- [80] E. Klinger *et al.*, *Sub-Doppler spectroscopy of the Cs atom $6S_{1/2} - 7P_{1/2}$ transition at 459 nm in a microfabricated vapor cell*, Opt. Lett. **49**, 1953 (2024).
- [81] Z. L. Newman *et al.*, *High-performance, compact optical standard*, Opt. Lett. **46**, 4702 (2021).
- [82] N. P. Georgiades, E. S. Polzik, and H. J. Kimble, *Two-photon spectroscopy of the $6S_{1/2} \rightarrow 6D_{5/2}$ transition of trapped atomic cesium*, Optics Letters, Vol. 19, Issue 18, pp. 1474-1476 **19**, 1474 (1994).
- [83] J. Lee *et al.*, *A compact cold-atom interferometer with a high data-rate grating magneto-optical trap and a photonic-integrated-circuit-compatible laser system*, Nature Communications **13**, 5131 (2022).
- [84] M. A. Kasevich, E. Riis, S. Chu, and R. G. DeVoe, *rf spectroscopy in an atomic fountain*, Phys. Rev. Lett. **63**, 612 (1989).

- [85] R. Elvin *et al.*, *Cold-atom clock based on a diffractive optic*, *Opt. Express* **27**, 38359 (2019).
- [86] B. Lewis, R. Elvin, A. S. Arnold, E. Riis, and P. F. Griffin, *A grating-chip atomic fountain*, *Applied Physics Letters* **121**, 164001 (2022).
- [87] A. Bregazzi *et al.*, *A cold-atom Ramsey clock with a low volume physics package*, *Scientific Reports* **14**, 931 (2024).
- [88] J. D. Elgin *et al.*, *A cold-atom beam clock based on coherent population trapping*, *Applied Physics Letters* **115**, 033503 (2019).
- [89] C. Wieman, G. Flowers, and S. Gilbert, *Inexpensive laser cooling and trapping experiment for undergraduate laboratories*, *American Journal of Physics* **63**, 317 (1995).
- [90] J. P. McGilligan *et al.*, *Grating chips for quantum technologies*, *Scientific Reports* 2017 7:1 **7**, 1 (2017).
- [91] T. Ikegami, S. ichi Ohshima, and M. Ohtsu, *Frequency Stabilization of Laser Diodes to the Cs-D2 Line with the Zeeman Modulation Method*, *Japanese Journal of Applied Physics* **28**, L1839 (1989).
- [92] S. Balushev *et al.*, *Tunable and frequency-stabilized diode laser with a Doppler-free two-photon Zeeman lock*, *Appl. Opt.* **39**, 4970 (2000).
- [93] S. Lecomte, E. Fretel, G. Mileti, and P. Thomann, *Self-aligned extended-cavity diode laser stabilized by the Zeeman effect on the cesium D2 line*, *Appl. Opt.* **39**, 1426 (2000).
- [94] M. Himsforth, *Coherent manipulation of ultracold Rubidium*, PhD thesis, University of Southampton, 2009.
- [95] C. So *et al.*, *Zeeman-tunable modulation transfer spectroscopy*, *Opt. Lett.* **44**, 5374 (2019).

- [96] A. Strangfeld, B. Wiegand, J. Kluge, M. Schoch, and M. Krutzik, *Compact plug and play optical frequency reference device based on Doppler-free spectroscopy of rubidium vapor*, *Opt. Express* **30**, 12039 (2022).
- [97] M. Weel and A. Kumarakrishnan, *Laser-frequency stabilization using a lock-in amplifier*, *Canadian Journal of Physics* **80**, 1449 (Dec 2002).
- [98] B. Wiegand, B. Leykauf, R. Jördens, and M. Krutzik, *Linien: A versatile, user-friendly, open-source FPGA-based tool for frequency stabilization and spectroscopy parameter optimization*, *Review of Scientific Instruments* **93** (2022).
- [99] E. A. Donley, T. P. Heavner, F. Levi, M. O. Tataw, and S. R. Jefferts, *Double-pass acousto-optic modulator system*, *Rev. Sci. Instrum.* **76**, 63112 (2005).
- [100] R. P. Middlemiss *et al.*, *Measurement of the Earth tides with a MEMS gravimeter*, *Nature* **531**, 614 (2016).
- [101] P. F. Griffin, K. J. Weatherill, and C. S. Adams, *Fast switching of alkali atom dispensers using laser-induced heating*, *Rev. Sci. Instrum.* **76**, 93102 (2005).
- [102] J. Ma, A. Kishinevski, Y.-Y. Jau, C. Reuter, and W. Happer, *Modification of glass cell walls by rubidium vapor*, *Phys. Rev. A* **79**, 042905 (2009).
- [103] C. C. Nshii *et al.*, *A surface-patterned chip as a strong source of ultracold atoms for quantum technologies*, *Nature Nanotechnology* **8**, 321 (2013).
- [104] J. McGilligan, *Micro-fabricated diffractive optics for quantum sensors and atomic clocks*, PhD thesis, University of Strathclyde, 2017.
- [105] W. Riley and D. Howe, *Handbook of Frequency Stability Analysis*, 2008.
- [106] F. Gruet *et al.*, *Compact and frequency stabilized laser heads for Rubidium atomic clocks*, in *International Conference on Space Optics — ICSO 2012*,

- edited by B. Cugny, E. Armandillo, and N. Karafolas, volume 10564, p. 105642Y, International Society for Optics and Photonics, SPIE, 2017.
- [107] J. Ye, S. Swartz, P. Jungner, and J. L. Hall, *Hyperfine structure and absolute frequency of the $87\text{Rb } 5P_{3/2}$ state*, Opt. Lett. **21**, 1280 (1996).
- [108] M. Christ *et al.*, *Additive manufactured ceramics for compact quantum technologies*, 2024, 2402.10274.
- [109] D. O. Sabulsky *et al.*, *A fibered laser system for the MIGA large scale atom interferometer*, Scientific Reports **10**, 3268 (2020).
- [110] D. S. Weiss, E. Riis, Y. Shevy, P. J. Ungar, and S. Chu, *Optical molasses and multilevel atoms: experiment*, J. Opt. Soc. Am. B **6**, 2072 (1989).
- [111] D. J. Wineland, R. E. Drullinger, and F. L. Walls, *Radiation-Pressure Cooling of Bound Resonant Absorbers*, Phys. Rev. Lett. **40**, 1639 (1978).
- [112] W. D. Phillips and H. Metcalf, *Laser Deceleration of an Atomic Beam*, Phys. Rev. Lett. **48**, 596 (1982).
- [113] Y. Bidel *et al.*, *Compact cold atom gravimeter for field applications*, Applied Physics Letters **102**, 144107 (2013).
- [114] X. H. Bao *et al.*, *Efficient and long-lived quantum memory with cold atoms inside a ring cavity*, Nat. Phys. **8**, 517 (2012).
- [115] B. Nikolov, E. Diamond-Hitchcock, J. Bass, N. L. R. Spong, and J. D. Pritchard, *Randomized Benchmarking Using Nondestructive Readout in a Two-Dimensional Atom Array*, Phys. Rev. Lett. **131**, 030602 (2023).
- [116] H. J. Metcalf and P. van der Straten, *Laser cooling and trapping of atoms*, J. Opt. Soc. Am. B **20**, 887 (2003).
- [117] M. A. Lombardi, T. P. Heavner, and S. R. Jefferts, *NIST primary frequency standards and the realization of the SI second*, NCSLI Measure **2**, 74 (2007).

- [118] W. R. McGehee *et al.*, *Magneto-optical trapping using planar optics*, New Journal of Physics **23**, 013021 (2021).
- [119] N. Chauhan *et al.*, *Photonic Integrated Si_3N_4 Ultra-Large-Area Grating Waveguide MOT Interface for 3D Atomic Clock Laser Cooling*, in *Conference on Lasers and Electro-Optics (2019)*, Optical Society of America, 2019.
- [120] A. Isichenko, N. Chauhan, D. Bose, P. D. Kunz, and D. J. Blumenthal, *Cooling rubidium atoms with a photonic integrated 3D magneto-optical trap*, in *Optical Sensors and Sensing Congress (2022)*, Optical Society of America, 2022.
- [121] A. Isichenko *et al.*, *Photonic integrated beam delivery for a rubidium 3D magneto-optical trap*, Nature Communications **14**, 3080 (2023).
- [122] A. Yulaev *et al.*, *Interfacing Photonics to Free-Space via Large-area Inverse-designed Diffraction Elements and Metasurfaces*, in *Optical Fiber Communication Conference (OFC) 2021*, p. F2B.1, Optica Publishing Group, 2021.
- [123] L. Zhu *et al.*, *A dielectric metasurface optical chip for the generation of cold atoms*, Science Advances **6**, eabb6667 (2020).
- [124] V. A. Henderson *et al.*, *Optical characterisation of micro-fabricated Fresnel zone plates for atomic waveguides*, Opt. Express **28**, 9072 (2020).
- [125] L. Chen *et al.*, *Planar-Integrated Magneto-Optical Trap*, Phys. Rev. Applied **17**, 034031 (2022).
- [126] S. Kang *et al.*, *Magneto-optic trap using a reversible, solid-state alkali-metal source*, Optics Letters **44**, 3002 (2019).
- [127] J. P. McGilligan *et al.*, *Dynamic Characterization of an Alkali-Ion Battery as a Source for Laser-Cooled Atoms*, Phys. Rev. Applied **13**, 044038 (2020).
- [128] J. P. McGilligan *et al.*, *Laser cooling in a chip-scale platform*, Applied Physics Letters **117** (2020).

- [129] C. Adams and E. Riis, *Laser cooling and trapping of neutral atoms*, Progress in Quantum Electronics **21**, 1 (1997).
- [130] P. D. Lett *et al.*, *Observation of Atoms Laser Cooled below the Doppler Limit*, Phys. Rev. Lett. **61**, 169 (1988).
- [131] A. Bregazzi, *Miniaturised components for next generation cold-atom quantum sensors*, PhD thesis, University of Strathclyde, 2024.
- [132] G. W. Hoth, E. A. Donley, and J. Kitching, *Atom number in magneto-optic traps with millimeter scale laser beams*, Opt. Lett. **38**, 661 (2013).
- [133] M. Vangeleyn, *Atom trapping in non-trivial geometries for micro-fabrication applications*, PhD thesis, University of Strathclyde, 2011.
- [134] A. T. Dellis, V. Shah, E. A. Donley, S. Knappe, and J. Kitching, *Low helium permeation cells for atomic microsystems technology*, Optics Letters **41**, 2775 (2016).
- [135] O. S. Burrow *et al.*, *Stand-alone vacuum cell for compact ultracold quantum technologies*, Applied Physics Letters **119**, 124002 (2021).
- [136] R. Kohn *et al.*, *Clean, robust alkali sources by intercalation within highly oriented pyrolytic graphite*, Review of Scientific Instruments **91**, 035108 (2020).
- [137] B. J. Little *et al.*, *A passively pumped vacuum package sustaining cold atoms for more than 200 days*, AVS Quantum Science **3**, 035001 (2021).
- [138] A. Bregazzi *et al.*, *A simple imaging solution for chip-scale laser cooling*, Applied Physics Letters **119**, 184002 (2021).
- [139] A. T. Dellis, V. Shah, E. A. Donley, S. Knappe, and J. Kitching, *Low helium permeation cells for atomic microsystems technology*, Optics Letters **41**, 2775 (2016).
- [140] U. D. Rapol, A. Wasan, and V. Natarajan, *Loading of a Rb magneto-optic trap from a getter source*, Phys. Rev. A **64**, 023402 (2001).

- [141] T. Arpornthip, C. A. Sackett, and K. J. Hughes, *Vacuum-pressure measurement using a magneto-optical trap*, Phys. Rev. A **85**, 033420 (2012).
- [142] J. P. McGilligan, P. F. Griffin, E. Riis, and A. S. Arnold, *Phase-space properties of magneto-optical traps utilising micro-fabricated gratings.*, Opt. Express **23**, 8948 (2015).
- [143] N. F. Ramsey, *A Molecular Beam Resonance Method with Separated Oscillating Fields*, Phys. Rev. **78**, 695 (1950).
- [144] G. Santarelli *et al.*, *Quantum Projection Noise in an Atomic Fountain: A High Stability Cesium Frequency Standard*, Phys. Rev. Lett. **82**, 4619 (1999).
- [145] B. L. S. Marlow and D. R. Scherer, *A Review of Commercial and Emerging Atomic Frequency Standards*, IEEE Transactions on Ultrasonics, Ferroelectrics, and Frequency Control **68**, 2007 (2021).
- [146] R. Flytkjær, F. Sabri, R. Esteve, W. Jessie, and P. M. T. Goulding, *The economic impact on the UK of a disruption to GNSS*, Available Online, 2023.
- [147] M. Cuntz, A. Konovaltsev, A. Dreher, and M. Meurer, *Jamming and Spoofing in GPS/GNSS Based Applications and Services – Threats and Countermeasures*, in *Future Security*, edited by N. Aschenbruck, P. Martini, M. Meier, and J. Tölle, pp. 196–199, Berlin, Heidelberg, 2012, Springer Berlin Heidelberg.
- [148] UK: Government Office for Science, *Quantum technologies: Blackett review*, Available Online.
- [149] L. S. Cutler, *Fifty years of commercial caesium clocks*, Metrologia **42**, S90 (2005).
- [150] T. M., *Next-Generation Chip Scale Atomic Clocks - Assessing the emerging physical platforms: microwave transitions in cold atoms and in trapped ions, and optical transitions in warm vapours*, (2022).

- [151] S. Lee *et al.*, *Laser frequency stabilization in the 10^{-14} range via optimized modulation transfer spectroscopy on the ^{87}Rb D_2 line*, Opt. Lett. **48**, 1020 (2023).
- [152] S. Zhang *et al.*, *Compact Rb optical frequency standard with 10^{-15} stability*, Review of Scientific Instruments **88**, 103106 (2017).
- [153] V. Schkolnik *et al.*, *JOKARUS - Design of a compact optical iodine frequency reference for a sounding rocket mission*, (2017), 1702.08330.
- [154] K. W. Martin *et al.*, *Compact Optical Atomic Clock Based on a Two-Photon Transition in Rubidium*, Phys. Rev. Appl. **9**, 014019 (2018).
- [155] B. L. Keliehor, *Technology development for a compact rubidium optical frequency reference*, PhD thesis, University of Strathclyde, 2023.
- [156] F. Biraben, *The first decades of Doppler-free two-photon spectroscopy*, Comptes Rendus Physique **20**, 671 (2019), La science en mouvement 2 : de 1940 aux premières années 1980 – Avancées en physique.
- [157] W. Demtröder, *Nonlinear Spectroscopy* (Springer Berlin Heidelberg, Berlin, Heidelberg, 2015), pp. 83–147.
- [158] K. Martin, *Compact Optical Frequency Standards for Future Applications Beyond the Laboratory*, PhD thesis, University of New Mexico, 2019.
- [159] V. Maurice *et al.*, *Miniaturized optical frequency reference for next-generation portable optical clocks*, Opt. Express **28**, 24708 (2020).
- [160] D. Sheng, A. Pérez Galván, and L. A. Orozco, *Lifetime measurements of the $5d$ states of rubidium*, Phys. Rev. A **78**, 062506 (2008).
- [161] A. J. Olson, E. J. Carlson, and S. K. Mayer, *Two-photon spectroscopy of rubidium using a grating-feedback diode laser*, American Journal of Physics **74**, 218 (2006).

- [162] S. Villalba *et al.*, *Sub-Doppler resonances in the backscattered light from random porous media infused with Rb vapor*, Phys. Rev. A **89**, 023422 (2014).
- [163] A. Akulshin, V. Sautenkov, V. Velichansky, A. Zibrov, and M. Zverkov, *Power broadening of saturation absorption resonance on the D_2 line of rubidium*, Optics Communications **77**, 295 (1990).
- [164] K. Sosa, J. Oreggioni, and H. Failache, *Miniaturized saturated absorption spectrometer*, Review of Scientific Instruments **91**, 083101 (2020).
- [165] R. Han, Z. You, F. Zhang, H. Xue, and Y. Ruan, *Microfabricated Vapor Cells with Reflective Sidewalls for Chip Scale Atomic Sensors*, Micromachines **9** (2018).
- [166] E. D. Palik, *Handbook of Optical Constants of Solids* (Elsevier, 1998).
- [167] Biraben, F., Bassini, M., and Cagnac, B., *Line-shapes in Doppler-free two-photon spectroscopy. The effect of finite transit time*, J. Phys. France **40**, 445 (1979).
- [168] S. Pollock, J. P. Cotter, A. Laliotis, and E. A. Hinds, *Integrated magneto-optical traps on a chip using silicon pyramid structures*, Opt. Express **17**, 14109 (2009).
- [169] R. Chutani, N. Passilly, J. Albero, M. Baranski, and C. Gorecki, *Deep Wet-Etched Silicon Cavities for Micro-Optical Sensors: Influence of Masking on $\{111\}$ Sidewalls Surface Quality*, Journal of Microelectromechanical Systems **23**, 585 (2014).
- [170] H. Nishino *et al.*, *Reflection-type vapor cell for micro atomic clocks using local anodic bonding of 45° mirrors*, Optics Letters, Vol. 46, Issue 10, pp. 2272-2275 **46**, 2272 (2021).
- [171] C. Iglesias *et al.*, *Fabrication of a Nanofluidic Channel for SPR Sensing Application Using Glass-to-Glass Anodic Bonding*, Electrochemistry **74**, 169 (2006).

-
- [172] F. Wittkämper, T. Scholtes, S. Linzen, M. Ziegler, and R. Stolz, *Integration of Passivated Gold Mirrors into Microfabricated Alkali Vapor Cells*, *Coatings* **13** (2023).